„Dunărea de Jos" University of Galati

Doctoral School for Mechanical and Industrial Engineering

DOCTORAL THSESIS

CHARACTERIZATION OF TWO FAMILIES OF POLYMERIC BLENDS BASED ON PA6 AND PP BY TENSILE AND CHARPY TESTS. ABSTRACT

PhD student

eng. Andreea Elena Musteață

President	prof. eng. Victor Cristian Eugen Rusu, PhD
Scientific coordinator	prof. eng. Lorena Deleanu, PhD
Scientific references	prof. eng. Anton Hadăr, PhD
	prof. eng. Sorin Cănănău, PhD
	prof. eng. Mihaela Buciumeanu, PhD

Series I6: Mechanical Engineering no. 53

GALAȚI

2020

ACKNOWLEDGEMENT

I would like to thank those who offered their support and guided me during this doctoral thesis.

First of all, I would like to thank Professor eng. Lorena Deleanu, PhD, who, as a scientific supervisor, offered me her permanent guidance, support and encouragement during the period of doctoral preparation and thesis elaboration.

I would like to sincerely thank the commission for guiding and evaluating the paper, formed by Professor Phys. Adrian Cîrciumaru, PhD, associate professor eng. Sorin Ciortan, PhD and associate professor eng. Constantin Georgescu, PhD, for the help offered, but also for the competent guidance and recommendations, of a high degree of professionalism.

This doctoral thesis would not have been complete without the help of eng. Doina Constantinescu, PhD manager at MONOFIL Șăvinești.

I would like to thank the INCAS National Institute of Aerospace Research for access to test equipment and modeling systems to the following scientific researchers: Cătălin Pîrvu, Ph.D., chem. Adriana Ștefan, PhD, eng. Mihail Boțan PhD, and eng. George Pelin, PhD, for the help given to the calibration of the test equipment and the interpretation of the traction results.

Charpy tests could not have been performed without the latest equipment in the Materials Strength Laboratory at the "Politehnica" University of Bucharest and eng. Horia Petrescu, PhD.

For the support given to the use of the electron microscope within the "Dunărea de Jos" University, I thank phsis. Alina Cantaragiu, PhD.

With special gratitude and love, I thank my parents who were with me, surrounded me with their affection and patience and who supported me in all respects during this period.

Andreea Elena Musteață

Summary

Chapter 1
Polyamide + Polypropylene Polymeric Blends (PA + PP)

1.1. Characterization of Polymeric Blends

Polymer blends have been developing in parallel with the advance of polymers. Once nitrocellulose was invented, it was mixed with nitrile rubber. The first compatible blend dates from 1928 and is that of polyvinyl chloride (PVC) with polyvinyl acetate (PVAc) and its copolymers. PVC was marketed in 1931, while its blends with butadiene nitrile rubber were patented in 1936. The modern era of polymer blends began in 1960, after Alan Hay discovered the oxidative polymerization of 2,4-xylenols, which developed polyphenylene ether (PPE). Its blends with styrene rubbers were on the market in 1965. At present, polymer alloys, polymer blends and their composites represent over 80% (by mass) of the total polymer-based materials [Rosato, 2003], [Rosato, 2004].

Polymer blends is attracting the attention of specialists through a set of particular properties, such as low specific mass, strength-to-mass and stiffness-to-mass ratios superior to traditional materials, tribological properties [Botan, 2017], resistance to aggressive environments, electrical and thermal properties, which led to the use in the field of aeronautics, shipbuilding, machine building, fine mechanics, electronics, medical equipment etc. Blends can be formed with miscible polymers, homogeneous polymer mixture up to the molecular level and with immiscible polymers, as is the PP + PA6 blends.

Polymer blending is the most versatile and economical method of producing materials capable of meeting complex performance demands. The trend is to offer blends that can be treated like any other resin on the market; therefore, their workability must match that of simple polymers, but they offer a much wider range of performance possibilities.

The advantages of polymer blends fall into two categories:

A. improving product performance:

- production of materials that have a complete set of desired properties, at low costs,
- extending the performance of polymers by incorporating less expensive polymers,
- improving specific properties: increasing the resilience of brittle polymers, eliminating the need to use low molecular weight additives, mixing with more rigid and heat-resistant resins/components to improve modulus of elasticity and dimensional stability, incorporating amorphous semicrystalline polymer into a resin to increase chemical resistance, the incorporation of non-flammable resin into a flammable one for improving flame resistance, mixing polymers with the -OH or -SH functional group in order to have permanently anti-static materials, obtaining biodegradable materials, mixing layered materials and composites,

B. improving machinability.

1.2. PA + PP Polymer Blends

Polypropylene (PP) is a cheap polymer, with versatile applications, high purity and chemical stability. PP belongs to the category of polyolefins, thermoplastic materials with a wide spread properties, the parts being made by injection. It is a semicrystalline thermoplastic, whose set of properties makes it suitable for a wide variety of engineering applications [Bradley, 1984]. It also offers exceptional chemical resistance at a relatively low cost. It is an easy-to-process material, with medium impact resistance, fair structural strength and resistance to an impressive range of chemicals.

PP is processed mainly by injection, but also by extrusion or thermoforming [Biron, 2010]. Trademarks usually contain stabilizing antioxidants and other additives [Grob, 2012], [Palacios, 2016]. The set of properties that includes high degree of crystallinity, low density,

high melting point (T_m=166 °C) and a deformation temperature under load higher than 90 °C also indicates good processability [Bradley, 1984]. The crystallinity of the isotactic PP homopolymer has a brittle behavior at low temperatures or on impact, if the parts have high stress concentrators (sharp notches, holes etc.). The low temperature impact resistance of unmodified PP and the Izod impact resistance give lower values than those obtained for PE. Fragility is related to spherulitic morphology and the tendency of cracking by spinning of PP, which increases in the presence of stress concentrators, especially at negative temperatures. [Utracki, 1995], [Utracki, 2002], [Folkes, 1993].

For PP with additives, composite type or polymer blends, an ability of the inclusions was observed to play a role in inducing shear fibrillation of the matrix and in propagating the crack tip. The impact resistance of PP can be improved with an elastomer modificator. The rigidity of the blend decreases with increasing the elastomer content. The interpretation of mechanisms responsable for increasing the impact resistance of modified PP with elastomers is based on multiple crazing, shear flow and tmechanism of cavitation and micropore formation. The elastomer particles in the PP matrix should be uniform in size and the interfacial adhesion between PP and elastomer should be good [Albrecht, 2006].

Like PA, PP accepts as elastomeric compatibilizers, such as those based on ethylene propylene (EP or EPDM) in low to medium concentrations (5% to 25 wt%). Low density polyethylene (LDPE) [Musteata, 2020] and high density polyethylene (HDPE) can be added to improve the hyperstability of elastomeric particles and to improve the set of tensile and impact properties.

Polyamides (PA6; PA6,6; PA6,10; PA6,12; PA 11, PA 12) have many applications due to their easy processability, low friction, wear resistance and rather high melting temperature, but they have the disadvantage of a higher cost, critical fragility to space demands and water absorption. Polyamides have constantly found areas of applicability, in which properties, such as mechanical properties [Botan, 2014], wear resistance [Botan, 2014], good resistance to hydrocarbons and good behavior at high temperatures are important. Due to the higher production cost as compared to PE and PS, their applicability was higher in mechanical engineering. The effects of the environment on the properties of polyamide include high sensitivity to moisture and water absorption. Increasing the crystallinity of polyamides influences the mechanical properties (increases hardness and wear resistance, reduces opacity and shock resistance). Copolymerization contributes to increased transparency, flexibility and reduced melting temperature.

The PP + PA6 blends has been tested for improved mechanical properties, where PP ensures good processability and moisture insensitivity, and PA6 contributes with mechanical and thermal properties. In the recent years, their nanocomposites have attracted the attention of the industry. As a result of nanoscale dispersions, composites show a significant mechanical improvement, particular thermal, physico-chemical properties as compared to conventional composites. To recent date, researchers have described nanocomposites based on an unique polymer matrix. Nanocomposites based on blends of two or more polymers (binary or ternary blends) seem to be a newer approach. Nanocomposites based on PP + PA6 blends were studied in [Chow, 2003], [Ou, 2009]. It has been observed that they can have properties in wide ranges, even for reinforced blends.

Sharma [Sharma, 2012] highlighted that PA+PP blends were introduced by DSM, Atochem and Mitsubishi (automotive industry) because they have lower water absorption than polyamide, dimensional stability (as an influence of PP concentration), low density, low permeability of liquids and vapors, moderate impact resistance induced by PA and good resistance to alcohols and glycols.

1.3. Particular aspects of PA + PP blends

PP + PA blends are immiscible mixtures, usually with strongly asymmetrical compositions (90/10, 80/20 or 70/30), which often have island morphologies, large droplets and lack of adhesion between phases, as a result of high values of interfacial stresses between immiscible phases. If no compatibilizers are added, the mixtures have poor mechanical properties, but in recent decades better results have been reported for these blends, but with compatibility additions [Palacios, 2016], [G'Sell, 2002], [Bai, 2004], [Bai, 2005], [Fu, 2006].

The compatibilizers of these blends are block copolymers, with different architectures (linear, stellar, crosslinked, cyclic polymers), spherical nanoparticles or in sheets or plates [Alexandrescu, 2017], [Banerjee, 2013], [Beuguel, 2017], elastomers [Gonzales-Montiel, 1995], [Palacios, 2016]. The most used elastomers with this role are: ethylene-propylene maleate copolymer (EPR), ethylene-propylene-diene maleate monomer (EPDM), [Vranjes, 2012], [Ma, 2019], styrene-ethylene-butylene-styrene maleate block copolymer (SEBS) [Gonzales-Montiel, 1995], [G'Sell, 2002], [Hosseini, 2015].

PP was mixed with EPDM to obtain a material that hardens and whose modulus of elasticity depends on the composition and temperature, but also has impact resistance in brands launched by Monsanto, Novacor, Mitsui Petrochem. [Sharma, 2012]. Antunes et al. [Antunes, 2011] studied the crosslinking effect on the phase inversion of PP+EPDM blends and reported that the phase inversion area is influenced by the mass ratio of the constituents and not by the ratio between their viscosities.

Clay particles serve as effective nucleating agents that can alter the crystalline morphology of polymers, such as PA6 and PP [Sharma, 2012].

Yu et al. [Yu, 2015] showed that, in the microstructure of the studied blends, the elastomer and the network of fibrils, formed on glass fibers, lead to improved ductility and resilience. Comparing the microstructure of PA6 and the nano-ocomposites PA6+5% POE-g-MAH (octen-ethylene elastomer with crosslinked maleic anhydride), it was observed that the latter had more wrinkled cavities and filaments. The cavitation of the elastomer, followed by the plastic notching of the gaps, promoted the plastic deformation of the matrix, prevented the growth of the crack and generated a rough surface at failure. The process of fibrillation can disperse a large amount of impact energy, making the PA6 matrix easily deformable.

Bai et al. [Bai, Part 1, 2004] developed a class of blends, composed of three phases: PP, PA6 and polyethylene-octene elastomer (POE) grafted with maleic anhydride. The mass fraction of PA6 was adjusted from 0 to 40%, in steps of 10%, and the mass fraction of POE was kept at half that of PA6. The morphology was mainly from PA6 particles dispersed in the PP matrix. The POE modifier was observed as a thin interface (less than 100 nm thick) at the PP/PA6 interface, and as isolated, but few, particles. The modulus of elasticity and the tensile strength are almost constant for PP and blends. But the Izod impact resistance greatly increases with the content of the alloying components. This remarkable effect is justified by the POE cavity at the interface, the high shear plastic deformation and the resistance of PA6 particles to crack propagation.

Laoutid et al. [Laoutid, 2013] found that the incorporation of 5 wt% hydrophobic nanosilica in PP+PA blends (80+20 wt/wt) led to a reduction in the size of dispersed droplets and a change in mechanical properties. This reduction in droplet size was due to the preferential migration of silica nanoparticles at the interface between PP and PA or PC, which led to the formation of an anti-coalescence barrier around the dispersed droplets.

The PA blends of most thermoplastics show a coarse morphology as a result of high interfacial tension. To obtain satisfactory results with PA blends, they must contain compatibizing agents.

Polyamides modified for impact resistance have better processability, including injection molding. Blends with elastomer particles, dispersed in the PA matrix, began to be

used [Bai, 2005], [G'Sell, 2004]. New trademarks also contain additions of short fiberglass, glass beads, clay and mineral powders. The applications of these blends are in various fields: sports and holiday equipment, medicine, automotive industry.

Although immiscible, there is a degree of compatibility between EP elastomers and the PP matrix, which leads to low interfacial tension and satisfactory interfacial adhesion [Utracki,2002].

A recent study [Hasanpour, 2019] presented the phase morphology, mechanical properties and breaking behavior of ternary mixtures PP/PA6/(EPDM: EPDM-g-MA) (70/15/15) with different concentrations of EPDM: EPDM-g-MA (Figure 1.1 presents the concluded models of the blends). The results showed that the tensile strain at break increases with the addition of EPDM-g-MA. PP has a semi-ductile behavior in tensile tests, while PA6 has a ductile fracture with higher fracture deformation and higher strength as compared to PP.

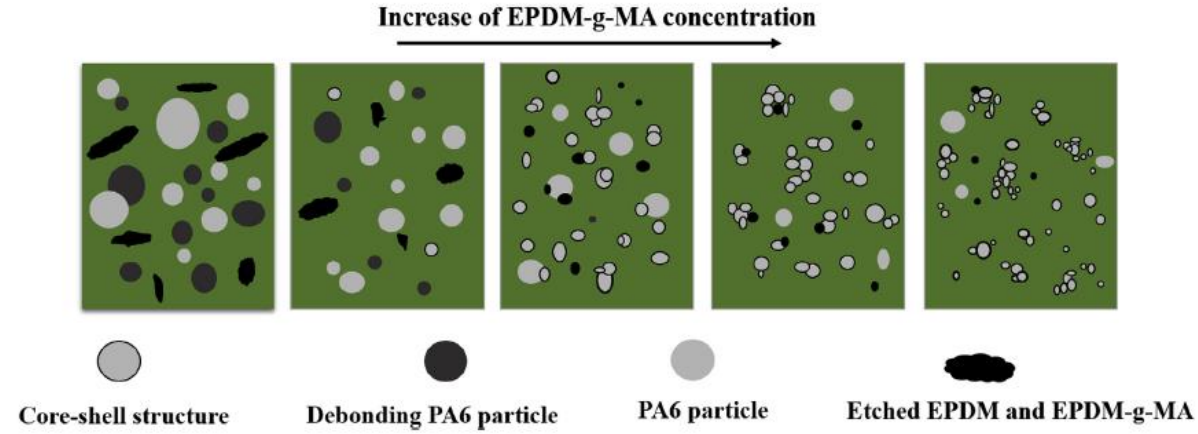

Fig. 1.1. Schematic representation of the morphology of PP/PA6/blends (EPDM-g-MA: EPDM) as a function of increasing EPDM+EPDM-g-MA content [Hasanpour, 2019]

Beuguel et al. [Beuguel, 2017] studied the influence of component concentration on the morphology and rheological properties of PP/PA12/mineral or synthetic clay blends. The rheological properties of the PP matrix influence the behavior at the interface: a higher viscosity of the matrix leads to a more developed interface by slowing down the migration of clay particles from the PP matrix into the PA12 nodules.

1.4. Modifiers for Polymeric Blends

Due to the semi-crystalline nature, thermoplastics have a high shrinkage during cooling and this can cause problems in achieving the accuracy of the parts injected into the mold. Mineral additives reduce the overall level of shrinkage, but if the particles are not isotropic, they can cause a differentiated shrinkage, leading to deformation or dimensional and shape instability (distortion) [Chanda, 2009], [Grob, 2012].

One of the main reasons for using mineral agents in thermoplastic polymers is the problem of shrinkage in their processing. Flattened agents, of sheet type, are generally more efficient, giving the best values in reducing shrinkage, while maintaining properties suitable for the application [Rothon, 1999].

Ground calcium carbonate is a common addition in thermoplastics. The main applications include PVC, but also PP and polyamides. The particle size depends on the application, but it is found commercially in a wide range. The advantages would be: low production price, small particle aspect ratio (so, towards spherical), high purity, improvement by cheap fatty acids. Calcium carbonate may have crystalline changes, but calcite is the most

commonly used form in polymers. [Hancock, 1995]. Most natural $CaCO_3$, used in thermoplastics, is treated with fatty acids (for not absorbing water).

In order to obtain good physical and mechanical characteristics, the uniform dispersion of clays, minerals is, sometimes, a difficult requirement to achieve.

Wang et al. [Wang, 2007] added organic clay (montmorillonite, 1 wt% and 4 wt%) and EPDM-g-MA (5 wt% to 40 wt%) to improve impact resistance and PA6 rigidity. The effects of clay on the morphology of the PA6/EPDM-g-MA blend were: weakening of interphase adhesion between PA6 and EPDM-g-MA particles led to the increase of elastomer particles at low concentrations of elastomer and clay, preventing coalescence between elastomer domains and reducing the size of elastomer particles in conditions of high concentration for elastomer and clay, widening the brittle-ductile transition range.

1.5. Conclusions and Future Research Directions

The topic of this research is of interest because

- blends can create a new set of properties, in particular for impact resistance and tribology,
- EF modeling allows for enlarging or restricting test intervals, but the simulation must be done after characterizing the blend, mechanically and thermally,
- the study will focus on thermoplastic blends with impact resistance properties based on PA6, PP and a thermoplastic elastomer, type EPDM,
- the results of the impact and tensile tests will be analyzed, as the author's proposed recipes are expected to have good impact results.

The purpose of the thesis and research directions are

- development of recipes for PA6 + PP blends, which are more efficient in terms of mechanical properties and low-speed impact, based on the critical analysis of a recent comprehensive documentation,
- study of the influence of the concentration and morphology of the blends on mechanical properties and at low speed impact,
- design and implementation of a tensile and Charpy test campaign, the results being analyzed for the ranking of the developed materials,
- study of the morphology of elaborated blends, using scanning electron microscopy and its role in Charpy impact and tensile failure processes,
- modeling, simulation of models for the Charpy test and validation using experimental results.

Chapter 3
Formulation and Processing of Classes of Blends PA6 + PP

3.1. General Aspects of Processing PA6 + PP Blends

Compatibilization has the following beneficial effects on the blends: it reduces surface tension to facilitate dispersion, stabilizes the morphology generated against changes in subsequent processing steps and improves adhesion between polymer domains, facilitating stress transfer, thus improving the mechanical properties of the product. [Utraki, 2002], [Harrats, 2006], [Datta, 1996].

The compatibilization strategy of immiscible polymers, such as PP and PA, involves one or more variants [Utracki, 2002], [Bicerano, 2002], [McKeen, 2008]:

- the addition of a small amount of co-solvent, a third component in the polymeric blend, which is miscible with both polymers (considered basic polymers),
- the addition of a copolymer with a miscible terminal group with one phase or a polymer and the other terminal group with the other phase or the other polymer,
- the addition of a large amount of coating-type copolymer, also commonly called impact modifier, because it improves impact qualities,
- a reactive compound, which alters at least some macromolecules and, thus, develops a local miscibility,
- additives which have mechanical and/or chemical influence on the blend etc.,

In PA + PP blend recipes, interfacial interactions and a morphology with rigid particles partially encapsulated in an elastomeric phase in the basic matrix are the key to good results for these blends.

An important conclusion is that it is difficult to predict the influence of constituents and their concentrations on mechanical properties and testing on specimens or actual components is the only way to have reliable data on the behavior of these materials, and to use them in design.

3.2. Recipes for the Blends to Be Studied

The two families of polymeric blends, formulated by the author will be presented. The recipes were established by mutual agreement with Monofil, Săvineşti, who also processed the blends, molding them (by injection) in the form of dumbbells for tensile testing and V-notch test plates for Charpy tests.

The first family of polymeric blends used for this research consists of polyamide 6, polypropylene, low density polyethylene (LDPE), calcium carbonate and a polybond 3200 adhesive, in the concentrations shown in Table 3.1.

The second family of polymer mixtures consists of polyamide 6, polypropylene, EPDM rubber (ethylene-propylene-diene-monomer), Polybond 3200 and kritylene, the concentration of the mixtures being given in Table 3.2.

Table 3.1. Recipes for the blens to be studied (first family)

Material	PA6	PP	LDPE	$CaCO_3$	Polybond 3200
PP	-	100	-	-	-
A	20	65	5	7	3
B	40	45	5	7	3
C	60	25	5	7	3
D	80	5	5	7	3
PA6	100	-	-	-	-

Table 3.2. Recipes for polymer blends (second family)

Material	PA6	PP	EPDM	Polybond 3200	Kritilen
PPm	-	99	-	-	1
H	12	60	8	20	-
G	42	20	28	10	-
PA6m	60	-	40	-	-

3.3. Components of the Studied Blends

PA6 (polyamide 6). Polyamides may also be a polymeric matrix in various composites with particle-type reinforcements, short, rigid or flexible fibers, but also in this family of materials. An issue is the interfacial adhesion to the filler materials, treated or not, for getting a better adhesion between them and matrix [Li, 2020]. Depending on the compatibility of the constituent polymers and the structure of the composite or blends, they can be: single-phase systems (solid solutions), generally with intermediate properties to those of the constituents, biphasic systems, in which compatibility is limited and morphologies are dispersions of constituents, the degree of dispersion being the main factor in determining their properties and systems containing branched polymers by crosslinking [Erdmann 2007], [Huang, 2006], [Chow, 2003], [Chow, 2015], [McKeen, 2008], [Jose, 2006].

PP (polypropylene). The development of new types of PP and research activities for light materials allows for replacing steel in automobiles in the near future. One of the major problems facing the components made of PP is low impact resistance. Hence, the idea of mixing PP with other polymers and/or elastomers to improve this property, while retaining, to some extent, the qualities of this polymer. Studies on PP-based blends are reported by Li et al. [Li, 2017], [Antunes, 2011], [Fu, 2006], [Hasanpour, 2019].

PP and PA compatibility can be achieved in three ways: chemical compatibility, by incorporating a compatibilizing agent, usually either a copolymer or multipolymer, physical compatibility, by physical means (high field of stresses in processing, heat treatment, irradiation etc.), reactive compatibility, during reactive processing, extrusion or injection molding [Li, 2017], [Antunes, 2011], [Jose, 2006].

Polybond 3200 is a chemically modified polypropylene. Among the most important features are: chemical coupling agent for glass fibers, cellulose fibers and PP-reinforced mineral filler, which offers improved physical and thermal properties, compatibilizer for blends, such as polypropylene/polyamide and polypropylene/EVOH to improve processability and mechanical properties. Physical properties are comparable to other Polybond®. Polymer modified products can be obtained using lower levels of addition of Polybond 3200.

MAH-g-PP (Polybond 3200) was also used by Chow et al. [Chow, 2003], having l.2wt% maleic anhydride (MA), with a melt flow index of 105 g/10 min at 190 °C and 2,l6 kg. And Jose et al. [Jose, 2006] used Polybond 3200, but in PA12 + PP blends.

Figure 3.1 shows a) the morphology of the model elaborated by Chow et al. [Chow, 2003] and b) a morphology obtained by the author. The coating of PP particles, wrinkled, in order to take over the difference between the surface tensions of the immiscible polymers and the way it remains attached to the PA6 matrix by irregular fibriles.

LDPE (low density polyethylene) is a thermoplastic made of ethylene monomer. Despite competition from more modern polymers, LDPE continues to be important. It is not reactive at room temperature, except for strong oxidizing agents, and some solvents cause swelling. It can withstand temperatures of 80 °C continuously and 90 °C for a short time. Made in translucent or opaque versions, it is quite flexible and hard. LDPE has more ramifications (about 2% of carbon atoms) than HDPE, so its intermolecular forces (instant-

dipole-induced dipole attraction) are weaker, tensile strength is lower and its resilience is higher. Also, because its molecules are less tight and less crystalline due to the lateral branches, its density is lower.

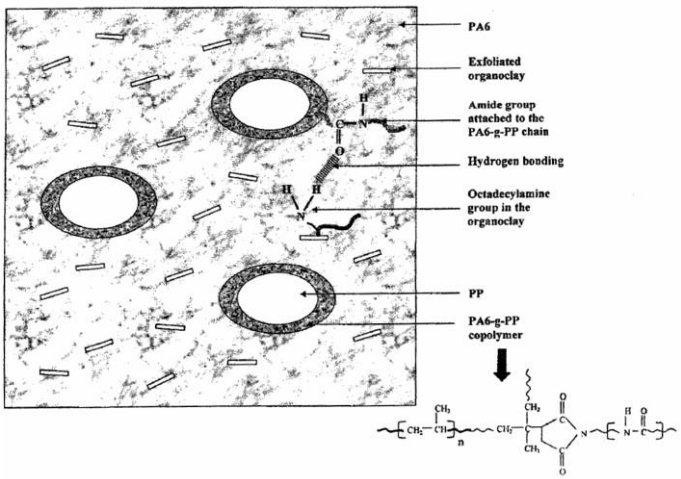

a) model proposed b Chow [Chow, 2003]

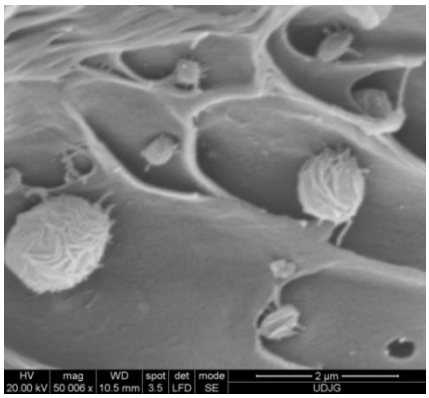

c) SEM image, after tensile test with 250 mm/min, for the blend 80% PA6 +5% PP+5% LPDE+3% Polybond 3200+7% $CaCO_3$

Fig. 3.1 Model and model confirmation for material D

$CaCO_3$ (calcium carbonate) is one of the most popular mineral fillers used in the plastics industry. It is widely available worldwide, easy to grind or reduced to a specific particle size, compatible with a wide range of polymeric resins. As an additive in plastic compounds, $CaCO_3$ helps lowering surface energy and provides opacity and surface gloss, which improves the surface finish. In addition, when the particle size is carefully controlled, $CaCO_3$ helps to increase both the impact strength and the flexural modulus (stiffness).

EPDM is a synthetic rubber, ethylene-propylene-diene-monomer, mixed with carbon black, oils, vulcanizing agents and other auxiliaries, chemically stable, with UV and ozone resistance, practically, unlimited. EPDM maintains its physical and chemical properties (elasticity) between - 45 °C and 130 ºC, remaining unaffected up to 250 ºC. Being an elastomer, it is elastic, returning to its initial position after elongation, with superior elongations at break up to 400...500%. [Hasanpour, 2019], [Ma, 2019].

The **Kritilen®Black** brands are concentrated amorphous carbon in a polymeric carrier and offer a convenient way to incorporate amorphous carbon into thermoplastic and improve UV resistance, without dust contamination and provide a good dispersion, essential to product opacity . Due to the small size of amorphous carbon particles (20-30 nm) and their very good dispersion in the carrier polymer, this product improves also the extracting process from mold. For PP it is recommended to use PP940 [Kritilen Masterbatches, 2020].

3.4. Processing of Formulated Blends PA6+PP and Compatibilizers

There are different technologies for obtaining PA + elastomer maleate + clay blends [Chow, 2003], [Li, 2017], [Ahn, 2006].

Figure 3.2 schematically shows the laboratory technology for obtaining the materials developed by the author, with the help of the research company Monofil SA Săvinești.

Description of the Processing Steps

Pre-mixtures of PA6, PP, LDPE and Polybond 3200 granules are performed in a mixer (high speed mixer), with a capacity of 200 l, mixing speed 475/950 rpm, provided with heating system with electric resistances of 11 kW and pneumatic discharge system. Pre-mixing of components in a mixer before being introduced into the extruder is important

because the used raw materials have different densities and, implicitely, a high tendency of stratifying on density if they are not pre-mixed. Thus a higher degree of dispersion is realized.

Pre-mixing drying: mixtures of polymers and additives from the high speed mixer will be placed in a drying hopper, at a temperature of 80-100°C. The dryer is equipped with an automatic mixing loading and unloading system, with a capacity of 1500 l and a working flow of 200 kg/h.

The premixtures in the drying hopper are automatically loaded into the primary dosing system. The primary dispenser has the following technical data: dosing flow = 150 kg/h, dosing system = with double screw, dosing speed = max100 rpm; feed hopper volume = 150 l.

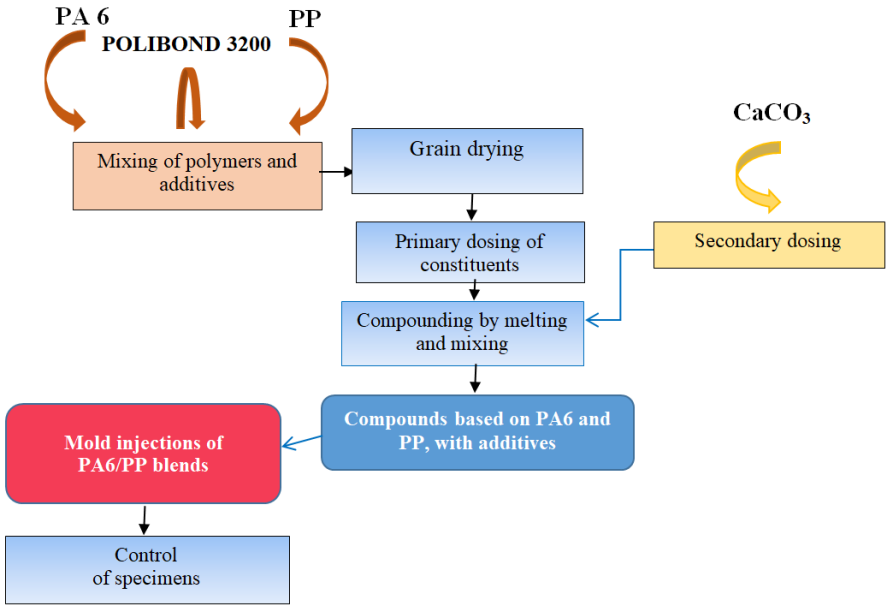

Fig. 3.2. The technological flow of obtaining the first class of polymeric blends, based on PA6 and PP

Fig. 3.3. EC 52 double screw granulator extruder (SC Monofil Săvinești SA)

The secondary dosing system will be used in the laboratory processing to introduce the compounding agent directly into the melt, in the case of the first family of mixtures, it is $CaCO_3$. The secondary dosing system has a dosing capacity of 80 kg/h.

The compounding of the mixtures of polymers and additives was performed on a granulating extruder type EC 52 with double screw, with simultaneous rotation.

The extruder is equipped with a cooling system of the zones using cooled softened water, with a vacuum pump (with a power of 2.2 kW), with water jacket, respectively, a hydraulic system for continuous filtration of melts provided with an engine of 1.5 kW and a maximum working pressure of 20 MPa.

Because the quality of the composite or thermoplastic blends depends on many factors, such as temperature, screw rotation speed, extruder length, the optimal technological parameters that will be used to make these polymer blends are indicated in Table 3.3. Table 3.4 comparatively shows some processing parameters.

The extruder cylinder (Fig. 3.4), has a modular structure, each module having a length to diameter ratio of 4 (L/D). Module 1 is provided with a supply port for additived polymeric matrices. Module 5 is provided with a hole located at the top for ventilation and/or feeding with long fibers and a side hole for dosing chopped organic or inorganic fibers and/or mineral fillings. Module 9 has a hole for the injection system.

Table 3.3. Technological parameters

Parameter	**Musteață**	**Ahn [Ahn, 2006]**
Machine	**Extruder machine type EC52 with double screw with simultaneous rotation, diameter 51.4 mm**	Haake extruder with double screw with 30 mm diameter, wheel 26 mm and a length of 305 mm.
Processing temperature, °C	**130-150** **240-260 (PP: 170...190)** **220-230 (PP: 170...180)**	240 280 (injection nozzle)
Rotational speed, rpm		280
Power supply flow		980 g/h
Mold temperature, °C		80
Injection pressure	**50...60 bar**	70 bar
Maintenance pressure		35 bar
Maintenance pressure time in mold for cooling, s		9.0

Table 3.4. Optimal compound processing parameters

No.	Technological parameters	UM	Values
1	working temperature on the 3 zones (from 9 available on the equipment): Zone I Zone V Zone IX	°C	 130-150 240-260 220-230
2	screw diameter	mm	51.4
3	ratio L/D		40:1
4	maximum rotary screw speed	rpm	600
5	modular screw structure, with 5 types of sections of different lengths	mm	16-48
6	axial pressure	kN	4,5-5,5
7	melt pressure	bar	50-60
8	melt temperature (nozzle)	°C	90-100
9	supply current intensity	A	24
10	main engine power	kW	55

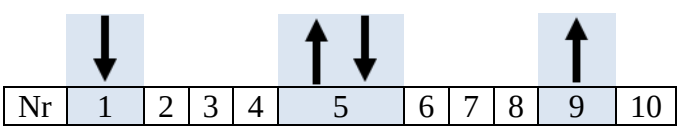

Fig. 3.4. Recommended cylinder configuration

Chapter 4
Characterization of Elaborated Materials by Tensile Tests

4.1. Introduction (Standards, Specimens)

General mechanical properties have been introduced to facilitate comparison to other classes of materials. In the use of plastics in engineering, these properties have a limited applicability. The reason is that the results are obtained on tests with relatively short investigation times and the use of information is restricted to quality control and, perhaps, to the initial selection of the material, depending on strength, resilience etc. Design based, for example, on the modulus of elasticity obtained by short-term tests will not accurately estimate the behavior of polymeric materials because they are viscoelastic, which means that the properties are sensitive to: deformation rate, stress, stress history, temperature and what is more difficult to estimate is the simultaneous and synergic influence of these factors on their behavior. Even the specimen processing puts its mark on the mechanical behavior of the materials; a component, even identical in size, will not behave in the same way as the test specimen if they were not obtained under the same conditions [Brown, 2002], [Musteață, 2016].

Tensile testing of plastics is covered by ISO 527, also adopted in Romania [SR EN ISO 527-1: 2020], [SR EN ISO 527-2: 2012], and the different parts of the standard refer to different types of polymeric materials and their composites, such as cast and extruded materials, foils, unidirectional or orthotropic fiber composites, high performance composites. The tensile test is normally performed at one of the standard rates, chosen from a set of values in the standard or from the test machine technical book.

For traction, the results of these tests are expressed by means of the relations:

real tensile stress $\sigma = F/A$ (4.1)

tensile stress at traction (engineering) $\sigma_{eng} = F/A_0$ (4.2)

relative strain at traction (engineering) $\varepsilon_{eng} = \Delta L/L_0$ (4.3)

where F is the force applied at time t, A - cross area of the specimen at time t, A_0 - initial cross area of the specimen, L_0 - initial length of specimen between marks, L - the length between marks, at moment t.

If the engineering values are known, the relations used in this paper to calculate the real values are:

- real relative strain $\varepsilon_{real} = \ln(1 + \varepsilon_{eng})$ (4.4)
- real tensile stress at traction $\sigma_{real} = \sigma_{eng}(1 + \varepsilon_{real})$ (4.5)

The shape and dimensions of the specimens used in the tensile test are given in Fig. 4.1.

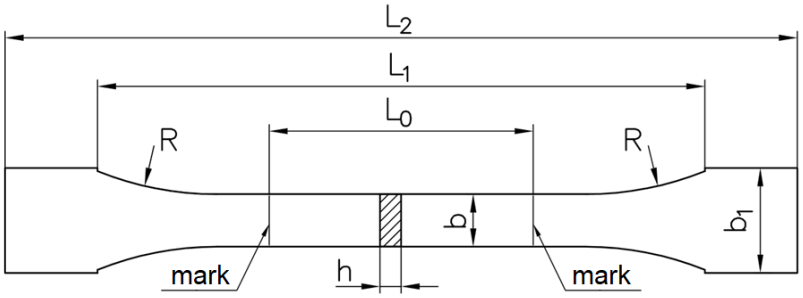

Type 1A
$L_2 \geq 150$ mm
$L_1 = 115$ mm
$L_0 = 50$ mm
b=10 mm
h=4 mm
b1=20 mm

Fig. 4.1. Sample dimensions, according to SR EN ISO 527-1:2020 [SR EN ISO 527-1:2020]

4.2. Testing Machine, Test Procedure and Measured and Calculated Parameters

The test procedure of the injected samples from the blends designed by the author was according to SR EN ISO 527-1: 2020 Plastics. Determination of traction properties. Part 1: General principles.

The specimens were tested on the INSTRON 2736-004 tensile test machine (from the INCAS advanced materials laboratory). The specimens are of type 1A, in the shape of a dumbbell, according to SR EN ISO 527-2 [SR EN ISO 527-2, 2012].

4.3. Tensile Characteristics for Blends Elaborated Based on PA6 and PP

4.3.1. The First Family of Formulated Blends

Initially, the author structured the research plan on a family of PA6 + PP blends, with an adhesive (Polybond 3200), a compatibilizing agent (LDPE) and a dispersing agent ($CaCO_3$). The same concentrations of adhesive and dispersing agent were maintained in all blends. The four blends, for which PA6 varies between 20-80% wt, were tested and presented in [Musteață, 2019], [Musteață, 2018], [Musteață, 2018].

The standard SR EN ISO 527-2:2012 provides for the calculation of the average for five tests, for which the specimens are broken almost centrally, in the area thinned by a constant section of the specimen. Sufficient tests were performed for each material, between 5 and 11, so that five representative tests with similar stress-strain curves could be selected.

Figure 4.2 shows only real stress-strain curves for extreme test speeds (v=10 mm/min and v=1000 mm/min) (calculated with relations (4.4) and (4.5)) for five tested specimens. The tests were performed for four deformation speeds 10 mm/min, 250 mm/min, 500 mm/min and 1000 mm/min, respectively.

It is observed that all curves, for all test speeds, have three distinct areas:

- a linear portion, wider for higher test speeds (elastic proportionality area),
- an elasto-plastic curved area,
- a slightly convex bearing, after which the tension drops suddenly, indicating that the specimen has broken.

The PP material is quite predictable, due to the tendency of the curves to overlap, except for the tensile stress at break which varies by almost 80% at the lowest speed and much less at higher test speeds, the average tensile stress at break for the other three test speeds varies between 8.6% and 9.9%.

Material A has similar stress-strain curves for all test speeds, except that at the speed test v=1000 mm/min, the sample is not broken abruptly but after a very steep curve, probably the result of the addition of PA6 and of polybond. In the literature, the addition of $CaCO_3$ can also contribute to a progressive failure of the specimen. Unlike PP, for material A, the tensile stress at break has much lower values, their range narrowing at higher test speeds but remaining with the minimum value around 3%.

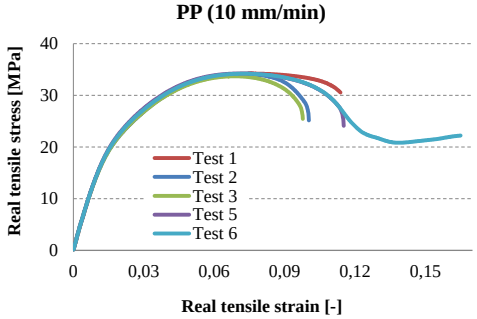

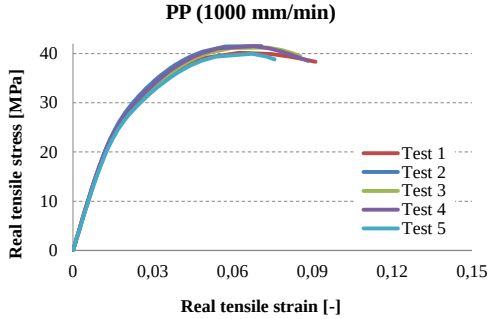

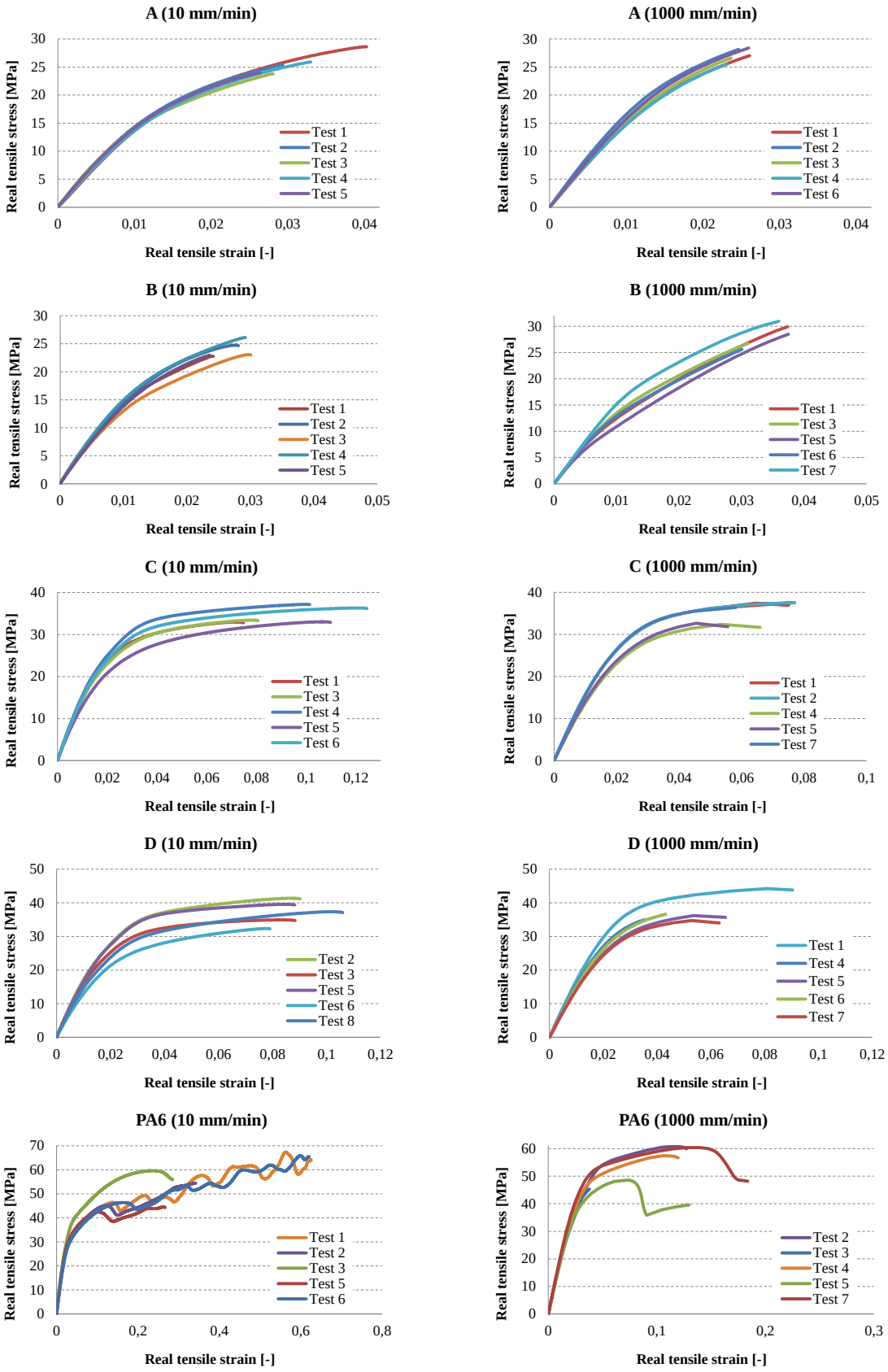

Fig. 4.2. Stress-strain curves, for the first tested family of blends

The morphology in the breaking surface of material A (Fig. 4.3) is different depending on the test speed. At low speed (v=10 mm/min), the PP matrix has time to deform and the

failure has locally elongated fibers, until breaking; there is a reduced adhesion between the PA6 droplets and the matrix and the $CaCO_3$ particles, unevenly distributed and trapped on the the breaking surface of the matrix or on the surface of the PA6 droplets. At higher speeds, the failure is of brittle type and in c) a drop of PA6 with interface from the compatibilizing agent is seen. Smaller drops of PA6 are embedded in the PP matrix.

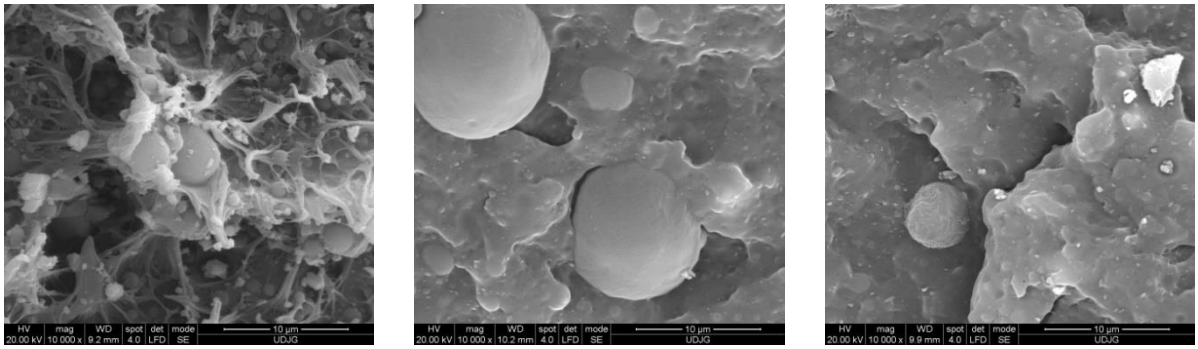

v=10 mm/min v=250 mm/min v=1000 mm/min

Fig. 4.3. Morphology of material A, depending on the test speed

The flow level of material C is due to the presence in a high percentage (60%) of PA6, and from the study of SEM images with EDX analysis it was found the reversal of the role of constituents: PA6 becomes matrix and PP is dispersed as droplets. It is observed that the PA6 matrix has large local deformations in the tensile breaking section.

B **C**

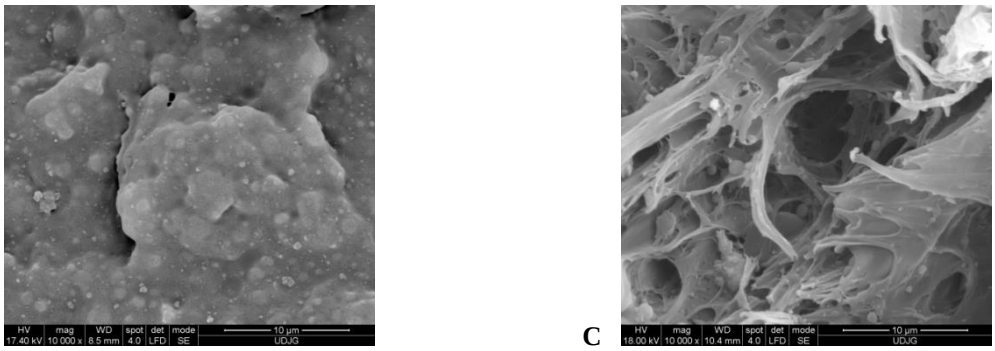

Fig. 4.4. SEM images of materials B and C, at v=250 mm/min

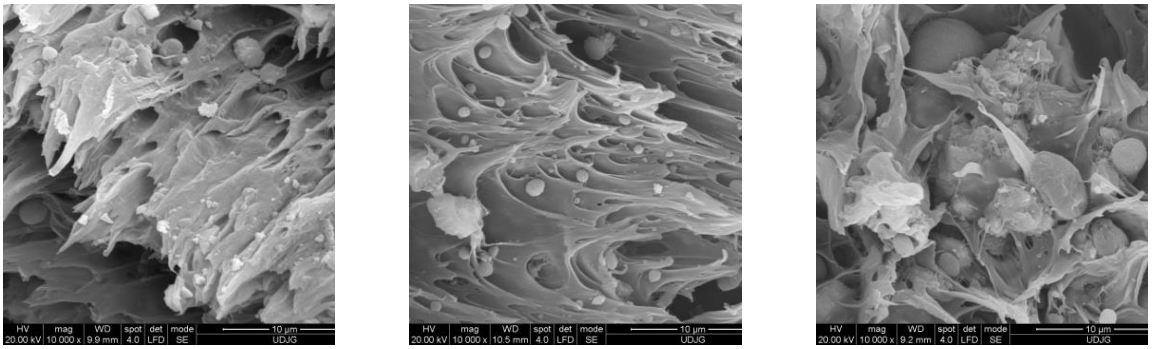

a) v=10 mm/min b) v=250 mm/min c) v=1000 mm/nin

Fig. 4.5. SEM images of material D on the breaking surface

Material D has the highest concentration of polyamide (80%) which explains the scattering of flow bearings, between 30 and 38 MPa for v=10 mm/min, between 35...42 MPa for v=250 mm/min and v=1000 mm/min. The presence of polyamide as a matrix determined a tensile strain at break interval of 4% for v=10 mm/min. At lower test speeds, the values of

the tensile stress at break were below 10% for v=500 mm/min and v=1000 mm/min. The first part of the stress-strain curves overlapped, which means that the material is predictable. The scattering of tensile stress at break can also be caused by the presence of cavities obtained by laboratory technology and which are proof of the immiscible nature of the two basic polymers and most likely, of a still inadequate processing regime.

In Fig. 4.6 are presented the photos of the sets of five specimens tested for material A, depending on the test speed.

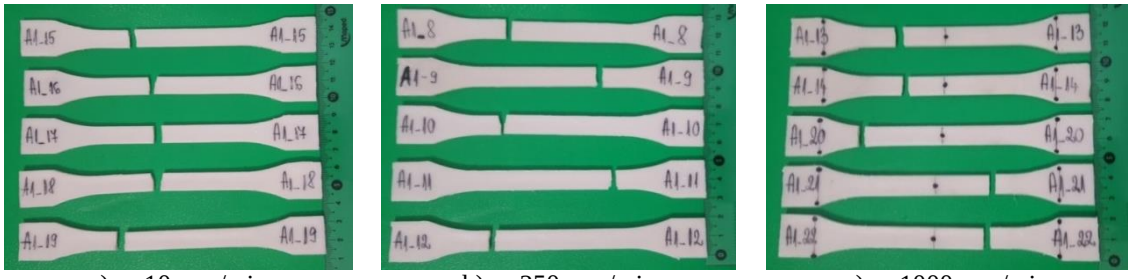

a) v=10 mm/min b) v=250 mm/min c) v=1000 mm/min

Fig. 4.6. Material A - test specimens after tensile testing

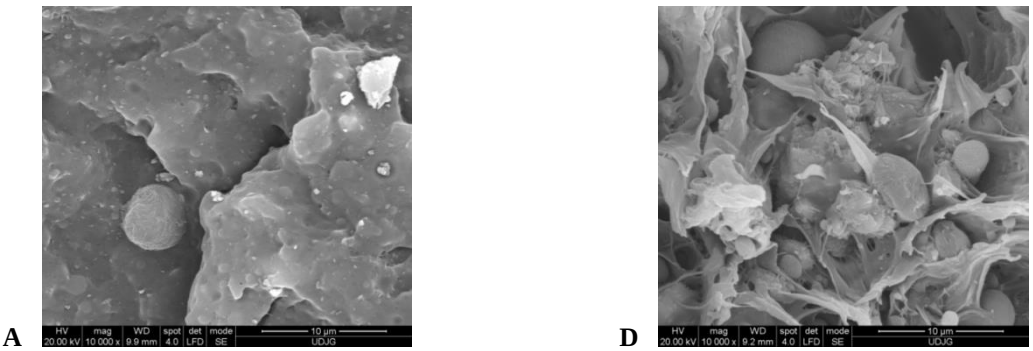

A **D**

Fig. 4.7. SEM images of materials A and D at v=1000 mm/min

Figure 4.7 highlights the difference in the morphologies of blends A and D, on the broken surface, supporting the explanation for a higher value of the tensile breaking energy of material D. It is observed that material A has finer droplets of PA6 embedded in the PP matrix and also larger droplets (bottom left) wrapped in the compatibilizer and with $CaCO_3$ dispersed fairly evenly, but with particles quite different in size. Here, the rupture is fragile in nature, without large plastic deformations of PP. Material D, having the matrix of PA6, shows large, local plastic deformations of the matrix with locally elongated fibrils and PP drops unevenly attached with fibrils in the matrix.

Unlike the literature consulted for metallic materials [Găvruș, 2009], [Găvruș, 2012], [Johnson, 1983], which show that the tensile stress increases with the increase of the deformation speed, for the materials from the first family this trend is not clearly formulated by the experimental results. For example, for PP, the increase of the strength at break with the deformation rate is evident, from v=10 mm/min (σ_r=22.8 MPa), to v=250 mm/min (σ_r=33.4 MPa), then the increase is very small, from 33.5 MPa (at v=500 mm/min) to 36.3 MPa at v=1000 mm/min. For the other materials, the minimum value is obtained at v=10 mm/min, but for the other test speeds, the values are not ordered according to the test speed and are very close. For PA6, for v=10...500 mm/min, the value of the characteristic is almost the same, the only much differentiated value being for v=1000 mm/min (σ_r = 47.7 MPa).

The lowest values of the tensile stress at break were obtained for A (20% PA6) and B (40% PA6), the values being too close to be able to highlight a clear dependence on the test speed. And for C and D, the difference between the values at the same test speed is

insignificant. For PP, the tensile stress at break varies by only 4% between values at test speeds 10...1000 mm/min. For material A, the tensile strength is reduced by only 4,4% from tests performed at v= 10 mm/min compared to those performed at v=250 mm/min, and for material B this difference is 3,1% , for material C is high, of 42.5%, and for material D - 9.0% and for PA6-69.7%. This recommends blends A and B for parts that require dimensional stability to breakage.

The minor phase coalescence in the PA6 matrix (materials A and B) is restricted by clay (in this study, $CaCO_3$), and the interfacial adhesion was improved based on the elastomer, in material G. In the ideal model, clay or $CaCO_3$ acts more first reducing the average diameters of the dispersed particles and stabilizing the morphology of the phases and the elastomeric compatibilizing agent acts after increasing the interfacial adhesion between the dispersed particles and the matrix.

4.3.2. Analysis of the Morphology of Blends from the First Family

Cracked surfaces were observed using an SEM scanning electron microscope, after a thin layer of gold was deposited to increase local electrical conductivity and improve the resolution of SEM images.

Morphology can be analyzed at the macro and micro level. Everyone can give details about how the test tube behaved and the microstructure of the blend from which the test piece is made. When PP + PA6 blends are required with a tensile load, a certain fraction of the total deformation is absorbed by the conservative deformation of the material. In the PP matrix, the deformation results from a combination of amorphous hyperelastic phase and crystalline plasticity. The PA6 phase is also capable of deforming plastically, but its flow stress falls in the plastic domain and has a much higher value than that of PP [G'Sell, 2004]. Consequently, in PP/PA6 blends, particles isolated from PA6 show a lower deformation than the PP matrix, which leads to surface tension concentrations. Instead, the insulated POE nodules deform due to the compatibility properties of the rubber.

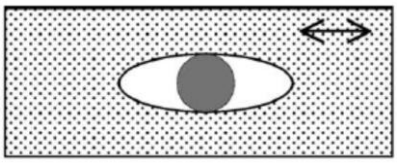

Fig. 4.8. Debonding at interface PP/PA6 [Bai, 2005]

One type of damage mechanism is surface tension (finally producing interfacial debonding). Due to the contrast of mechanical properties of adjacent materials, the induced stresses break the weak adhesion, leading to debonding of the matrix (here, PA6) preferentially as in Fig. 4.8 where the tensile load is applied horisontally. One may notice that the drop is only attached to the matrix at poles. Surface tension is mainly active for particles isolated in the matrix [Bai, 2005].

Cavitation is one of the main processes of energy dissipation during the deformation of polymer blends, which influences their behavior during impact testing [Utracki, 2002], [Sharma 2012]. Cavitation decreases the hydrostatic stress in the matrix, increases stresses and promotes shear deformation.

Of blends A, B, C and D, only blend A has no visible gaps or pores in the failure section. The other materials have, as a result, the technology and / or the additives do not improve the injection molding of the specimens. Although $CaCO_3$ has been used in the literature for the compatibility of similar blends [Sharma 2012], in this case, it fails to maintain the polymers without cavity gaps when cooled in the mold.

The morphological analysis of the formulated blends can be performed according to two criteria:

- the influence of the test speed on the breaking appearance of each material,

- the influence of the concentration of the components at the same test speed.

Next, the analysis will be done according to the first criterion.

In Fig. 4.9, the traction fracture surfaces for PP specimens are shown. It is observed that at low speed the surface of the fragile failure is relatively larger and towards the center of the specimen, and the flow is obvious around this area. For the other speeds, the surfaces look similar at the macro level. The failure seems fragile on a much larger surface, the flow being observed only locally.

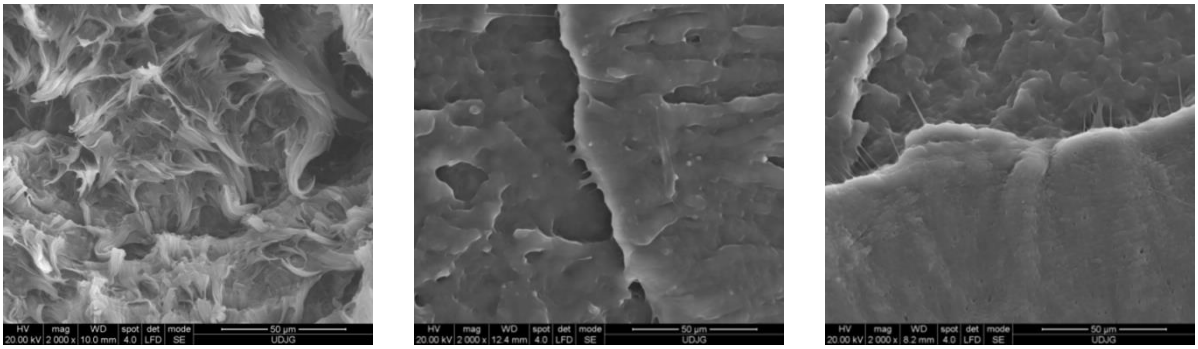

a) v=10 mm/min b) v=500 mm/min c) v=1000 mm/min

Fig. 4.9. Differentiation of tensile strength for the same material (PP), depending on test speed (magnification x2000)

For PP, at the micro scale (50 μm), large differences in appearance are observed between v=10 mm/min and v=250 mm/min. Due to the low traction speed, the polymer flows locally, resulting in some fibers that elongate locally and thin to break. It is a specific process of breaking thermoplastic polymers at low tensile stress rates and the spatial orientation of the fibrils is approximately in the direction of stress of the specimen. The curvature of the tips of the broken fibrils is due to the relaxation of the material. This process of breaking with the fibers also causes the appearance of micro gaps due to the flow of the material in micro volumes. As the demand increases, these fibrils elongate and break, the micro gaps created can join and cause the macro-breaking process. At v=250 mm/min, this micro-volume fibrillation process is no longer visible. The fibrillation tendency can be observed, but the fibrils can no longer develop because the material yields quickly, on the entire surface.

At the highest speed, v=1000 mm/min, the fibrils are sparse and very thin suggesting a sudden stretching of a more plastic micro volume. In the lower right, there are also very small pores caused by strip-like landslides on the breaking surface. The macro appearance of the breaking surfaces for material A differs only at the lowest test speed, the appearance being rougher and with obvious flow areas but scattered over the entire surface.

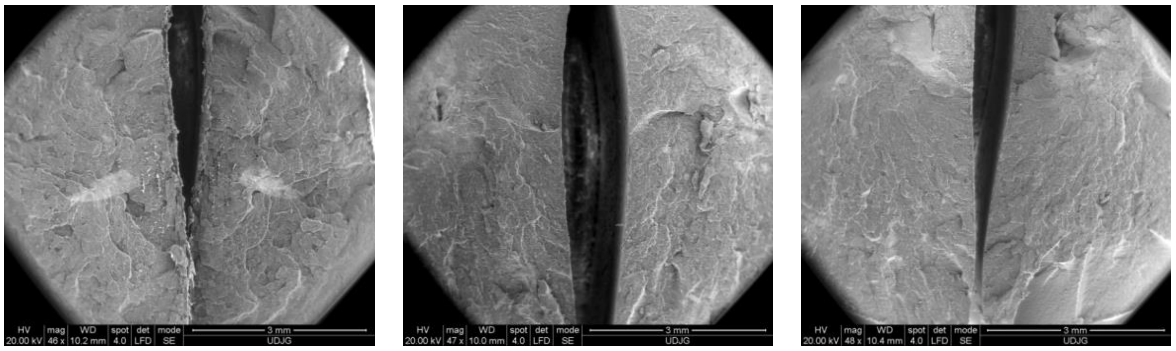

a) v=10 mm/min b) v=500 mm/min c) v=1000 mm/min

Fig. 4.10. Differentiate the tensile strength for the same material (material A), depending on test speed (magnification x50)

In Fig. 4.11a, in blend A, it is observed that the dispersed polyamide droplets are elongated and broken like small short fibers. Also in this image you can see drops of PA6 discovered by breaking the matrix and which have an almost spherical shape. It is observed that some drops of PA6 do not have a very good adhesion to the PP matrix, as evidenced by the gap formed around them, once due to surface tension and due to the difference in expansion coefficients. In Fig. 4.11b the dispersion of polyamide droplets in the PP matrix, some $CaCO_3$ particles and a crack in the matrix due to the stress are very well observed. The polyamide droplets are no longer fibrillated and the failure was performed at the droplet-matrix interface. It is observed that some drops were torn off and small spherical slots remained on the breaking surface.

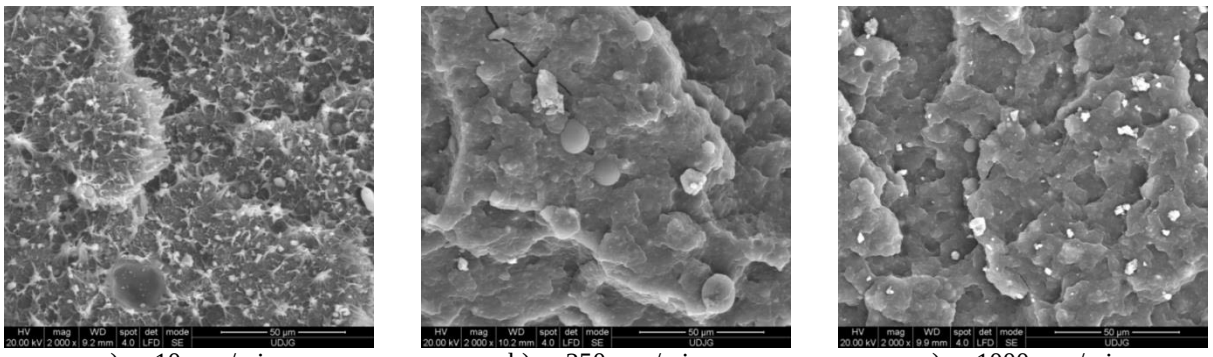

a) v=10 mm/min b) v=250 mm/min c) v=1000 mm/min

Fig. 4.11. Differentiate the tensile strength for the same material (material A), depending on test speed (magnification x2000)

At higher speeds, the brittle failure of PP is observed with the formation of micro gaps between areas with small differences in mechanical properties. It may be seen also $CaCO_3$ particles that have different sizes, from a few microns to 5-10 microns.

For material B, the same trend is observed as for material A, fibrillation of polyamide droplets at low speed and pore formation due to tensile stress. Gaps appear at higher speeds due to stress and the dispersion of PA6 droplets and $CaCO_3$ powder on the breaking surface is observed. It is possible that some micro cavities result from the cooling process of the test tubes and only be enlarged following the stretching request.

Material C also showed cavities resulting from the injection and cooling process. The aspect of failure does not differ much from v=10 mm/min to v=250 mm/min. Instead, the micro analysis looks different for the two test speeds (Fig. 4.12).

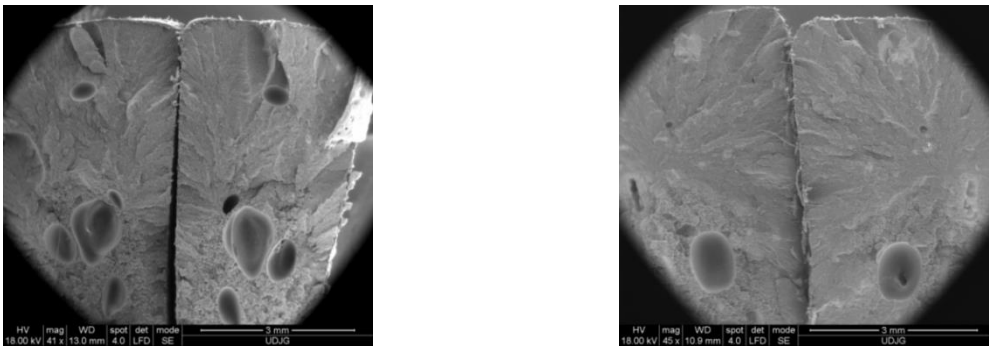

a) v=10 mm/min b) v=250 mm/min

Fig. 4.12. Differentiate the tensile strength for the same material (material C), depending on the test speed (magnification x40 ... 45)

Making an EDX analysis, it can be seen (Fig. 4.13) that the drops in blend C have in the elemental composition carbon in large proportion, specific to polypropylene, $(C_3H_6)n$ and

oxygen and calcium, elements characteristic of calcium carbonate. In Fig. 4.13b, the EDX analysis of the matrix highlights the presence of nitrogen, nitrogen being only in the composition of the molecular chain $(C_6H_{11}NO)_n$.

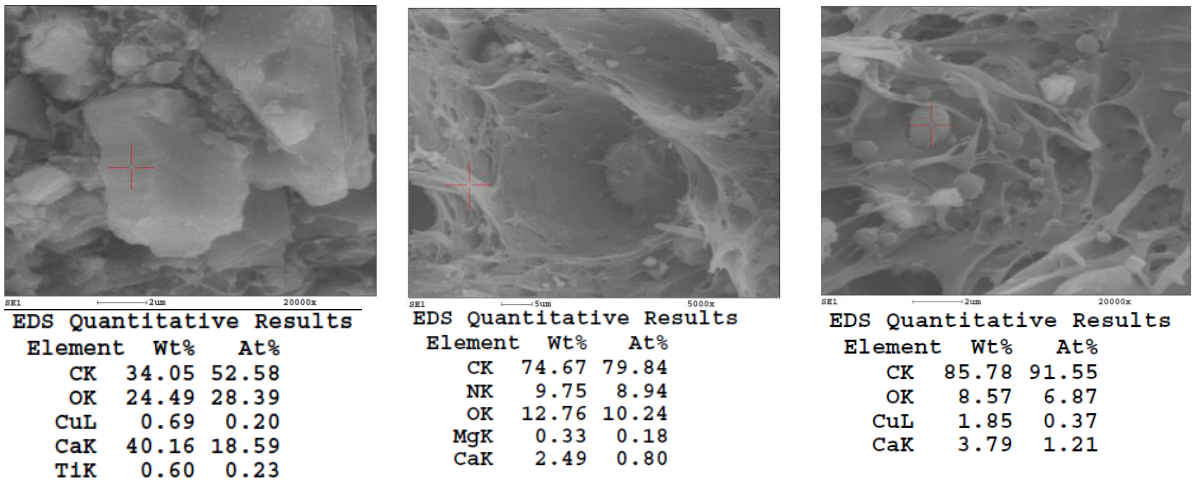

a) presence of $CaCO_3$ b) polyamide c) polypropylene

Fig. 4.13. EDX analysis of material C (tensile breaking surface with test speed of v=250 mm/min)

This shows that between the concentration of the components in material B and the concentrations of the components in material C, a reversal of the blends was made, in the sense that the polyamide became a matrix and the polypropylene is found in the form of droplets in this matrix. The droplets are attached to the matrix either over the entire surface or through the fibers. At the tensile stress, local flows in the form of threads are observed on the breaking surface, which caused the crazing process to be much more visible and present on the whole breaking surface compared to the rare crazing from materials A and B.

All specimens in material D showed the same aspect of failure at the macro level, had micro cavities oriented in the direction of injection of the material. The formation of macro cavities during the cooling of the specimens due to the interfacial tensions between the two immiscible polymers is characterized by very elongated ellipsoidal shapes in the injection direction, very smooth walls.

About 20% of the samples in PA6 had gaps. Decohesion (detachment) of particles from the matrix is an important mechanism of deterioration in polymeric blends with ductile matrix (such as PA) and weakly adherent particles (such as PP when constituting the dispersed phase). This mechanism also appears in the blends of PP + PA + POE [Bai, 2004].

Macro-scale gaps may occur due to inadequate processing parameters. Cavities also occur if the volumes on the surface of the injected elements solidify too quickly and the contraction is located inwards. So the cavities are associated with molds that are too cold to melt. Causes can also be an insufficient volume of melt in the machine, incorrect processing conditions (pressure, temperature, time and speed of injection and maintenance), wet materials. It can be avoided by re-designing the injection process. Specialists [***Polyamide (Nylon) - Troubleshooting Common Nylon Processing Problems], [***DUPONT™ ZYTEL® AND MINLON® Nylon Resins Molding Guide] recommend: drying the constituents, raising the melting temperature and more precise control over the processing areas, increase of the mold temperature, increase of the injection and maintenance pressure, increase of the injection time, increase of the supply in the melt distribution system, especially if the buffer zone is small, decrease of the supply area if the buffer zone is too big, relocation of the intake routes melting, removing thick-walled sections.

Figure 4.14 shows details of the breaking surfaces for materials A and D. Comparing the SEM images at the same scale, the following can be observed:

- different behavior of material matrix A (from PP) and material matrix D (from PA6),
- phase reversal is observed: for material A, the drops are PA6, for material D the drops are made of PP,
- at the lowest speed, the PP matrix forms tufts of short fibers and the PA6 matrix breaks into long fibers, on almost the entire breaking surface.

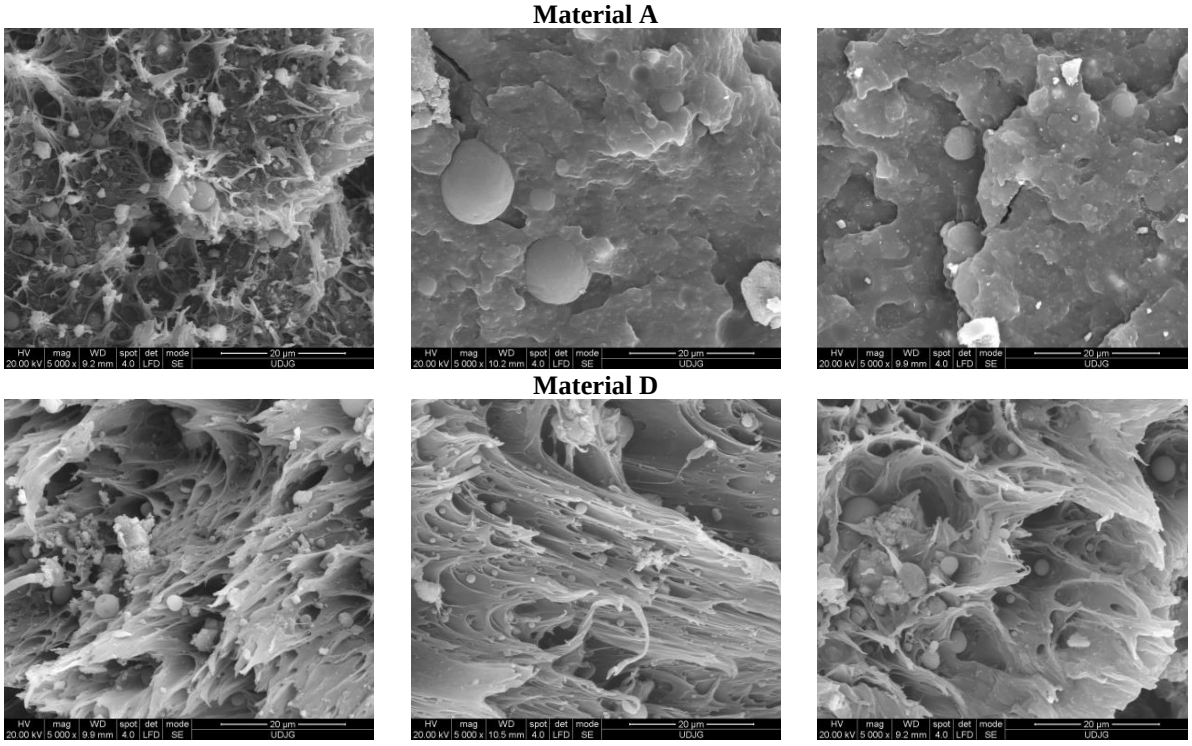

v=10 mm/min v=250 mm/min v=1000 mm/min

Fig. 4.14. Details of tensile breaking surfaces to highlight phase reversal

4.4. Conclusions from Experimental Data for the First Family of Blends

Taking into account the four formulated blends, material D (with 80% PA6) is the most promising, having the highest tensile and energy at break (11.82 J at v=10 mm/min and 7.3 J at v=1000 mm/min), but the values are lower than those of PA6.

Figure 4.15 has four mechanical characteristics of the tested materials. For PA6, in this figure, the value of the tensile stress at break (55.43%) and the energy at break (90.15 J) are not at the scale at which the author wanted to emphasize in detail the influence of the concentration of PA6 for the other blends.

Qualitatively, analyzing the graphs in Fig. 4.15, the grouping of the four blends according to the nature of the matrix is observed. For A and B, which have PP matrix, the tensile stress at break is lower than that of the constituents and for C and D, which have PA6 matrix, the tensile stress at break is lower but close to PA6.

As reported by other research [Bai, 2005], the tensile strain at break decreases when the test speed increases and this conclusion was obtained for all tested materials, except for material B which has an increased elongation at break.

The tensile strain at break also grouped the blends into two classes (Fig. 4.15b):

- materials A and B have low values (2.5% ... 3.7%), decreasing slightly with the test speeds,
- materials C and D with higher values (5.9% .. 10.3%).

The energy at break also separates the same groups of materials: A and B, with lower values (1.7 J...2.8 J) and the group of materials C and D, with values higher and a greater

dependence on the test speed: for C, this characteristic is 11.6 J at v=10 mm/min, 6.6 J at v=250 mm/min, 8.6 J at v=500 mm/min and 7.6 J at v=1000 mm/min. For material D the trend is similar, but with values higher than C (11.8 J at v=10 mm/min, 10.9 J at v=250 mm/min, 9.6 J at v=500 mm/min and 7.3 J at v=1000 mm/min.

The average values for the tensile stress at break fall in a band of 25 MPa, these being difficult to evaluate based on the test speed (Fig. 4.15a). With the exception of PP at v=10 mm/min, the lowest values were obtained for materials A and B. For C and D this characteristic increased slightly, with increasing concentration of PA6.

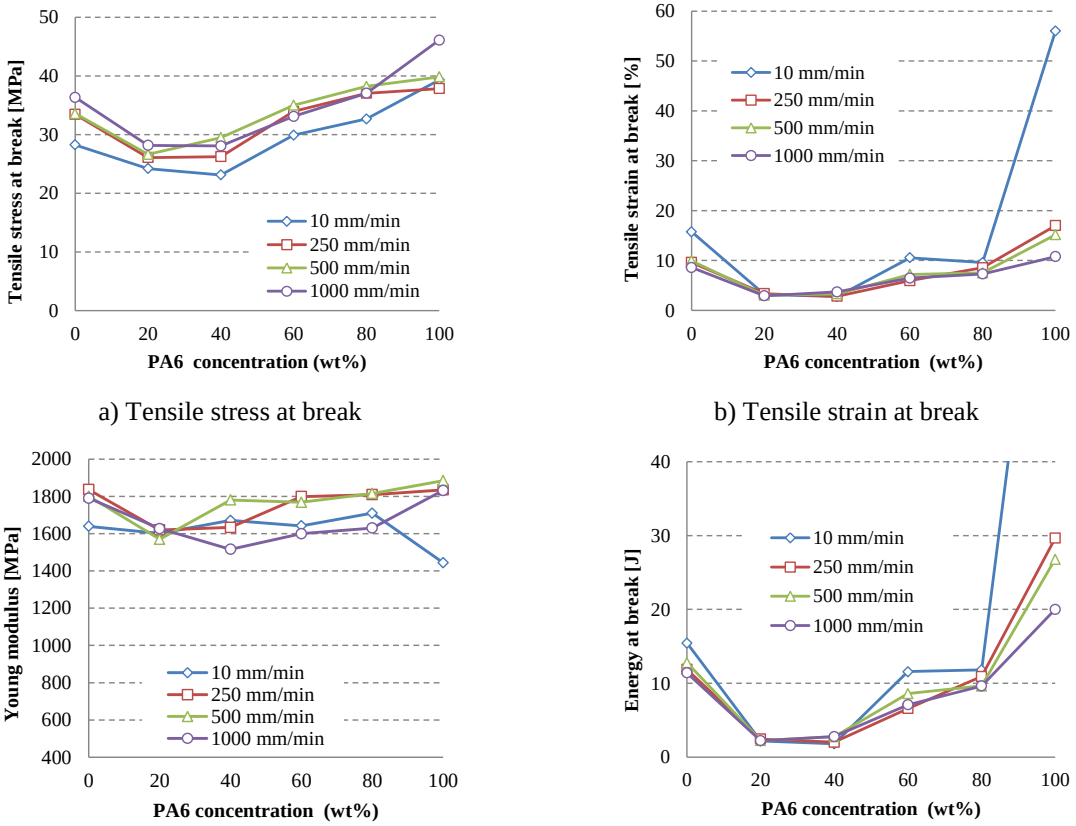

a) Tensile stress at break

b) Tensile strain at break

c) Young modulus

d) Energy at break

Fig. 4.15. Mechanical characteristics according to PA6 concentration and test speed

The increase of the PA6 content and the consequent decrease of the PP content of the blend is favorable to the mechanical properties as such:

- energy at break varies insignificantly for materials A and B at all test speeds.
- modulus of elasticity varies very little depending on the concentration of PA6 and the test speed, so we find the lowest value for material A (1569.7 MPa at test speed v= 500 mm/min) and the highest for the material D (1815.6 MPa also at test speed v= 500 mm/min), excluding base materials PA6 and PP.
- tensile strain at break remains low and less influenced by the deformation rate of the test compared to the PA6 concentration.

The technology needs to be improved to eliminate gaps in blends with a high concentration of PA6, and the research study needs to be done again.

Studying these graphs, it turned out that the tensile energy at break did not improve, but a lower tensile deformation was obtained, resulting that the parts made of materials A and B have smaller deformations on demand, which would interest a designer who requires greater shape stability.

4.5. Tensile Characteristics for the Second Family of Blends, with PP, PA6 and EPDM

In Figures 4.16-4.17, are presented the photos of the test specimen sets tested for materials G and PA6m, depending on the test speed.

Materials G and PA6m have large necks and deformations at break, characteristic of ductile materials and which, most likely, could have high tensile energy at break at traction.

a) 10 mm/min b) 1000 mm/min

Fig. 4.16. Broken tensile specimens at different test speeds for material G

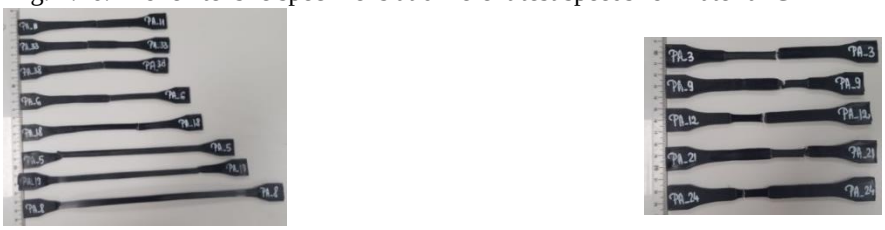

a) 10 mm/min b) 1000 mm/min

Fig. 4.17. Broken tensile specimens at different test speeds for PA6m material

Figure 4.18 shows the real stress-strain curves for the four materials tested (five tests selected as typical for each material in the second family, calculated with relations (4.4) and (4.5)), only to the extreme test speeds.

It is observed that the introduction of 1% Kritilen caused, at v=10 mm/min, first a decrease of the real tension, explainable by the reduction of the internal friction due to the presence of carbon, which is known to have a low coefficient of friction and that it is added to polymers and polymeric composites to reduce friction with another body. Then the curves of the additive polymer have an ascending slope, suggesting a hardening (an increase in strength) due to the alignment of the molecular chains. At higher test speeds, the shape of the curves is maintained for both materials.

Material H has the lowest concentration of polyamide (12% PA6). It is found that the failure occurs at very different values of deformation. In other words, the material has a predictability on which the designer can rely only in the range of 0-20 MPa, after this value, the failure can occur in a wide range of stresses, from 25 MPa to 40 MPa. The designed parts of this material should not exceed 15-20 MPa, in maximum values, so as not to increase the probability of failure. It follows that the failure of this material is unpredictable after these stress values.

Material G (42% PA6), retains some properties as in material H, with less polyamide, but has a substantial scattering of tensile stress at break. The real stress-strain curves overlap well in the area of the non-linear elastic and elasto-plastic domain, then in the plastic flow area, they are only slightly spaced, All curves have two domains, except for the curves obtained at v=10 mm/min, for which three domains can be observed: the elastic (linear) one, then a low-slope flow bearing, followed by the last one with a higher slope. This quality of behavior almost identical at the request of identical designed parts is a quality sought after by designers. The first segment has an almost linear slope, the inclination and the upper value

depend very little on the request speed. The second segment shows a more pronounced hardening plastic deformation for low test speeds (ie the slope has a higher slope) than the inclinations obtained for higher speeds.

For speeds of 250-1000 mm/min, the shape and characteristics of the curve have very small differences. There is also a slight tendency to increase the stress at break and less of the tensile strain at break.

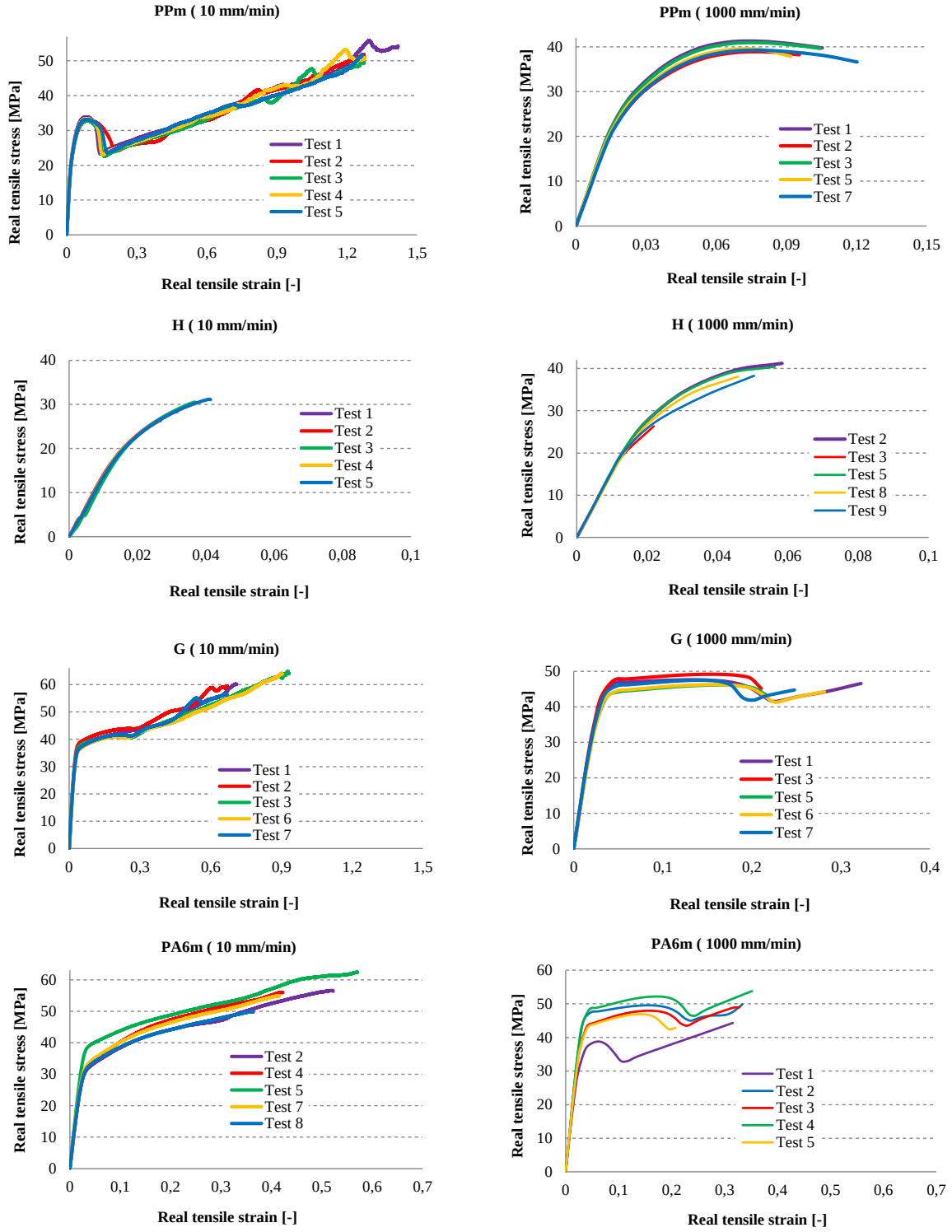

Fig. 4.18. Real stress-strain curves for materials of the second family

PA6m is a polymer blend without PP, made only from PA6 and EPDM. The elaboration of the recipe of this material was based on the results of some blends based on PA and EPDM or another elastomer [Ma, 2019], [Antunes, 2011], [Hasanpour, 2019].

Tensile tests revealed the following characteristic aspects:

- the curves for v=10 mm/min and 250 mm/min are very similar, except for an area of instability, manifested at v=250 mm/min for relative deformations between 0.2 and 0.3;

- at higher speeds, v=500 mm/min, the was made at deformations between 0.1 and 0.2, while at the highest test speed, the failure was made at deformations of 0.3-0.4 .

Figure 4.19 shows that the addition of EPDM increased the ductility of the polymeric material, but, as in PA6, and in PA6m there is a similar aspect of the same order of magnitude, of initiation of tensile fracture.

PA6 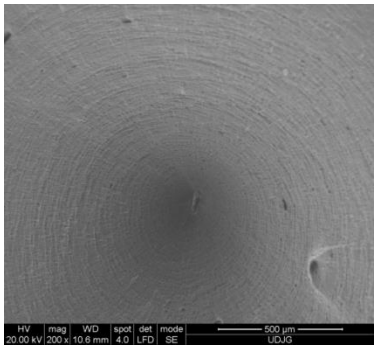 **PA6m** 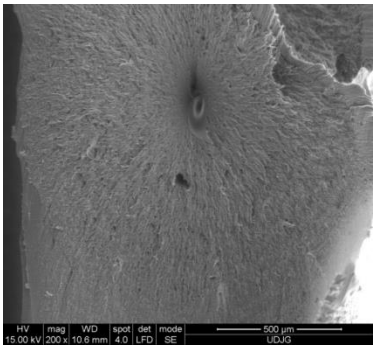

Fig. 4.19. Breaking surface aspects for test speed v=500 mm/min

If the average values of the studied mechanical characteristics are represented, for each material, trends depending on the test speed can be highlighted.

If the morphology of failure for different test speeds is studied, no large differences are observed in the shape and size of the failure fibrils, this having a ductile character.

4.6. Conclusions for the Second Family of Blends

Figure 4.20 shows the tensile characteristics as a function of PA6 concentration. In analyzing these graphs, it should be noted that only three materials contain EPDM (H, G, PA6m) corresponding to the following percentages of PA6: H - 12% PA6, G - 42% PA6 and PA6m - 60% PA6.

Of the formulated blends, PA6m behaves best, has the highest tensile stress at break, insensitive to the test speed, except for the speed of 10 mm/min. Material G does not have a clear variation in tensile stress at break depending on the test speed either.

The tensile strain at break has high values for PPm considering that without 1% Kritilen, the fracture deformation value is 15%. It follows that the addition of kritilene favors the slipping of PP molecules and excessive deformation of the specimen, even without breaking.

The evolution of the tensile stress at break for speed v=10 mm/min differs from the evolutions at other speeds. For each material, the speed increase between 250 and 1000 mm/min, does not have a clear tendency of dependence on speed, the values of tensile stress at break being grouped over a range of 10-15%.

The value of the tensile stress at break increased for PA6m, even more than that of polyamide. Of the blends (H, G, PA6m), the lowest values were obtained for the blend with the lowest PA6 concentration, namely material H.

For Young modulus, the lowest values were obtained for speed v=10 mm/min for any of the tested materials. For the other three speeds, the values of this material characteristic are included in a relatively narrow band of ~100 MPa representing less than 6-8% of the total value, which leads to the conclusion that this parameter is not sensitive to the test speed over the tested range. The lowest values were obtained for PPm (1307 MPa at v=10 mm/min), and

the addition of PA6 in the composition of the other blends led at a slight increase in Young's modulus for these blends, namely blends G and H. The highest values were obtained for simple polyamide 6, tested in the first family of materials.

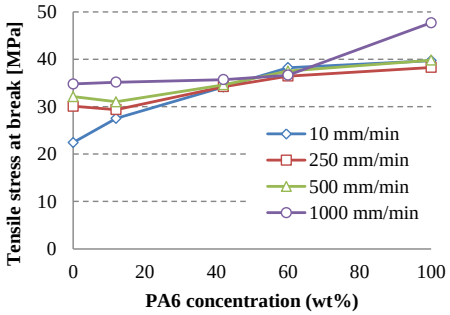

a) Tensile stress at break

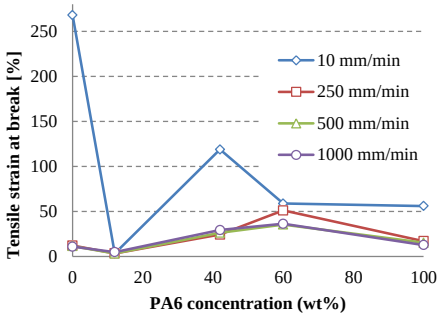

b) Tensile strain at break

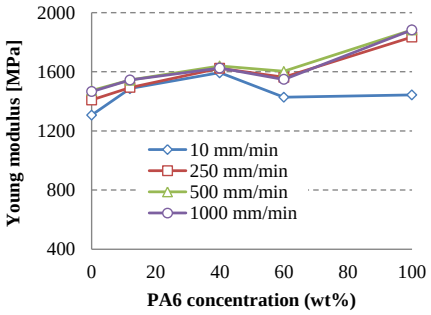

c) Young modulus

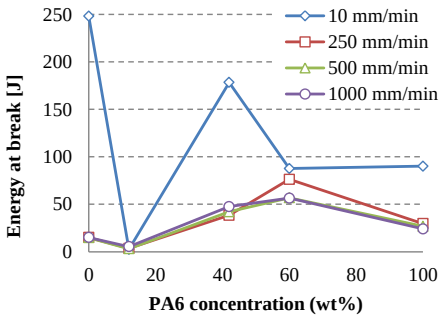

d) Energy at break

Fig. 4.20. Mechanical characteristics according to PA6 concentration and test speed

Energy at break. Regarding the modified polypropylene (PPm), at speed v=10 mm/min, the results of the energy at break are not conclusive because the tests were made for a maximum elongation of 250%, during which time none of the tested specimens broke. The average value for five tests, recorded by the machine for the energy at break to be tested was 248.14 J. Starting with the speed v=250 mm/min, the ductile character of the PPm disappears, the average values for the energy at break being very close on the tested interval. The lowest values of tensile energy at break were obtained for material H, highly grouped, around 2.5 J. For material G, the values of energy at break are higher and grouped for 250...1000 mm/min.

At v=10 mm/min, material G had the highest energy at break value (178.36 J). For PA6m, the highest values of energy at break were obtained, 76.34 J. At v=10 mm/min, the polyamide has values close to that of the PA6m material, but for the other test speeds, the values fall to less than half that of the PA6m material.

In conclusion, materials with high values for energy at break for high test speeds (v=250...1000 mm/min) were obtained in descending order for PA6m, G and PA6. From this study, it results that G and PA6m materials have this improved characteristic compared to the basic constituents (PP and PA6), although two other characteristics, Young modulus and the tensile stress at break are only slightly influenced by the test speeds.

4.7. Characteristic Morphology of PA + PP + EPDM and PA + EPDM Blends

4.7.1 Morphology of Similar Blends in Literature

To improve the impact resistance of PA-based materials (composites or polymer blends), the researchers investigated the influence of elastomers on the behavior of newly formed materials by adding elastomer. Research has been done for styrene-ethylene / butylene-styrene tribloc copolymer (SEBS) [Li, 2017], [Kusmono, 2008], ethylene-propylene random copolymer (EPR) [Ahn, 2006], ethylene-polypropylene-diene copolymer (EPDM) [Hasanpour, 2019], [Antunes, 2011], [Ma, 2019] and metallocene EPDM / maleated EPDM

copolymer (mEPDM/EPDM-g-MA). Impact resistance is usually improved to the detriment of strength and dimensional stability. The rigidity of polyamides with the addition of elastomer can be preserved to some extent by inorganic additives (glass micro spheres, short glass fibers, minerals and clays, carbon nanotubes and organic [Boțan, 2014].

In contrast, the impact resistance of polyamides can be improved by including an impact resistance modifying agent in the blend.

4.7.2. Morphology of Formulated Blends

In order to make them compatible as phases in a blend and to obtain desired properties, blends of immiscible polymers and, in particular, PP + PA blends, are developed by the addition of modifiers (compatibilizers) such as elastomers.

The functionalized polymers copolymerize in the blend by crosslinking on PA, giving rise to strong bonds between the two phases. The immiscibility of PP + PA6 blends leads to a reduction of the deformation at failure [Palacios, 2016] and this has been reported by other authors [Gonzales-Montiel, 1995]. This behavior can be explained by a process of delamination, detachment of the phases from the cooling phase and then on request, due to the reduced interfacial adhesion between the constituents.

The PPm material has the breaking surface typical of a thermoplastic polymer. It is observed that at low test speed, the breaking surface shows more pronounced local flows (the wavy surface on the right), indicating areas with qualitative differences of the polymer (degree of crystallinity and average molecular weight). At higher speeds, cavities generated by the uniaxial stress appeared, highlighting differentiated flows of the polymer. At the highest speed, these stress cavities are rarer and smaller, the breaking surface having a brittle appearance.

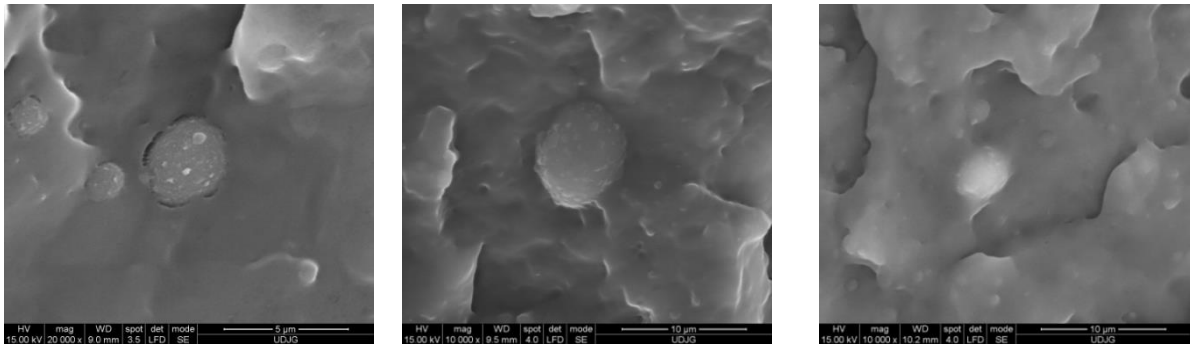

a) v=10 mm/min b) v=500 mm/min c) v=1000 mm/min

Fig. 4.21. Details of tensile fracture surfaces for material G at different test speeds

Figure. 4.21 shows details of tensile fracture surfaces for material G, which has a particular structure in the failure section.

For material G, the micromorphology of the breaking surface does not differ so much depending on the test speed. The PA6+EPDM matrix is observed, in which PP droplets are fixed. On the breaking surface, many drops are below 10 microns and remain trapped by the matrix through the fibrils. The PA6+EPDM matrix tends to deform in bundles, generating fibrils between them.

The influence of the compatibilizer concentration on the morphology of blends with PP+PA6+elastomeric compatibilizer was highlighted by Li and Xie [Li, Xie, 2017] on blends (PP+PP-g-(MAH-coSt))+PA6+SEBS (70+15+15), in which the component (PP+PP-g-(MAH-co St)) had concentrations of PP-g-(MAH-coSt) from 0% to 70%.

direction of increase of PP-g- content (MAH-co-St)

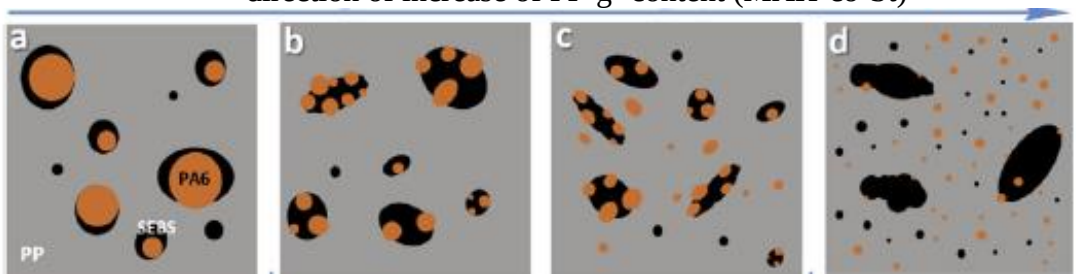

Fig. 4.22. Morphological model of a similar blend PP + PA6 + SEBS: a) complete wetting, b) and c) partial wetting, d) separate dispersion [Li, Xie, 2017]

In the case of using EPDM as a compatibilizing agent in PP + PA, or only in PA, the models discussed in Bai et a. [Bai, 2004] are customized in Fig. 4.22, depending on the test speed and the composition of the blend.

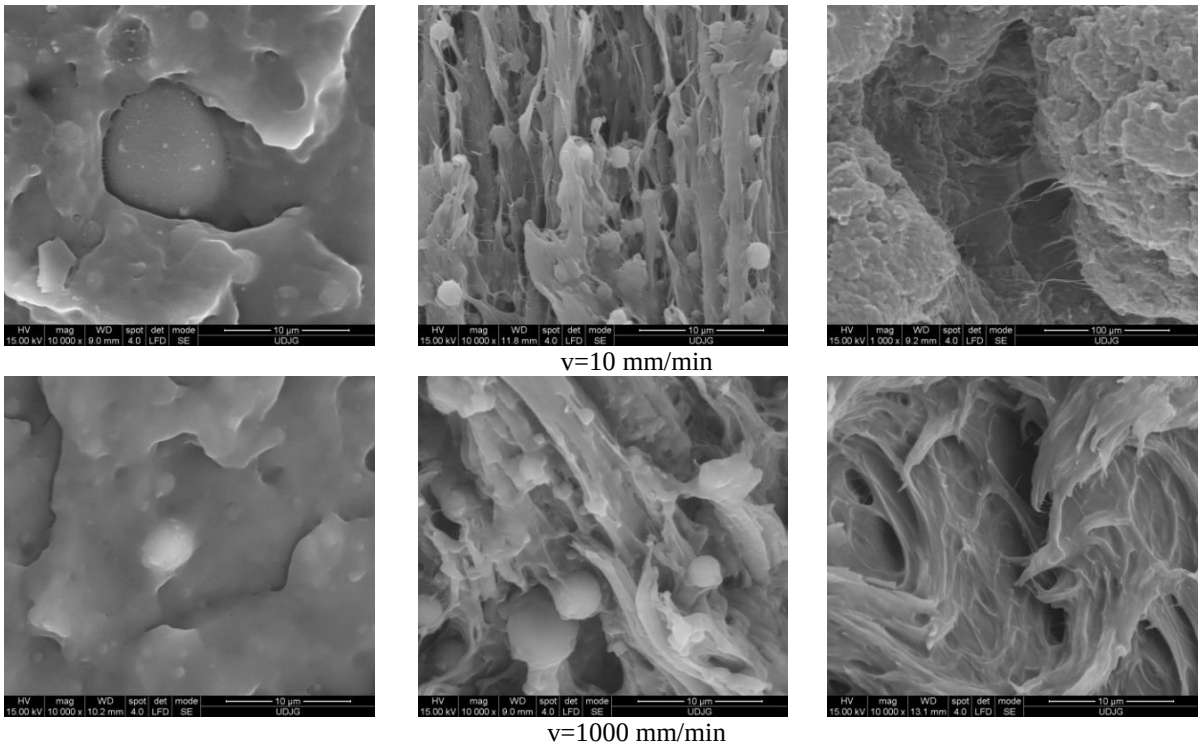

v=10 mm/min

v=1000 mm/min

H **G** **PA6m**

Fig. 4.23. SEM images only for blends from the second family at extreme test speeds

Although materials H and G have the same constituents, the structure in the tensile strength differs. Although H contains a small amount of EPDM (8% wt), it is observed that the PP + EPDM matrix has a better adhesion to PA6 droplets. No EPDM coatings were observed on PA6 particles. For blend G, the dispersed phase is PP and the droplet size is quite uniform. The failure occurs in the volume of the matrix by elongation. The PA6m material is a relatively homogeneous blend of constituents, with high local flows, which are the cause of a higher energy at break for breaking the specimen.

The identification of the constituents was performed by EDX analysis (Fig. 4.24). The droplets or islands could be identified as having PA6 whether or not there was a concentration of N (specific for polyamide) (specific for PP and EPDM).

Among the tested blends it is observed that material H has the lowest values of energy at break, resulting in this blend is not recommended for applications where energy at break is an important factor. If the values of the energy at break for v=10 mm/min are ignored, because real destruction mechanisms at these speeds are not often encountered and accepted

in machine components, the other values are grouped in the following ascending order for all speeds 250...1000 mm/min: H, PPm, PA6, G and PA6m. In other words, materials G and H, developed by the author, have promising results as impact-resistant materials.

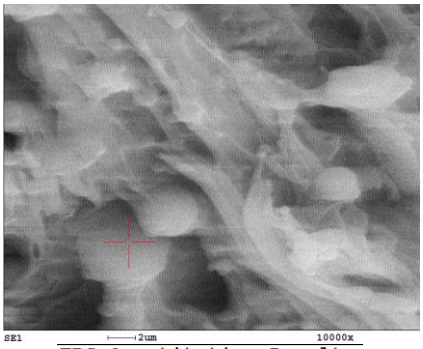

EDS Quantitative Results

Element	Wt%	At%
CK	89.27	91.73
NK	0.00	0.00
OK	10.73	8.27

a) presence of PP

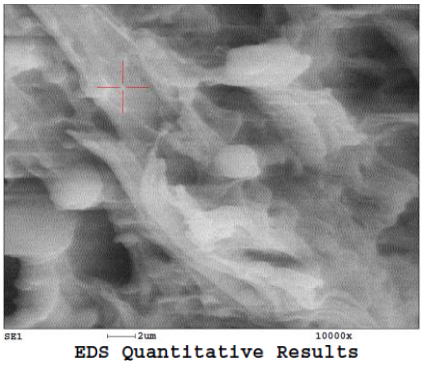

EDS Quantitative Results

Element	Wt%	At%
CK	78.90	82.53
NK	8.05	7.22
OK	13.05	10.25

b) presence of PA6

4.24. Identification of constituents by EDX (for material G)

Material G, has values higher than the blend H by ~10-15%, but the blend with the highest amount of PA6, PA6m, has the highest values of energy at break, even than that of simple PA6. For example, at v=250 mm/min, PA6 has 29.66 J, while PA6m has 76.3 J. In percentage, material PA6m has the energy at break 257.24% of the breaking energy of simple polyamide 6, which recommends it for applications that need low energy absorption. For the other test speeds, the proportion is kept, namely: at v=1000 mm/min, PA6m has 56.45 J, as compared to 24.05 J for PA6 (simple polymer), which represents 234.7% of the energy value at break for simple polyamide. Higher values than PA6 were also obtained for blend G, but the increase is not so significant.

4.8. Conclusions for All Tested Materials

The results of the tensile tests revealed the following:

- for all developed materials there were characteristics that were not very sensitive to the test speed (modulus of elasticity for some materials, stensile stress at break) and characteristics dependent on the test speed (energy at break and strain at break).

The characteristics of the first family are:

- the increase in the polyamide content produced, in some specimens (for materials C, D and PA6), processing cavities, which means that the production process should be improved,
- the morphology of the blends was dependent on the PA6 concentration, the phases being reversed from material B to material C,
- $CaCO_3$ dispersion is uneven (particle agglomerations were observed on SEM images),
- their grouping can be done (A and B) and (C and D).

Materials A and B have small tensile deformations, much lower tensile energies and PP matrices with dispersed droplets, of variable size of PA6

Materials C and D have higher tensile deformations, higher fracture energies, but not as much as each constituent and PP matrix with dispersed droplets, of variable size of PA6.

The characteristics of the second family blends are:

- the addition of kritilene in PP resulted in a very ductile character, with very high energy at break, at v=10 mm/min, but with the increase of the test speed the energy at break values decreased very much reaching values close to the polymer simple,
- materials H, G and PA6m had different morphologies, for the latter material, the blend of PA6 + EPDM being homogeneous and monophasic, and H and G being biphasic blends; material H has the behavior of a fragile material and G and PA6 are ductile materials.

Chapter 5
Characterization of Formulated Polymeric Blends by Charpy Tests

5.1. Impact Testing of Polymeric Blends Specimens

As with metals, plastics may behave differently depending on temperature and could exhibit a change in impact properties, from ductile to brittle, which must be known and evaluated when the polymeric material is introduced into an assembly [Arnold, 2015].
Even after 100 years, Charpy's impact testing procedures take place after similar procedures.

The tests in this paper were performed after consulting the following standards:

SR EN ISO 179-1: 2010 Plastics. Determination of Charpy shock characteristics. Part 1: Non-instrumental shock test,

SR EN ISO 179-2: 2020 Plastics. Determination of Charpy shock properties. Part 2: Instrumental shock test.

At the end of the testing campaign for this paper, the 2002 version was in force.

5.2. Charpy Test

5.2.1. Energy at Break for Charpy Test

In energy at break for Charpy test, there are contributions from various physical processes, such as the tip of the crack, the initiation of ductile cracks and, mainly, the propagation of cracks by breaking, the formation of the shear edge and the plastic deformation of the material. Ductile fracture is defined as failure that occurs with appreciable plastic deformation and considerable energy consumption. The main difference between ductile and brittle fracture is that, while the propagation of a ductile fissure is accompanied by a large plastic yield, very small plastic deformations occur at brittle fracture. The force-displacement diagram of a quasi-static bending test on a notched sample is given in Fig. 5.1.

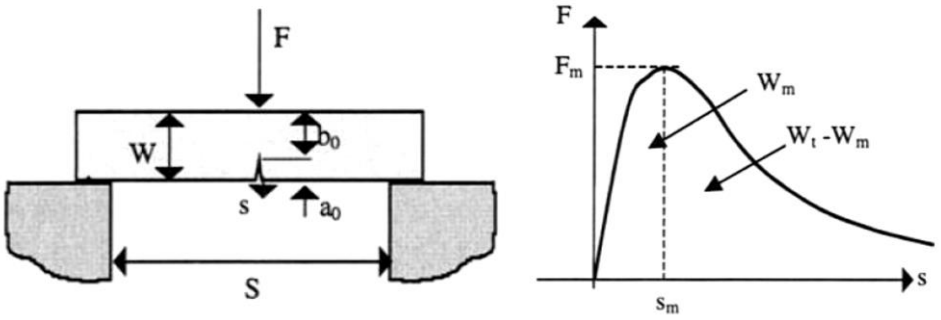

a) b)

Fig. 5.1. Mechanical tester (a) and the corresponding force - displacement diagram for a bending tests, with a notched speciman

A well-known evaluation procedure for this purpose is the bending force-deformation curve method. However, for a bending impact test, where the force-displacement diagram is generally influenced by significant oscillations (Fig. 5.1), the accuracy of this method is limited in the initial phase of crack appearance. In the case of a non-instrumented impact test, such as the classic Charpy test, the only determinable experimental parameter is the total energy at break, W_t. In fact, there is no direct physical relationship between Charpy energy at break and strentgth at break. However, the derived analytical equations and the good agreement with the experimental data imply that there are still some physical relationships between the two parameters. The main aspects seem to be the following: in small specimens,

such as Charpy specimens, deep failure of the crack is generally initiated, not before the plastic flow of the material.

The initial breaking strength depends on the radius of the notch. The energy consumed until the crack starts is very small compared to the energy required for the ductile fracture and plastic bending of the specimen. Therefore, the energy at break and the energy up to the maximum load are not much affected by the accuracy of the notches or cracks. As the energy at break decreases with decreasing temperature, the notch effect increases.

5.2.2. Charpy Test Procedure and Specimens

The Charpy test is standardized by the ISO 179-1 standard [EN SR ISO 179-1, 2010]: Determination of impact properties by the Charpy method. Impact test without instrumentation. The purpose of this standard is to specify a method for determining the Charpy impact resistance of plastics under defined conditions. A number of different samples and test configurations are defined. Various test parameters are specified according to the material type, sample test type and notch type. Charpy impact resistance with the notched specimen is characterized by a_{cN} - the impact energy absorbed at the failure of the notched sample, referring to the area of the original cross section of the notched sample, where N = A, B or C, depending on the type of notch [kJ/m^2].

The principle of testing. The specimen, held close to its ends like a horizontal bar, is struck once by the striker, with the line of impact in the middle of the distance between the supports and inclined at a high, constant nominal speed. The specimen supported on the supports, near the ends, like a horizontal beam, is impacted perpendicularly, with the line of impact between the supports, and bent at a high speed. The impact force is recorded. Depending on the method of evaluation, the deformation of the specimen may be measured directly by suitable measuring devices or in the case of energy carriers giving an impact without friction, calculated from the initial speed and force as a function of time. The force-deformation diagram obtained after the tests describes the behavior of the specimen on impact depending on the high bending speed, from where some aspects of the material properties can be deduced.

5.2.3. Test Equipment and Measuring System

The tests in this paper were performed on the CEAST 9340 impact test machine within the materials strength laboratory at the Polytechnic University of Bucharest. Unlike pendulum equipment, it uses a pneumatic cylinder to print the desired speed to the striker, which has a rectilinear motion, the space required being better managed than in the case of pendulum systems.

The CEAST 9340 equipment is equipped with an anti-recoil system, a temperature-controlled work enclosure, a height adjustment system from which the striker starts to vary the impact energy. The characteristics of the machine are: Energy range 0.30...405 J, impact speed 0.77...4.65 m/s, fall height 0.03....1.10 m/s and mass impactor 1...37.5 kg.

According to the SR ISO 179 standard, ten tests were chosen for each material considered to be typical for the respective material (were eliminated the tests that gave results far from the typical values).

The basic components of the test machine are the impactor, the striker and the frame with test tube supports. The load carrier may be of the inertial type (eg free-falling pendulum or lance, which may be spring-loaded, pneumatically or hydraulically operated. The force exerted on the specimen must be measurable, and its deformations in the direction of impact must also be measurable or derivable.

For the types of pendulum with low energy, the impact speed v_0 is 2.9 ± 0.15 m/s and for those with high energy 3.8 ± 0.2m/s. [SR EN ISO 179-1, 2010].

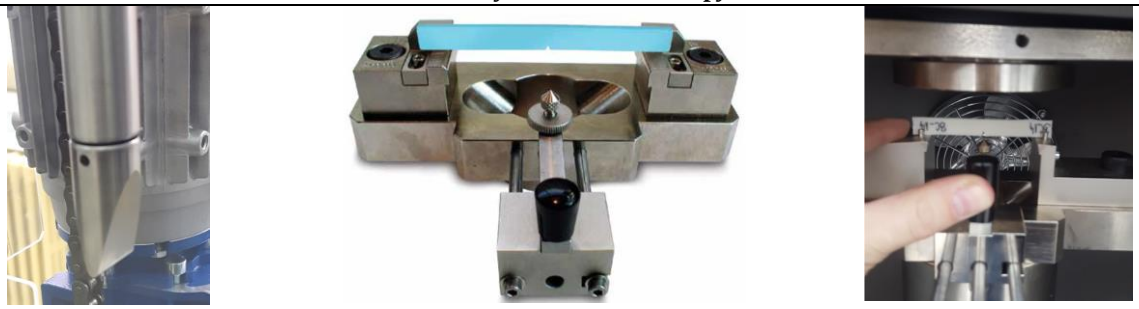

a) impactor b) specimen on support c) position adjustment

Fig. 5.2. The CEAST 9340 equipment used for the tests in this paper

The tests were performed with a hemispherical impactor, with a speed of 0.96 m/s and the mass of the impactor 3.219 kg. Figure 5.2 shows how to support the specimen and check the position of the notch in the middle of the distance between the supports.

5.3. Experimental Results

5.3.1. Results Obtained for the First Family of Polymeric Blends

Factors influencing impact resistance include impact speed notch shape and dimensions [Berstad, 1994], [Pick, 2008] semicrystalline polymers, such as polyolefins, including PP, increasing the degree of crystallinity decreases the impact resistance and increases the probability of brittle fracture, resulting in the impact resistance is also dependent on the thermal history of the part. In general, a faster melted material will be more impact resistant than if it is cooled slowly [Brown, 2002]. For polymer blends the impact behavior is also influenced by the nature and concentration of the constituents.

In this paper, specimens with dimensions of 10 mm x 4 mm x 80 mm and notch type C were used (Fig. 5.3).

Of all the features given by the test machine software, after the Charpy impact tests, the author highlighted the graphs with the characteristics of maximum Charpy impact force and energy at break, graphs that were done for each material.

The specimen has the drawing shown in Fig. 5.3, and Fig. 5.4 shows the geometry of the impactor.

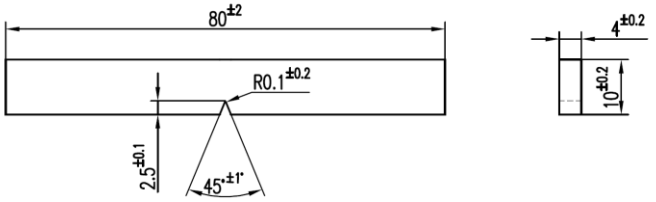

Fig. 5.3. Specimen dimensions

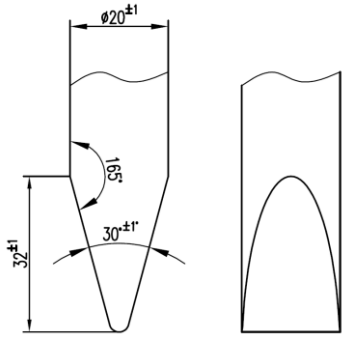

Fig. 5.4. Impactor geometry

For PP, the force-time curve has an evolution with wide oscillations, on an upward trend (Fig. 5.4). The energy absorbed by the specimen is calculated to the lowest value of force F, before 0, and will here in after be called the total Charpy impact energy or energy at break. It is considered that the value of the energy absorbed between the last positive value of F and F=0 can be neglected because it is of the order of 10^{-5}...10^{-6} J.

The moment of cancellation of the impact force for eight specimens was concentrated in the time interval of $0.89x10^{-3}$ s to $1.1x10^{-3}$s, and for the other two specimens the moment for F=0, appeared much later, and namely for specimen 2 at $1.37x10^{-3}$ s and for specimen eleven at $1.43x10^{-3}$ s.

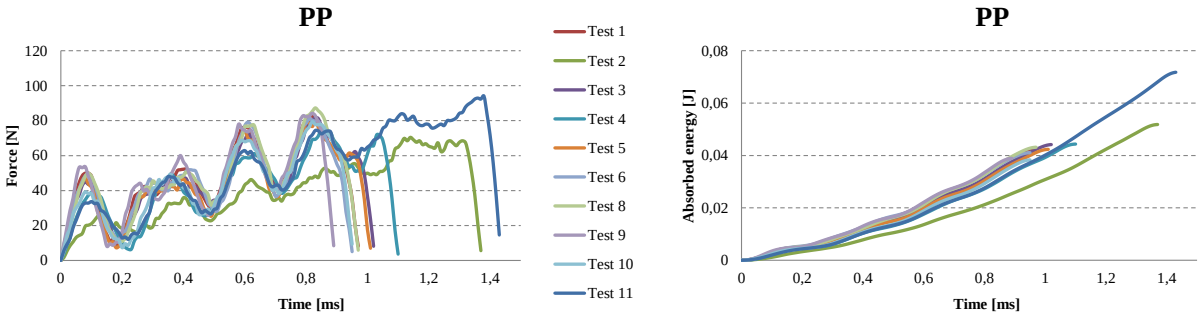

Fig. 5.5. Diagram of force and absorbed energy at impact, for material PP

Regarding the graph of absorbed energy over time, the trend of evolution of the curves is similar to that presented for the material PA6. In the evaluation of the energy at break, the values of the energy absorbed by the specimen up to F=0 were considered.

In [***Polypropylene (PP) Typical Properties Generic PP Impact Copolymer, https://plastics.ulprospector.com/generics/39/c/t/polypropylene-pp-properties-processing/sp/26], are given data for typical PP, 2.52...50.4 kJ/m^2 at 23 °C, and in [***Polypropylene(PP),http://www.irpcmarket.com/upload/document/datasheet-1516693272.pdf] the value of Charpy impact resistance is 6.5 kJ/m^2. If the impact strength of the specimen with the formula is calculated

$$R_{impact} = \frac{\Delta E}{A_0}\left[J/m^2\right] \tag{5.1}$$

where ΔE is the energy absorbed up to F=0 and $A_0 = b(h_{specimen} - h_{notch})$, for PP is obtained $R_{impact(PP)} = 1.267....2.333\,kJ/m^2$. This value depends on the initial test conditions, with reference to the initial speed and mass of the impactor and the shape and dimensions of the notch. The values can only be compared for the same initial conditions and the same notch.

The graphs of velocity as a function of time are well grouped even in the form of small oscillations, which reflects the homogeneity of the material. The tendency to decrease the speed is of parabolic type, characteristic of the visco-plastic materials.

One of the tests considered was done with v_0=0.96 m/s, the others being performed at v_0=0.950 m/s. The test was considered valid because the speed variation was only 1.052% of the speed value for the other nine tests (v_0=0.950 m/s).

The oscillations of the force in time are more pronounced than in PP and three oscillations can be observed, the first of which is very well outlined for all specimens, which reflects that the mechanism of failure in this area of the graph is similar for all specimens. The oscillation of the force in the middle of the graph is more uneven reflecting the non-uniformity in section of the processing gaps and/or of the local blend between the polymers. The graph is followed by a third oscillation of the force with different maximum values. The existence of small peaks after this higher oscillation reflecting the failure of some fibrils left after the previous failure process (the last maximum of the force).

Material A (Fig. 5.6) presents the following characteristics of the force-time curve. The first peak of the force appears around the moment t=$0.07x10^{-3}$ s and the first minimum of the force appears at t=$0.18x10^{-3}$s, after which the specimens have a slightly ascending plateau followed by a final increasing zone only for two specimens, at approximately t=$0.47x10^{-3}$ s.

For the other eight specimens a last maximum of the force was obtained around t=0.62x10^{-3} s. For this material the force reached zero in the interval t=0.45...0.84x10^{-3} s. In other words, material A shows three distinct areas on the force-time graph:

- zone I - a curve with a maximum force of 42-55 N and a descent to a time of t=0.18x10^{-3} s for all the specimens tested;

- zone II comprises a sudden rise, a slightly ascending bearing and an oscillation with a maximum between 50...82 N; this level differs greatly in duration and shape;

- zone III represents the last oscillation of the force, the maximum being between 62...95N, after which the graph drops to 0.

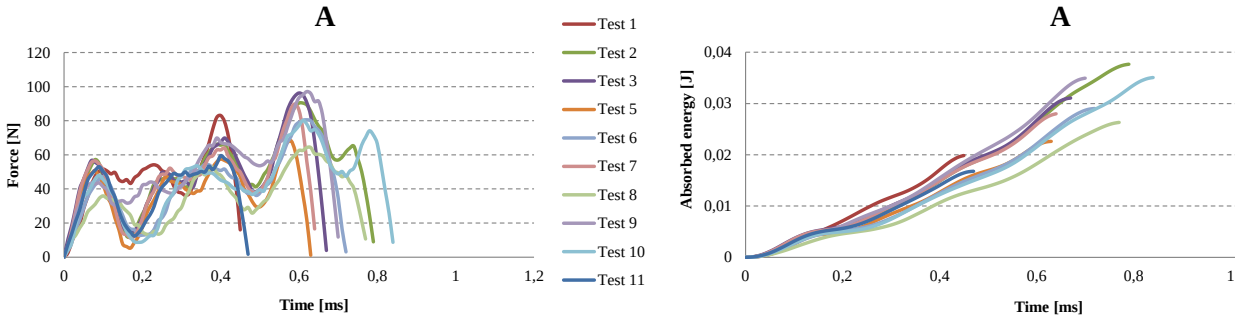

Fig. 5.6. Material A

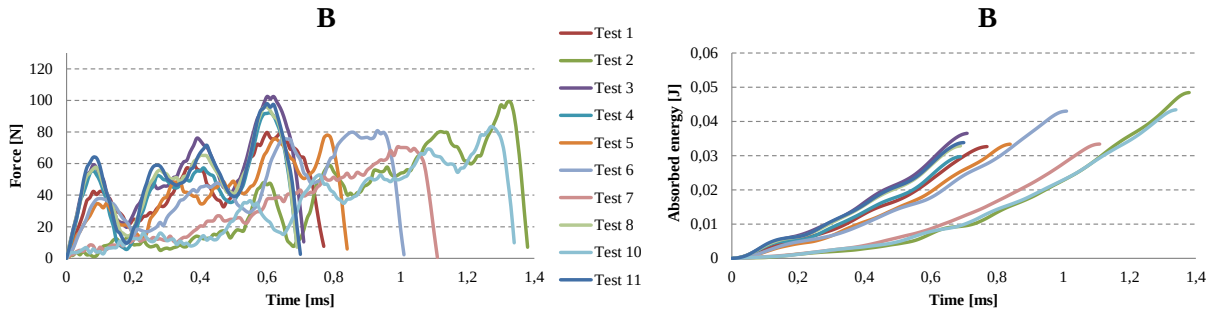

Fig. 5.7. Material B

If the first stage is similar for all specimens, this does not happen in the other areas, the latter differ especially in duration. Through the oscillations of the force, the material A shows that it is a blend and that there are areas in it that are more opposed to breaking (areas predominant with PA6) and therefore more irregular levels appear compared to PP. The energy at break (up to F=0) evolves almost linearly for all specimens, with very small ripples but the scattering of the total energy at break values is over a large range (0.677 J). For material A the impact resistance varies between $R_{impact(A)} = 0.600....1267\ kJ/m^2$.

Material B has similar curves (Fig. 5.7), but all breaks, unlike material A, occur after t=0.7x10^{-3}s. The force value range that includes the tests performed for material B is wider, namely 40 N for the first stage, 50 N for the second stage and 60 N for the last stage.

Regarding the energy-time curve, the tested specimens were grouped seven on an almost linear curve, but with a smaller slope and three on a curve consisting of two areas, a linear one with a smaller slope, followed by a slightly parabolic one. The force-time curve of the material shows oscillations with shorter periods and more than at A and B. The first stage is similar to the other two materials discussed above, but the second stage has different oscillations, the curves do not overlap for all specimens. The breaking time (F=0) varies from 1.06x10^{-3} s to 1.63x10^{-3} s. The range of impact resistance variation for material B is 0.667 J and the impact strength value is $R_{impact(B)} = 1.00....1.667\ kJ/m^2$

Material C (Fig. 5.8) has energy-time curves with smaller oscillations, but the trend is almost linear, and the scattering range of the results for energy at break is 0.057 J. The value of impact resistance is $R_{impact(C)} = 2.4...4.3\,kJ/m^2$

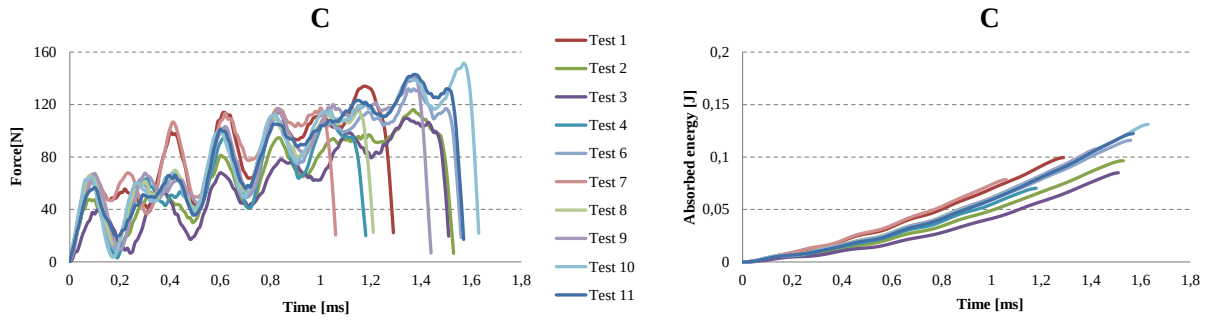

Fig. 5.8. Material C

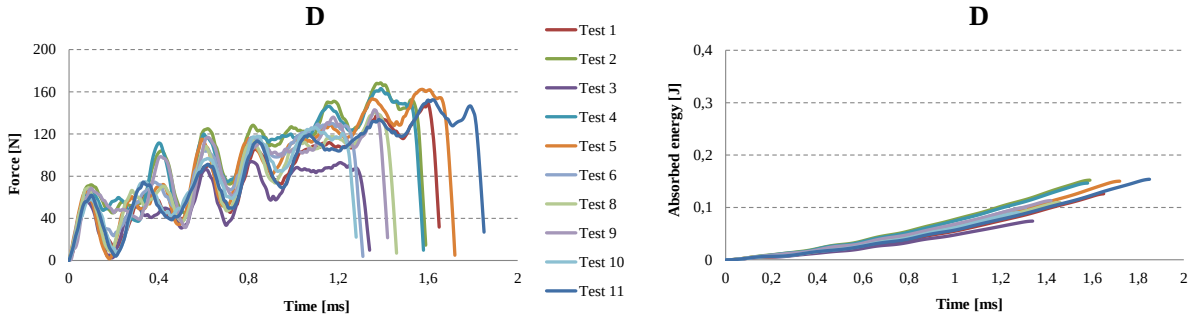

Fig. 5.9. Material D

Material D (Fig. 5.9) has a similar evolution to material C, for all curves analyzed over time (force, absorbed energy). The shape of the energy-absorbed-time curve is parabolic and with a smaller radius of curvature, and the variation range of this characteristic is 0.08 J.

$R_{impact(D)} = 2.467...5.133\,kJ/m^2$

The values of the force-time curve for PA6 fall for all tests in an ascending band of width about 50 N. Within this band, the tests oscillate with different time periods, shorter at the beginning of the impact and then with longer time periods and oscillations. more mitigating. The tests showed the failure of the specimens in the range between $t=2.08x10^{-3}$ s and $t=2.59x10^{-3}$ s. In contrast, the absorbed energy, calculated as the area of the surface under the force-time curve, has a uniform evolution in a relatively small interval; the variation of the absorbed energy for the tested specimens being from 0.21 J to 0.28 J. The energy curve in time has two components, an almost linear area, between $0...1x10^{-3}$s and then a curved area until breaking. The impact resistance of PA6 was $R_{impact(PA6)} = 7.0...9.3\,kJ/m^2$.

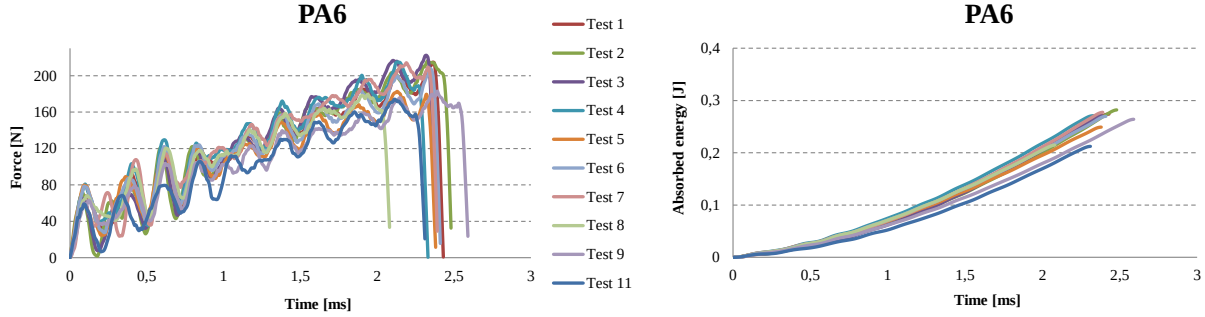

Fig. 5.10. Material PA6

5.3.2. Results Obtained for the Second Family of Polymeric Blends

Figure 5.11 shows macro images of the broken specimens and how the specimen fragments were prepared for SEM investigations. The clarity of the images was obtained by covering the surfaces of interest with gold. Charpy test behavior will be discussed in order of increasing PA6 concentration.

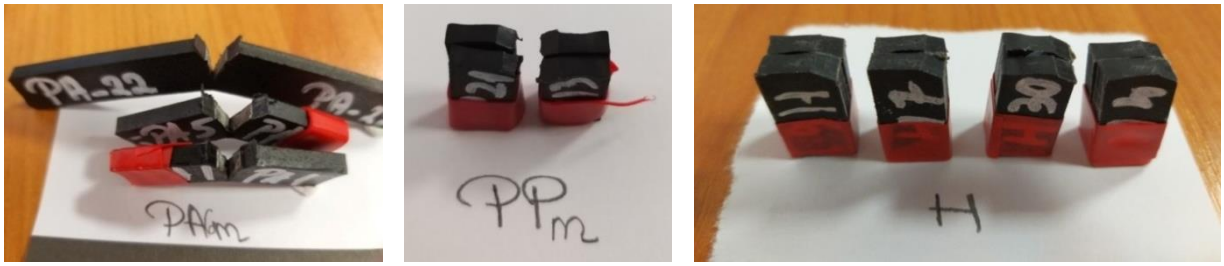

Fig. 5.11. Specimens after Charpy impact testing

Material PPm

The force-time curves have large oscillations especially in the first part of the destruction process, the oscillations being of 30-60 N which means a mixed structure of amorphous and crystalline volumes.

The breaking time for the most of the specimens is up to $1x10^{-3}$s except for test eleven, for which the specimen broke at $t=0.9x10^{-3}$ s. Regarding the energy-time zones, two zones can be distinguished: the first up to 0.07 J which has a very large curvature followed by a linear zone except for test eleven, the rest of the results fall in a very narrow band of 0.025 J The very short time to failure shows the more fragile nature of PP.

The addition of Kritilen in PP does not introduce noticeable changes in the form of force-time curves, but in the case of PPm several specimens "crowd" with breaking to higher values of moments for F=0.

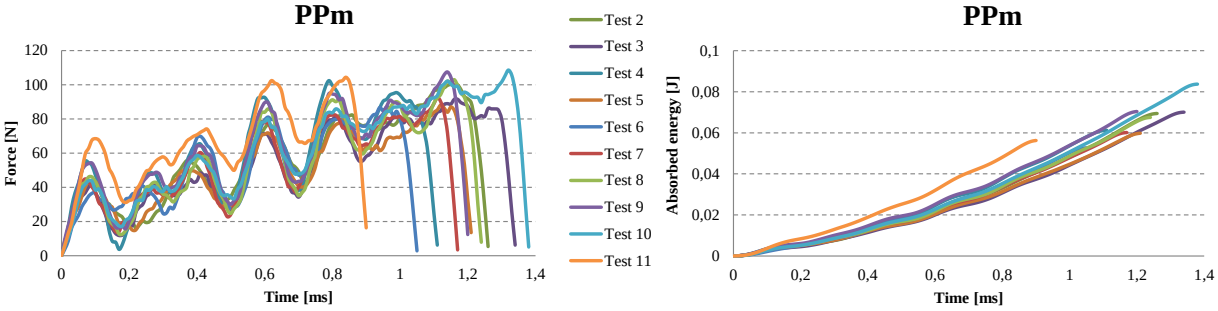

Fig. 5.12. Material PPm

If we compare the values of some parameters from the Charpy test for PP and PPm, it is observed that PPm has slightly higher values, both for F_{max} and for the energy absorbed on impact (Table 5.2). The time to failure (F=0) is approximately the same for PP and PPm (0.85...1.4 ms). It turns out that the addition of this agent Kritilen PP940 has improved the behavior of PP on impact, even if its concentration is only 1%. From the tests performed, the impact resistance for PPm was $R_{impact(PPm)} = 1.7...2.8\,kJ/m^2$

The behavior of the H material in the Charpy test is similar to that of the PPm material (Fig. 5.13), but the time to failure (considered at F=0) is close, the specimens having the time to failure from $0.9x10^{-3}$ s to $1.29x10^{-3}$ s. The oscillations of the force-time curve show the presence of two polymeric structures, one more tenacious and the other weaker. The oscillations of the force-time curve show that in the breaking section the material is

composed of an alternating succession of more resistant micro-volumes and weaker materials from a mechanical point of view, but also amorphous and crystalline micro-volumes of the two constituent polymers (PP and PA6). The impact resistance value for material H, $R_{impact(H)} = 1.5...2.733\,kJ/m^2$, does not recommend it for impact resistance applications.

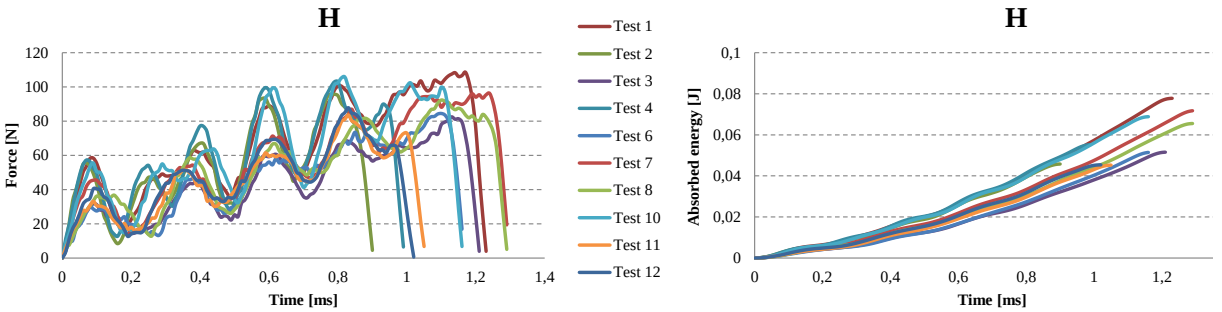

Fig. 5.13. Material H

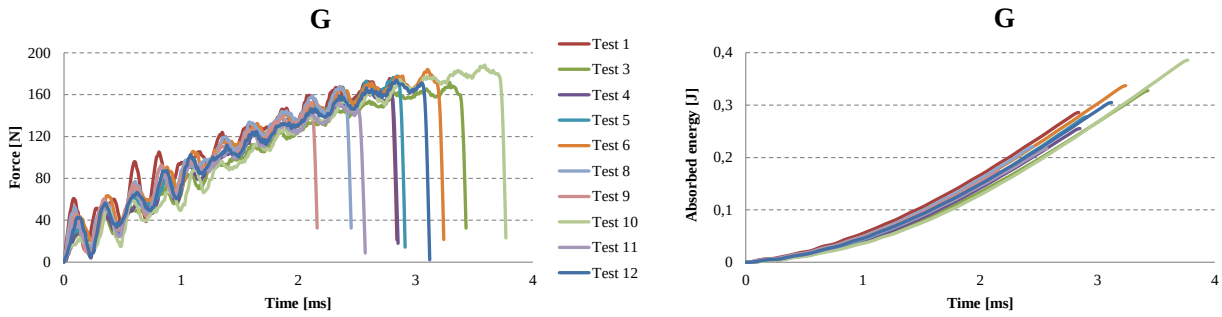

Fig. 5.14. Material G

Material G (Fig. 5.14) has a much smaller amplitude of force oscillations. The oscillations start with values between 30-60 N, after which the amplitude of the oscillations does not exceed ~ 20 N. The maximum values of the force are concentrated between 150-180 N, which reflects that the specimens are more similar in terms of response to the request, that is, the quality of the injection process is more controllable for this material. The energy-time curves are very close and very similar. The scattering band of the curves is narrower up to 0.5 J (up to 1 ms) and then on the linear area it is slightly more scattered.

The value of the moment of completed failure (F = 0) is in the range of $t=2.16x10^{-3}$s to $t=3.77x10^{-3}$s. If G is compared with the other materials (Table 5.2), it is observed that the maximum value of time to failure has the value of $t=3.77x10^{-3}$ s, the highest of all materials of the second family. If the materials are ordered in descending order of the greatest value of time to failure (F=0), this is G, PA6m, PA6, PP and very close to each other, PPm and H. For F_{max} the highest value is for PA6, followed by that for PA6m.

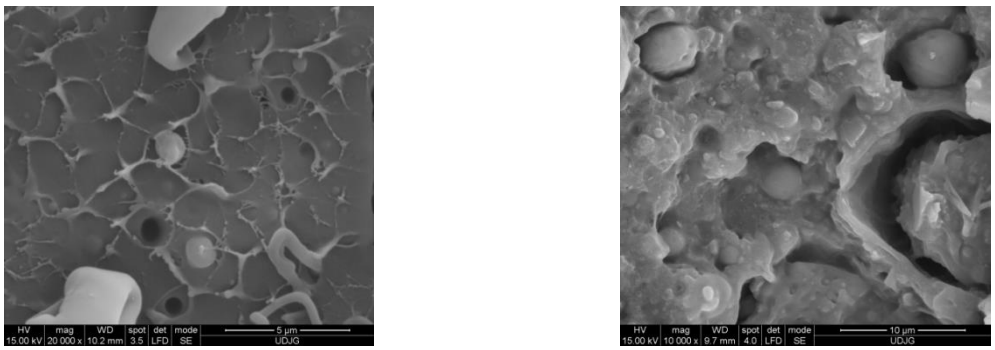

a) Material H b) Material G

Fig. 5.15. Fracture morfology at break, after the impact test

The SEM images (Fig. 5.15) shows that the introduction of PA6 in higher concentration altered the morphology of the blend. Material H has a PP matrix with PA6 droplets and pores of the order of a few microns.

The droplets located right on the breaking zone are very deformed, elongated and the matrix breaks as a more brittle polymer, with linear micro-flows, probably as a result of a lower crystallinity of PP. Material G has the inverted phases, as it resulted from the EDX analysis. The PP droplets are larger and do not have cohesion on the whole surface with the matrix, which seems to be a homogeneous blend of PA6 and EPDM. But the most important feature, the energy absorbed during impact, has the highest value for PA6m (0.305...0.389 J). Impact resistance values are in the range $R_{impact(G)} = 5.767...12.733\,kJ/m^2$

The addition of EPDM in PA6m has a force-time diagram similar to that of simple polyamide, but the failure occurs after a slightly longer time interval. At t = $2.59x10^{-3}$s, for PA6, all the specimens were already broken, whereas for PA6m the damage of the specimens (with incomplete failure), is achieved between t=$3.34x10^{-3}$ s and t=$3.59x10^{-3}$ s. In other words, the addition of EPDM increases the time to failure (even partially, in the case of PA6m material). The evolution over time of the destructive energy has similar forms only that most of the PA6m specimens break partially after storing an energy between 0.305 J and 0.389 J, while PA6 reaches only 0.279 J at the complete failure of the specimens.

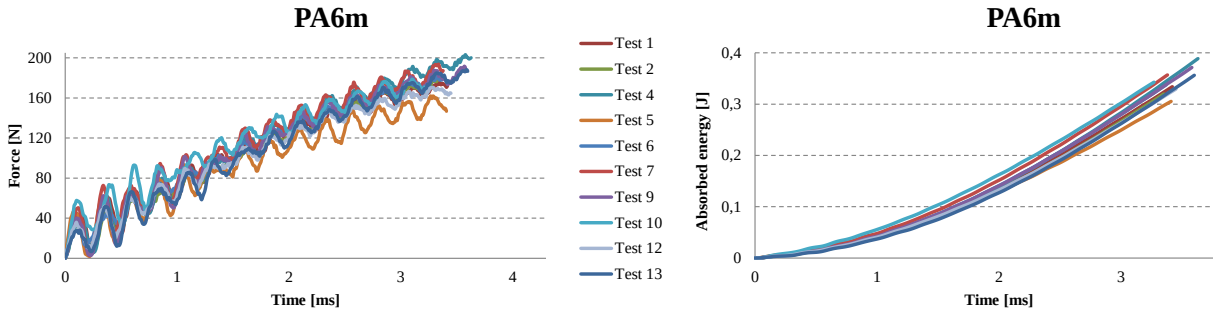

Fig. 5.16. Material PA6m

The energy at break graph for PA6m has two areas: one in which the energy increases after a curve up to 0.15 J, after which the evolution of the energy stored in the test tube is linear. Impact resistance values are in the range $R_{impact(PA6m)} = 10.16...12.96\,kJ/m^2$

5.4. Comparative Analysis of Results

The First Family of Blends

The diagram of the average values of the breaking force and the spreading interval reveals the following:

- the material that breaks and has the lowest maximum force value is PP,
- the material that breaks and has the highest maximum force value, is PA6
- blends A, B, C and D have intermediate values for the maximum force, between 81.6 N for PP and 201 N for PA6.

For blends A and B the maximum force is close to that of PP. Increasing the PA concentration leads to an increase in the maximum strength for blends C and D, but does not reach the value of polyamide.

Scattering intervals increase with increasing PA6 concentration, so the behavior of materials C and D is more difficult to predict. The large scattering for C and D can also be caused by the presence of cavities in the processing cavity inside the specimens.

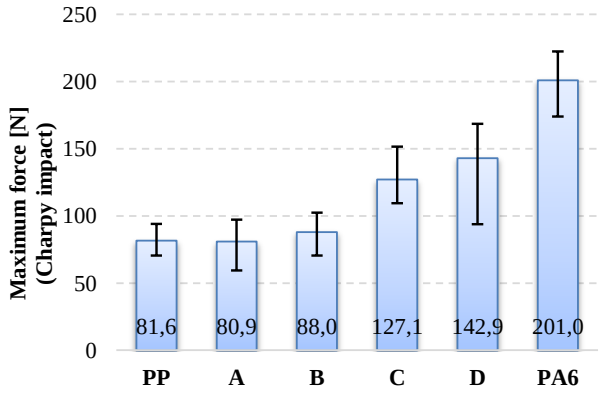

Fig. 5.17. Average values of maximum force for the first family of blends

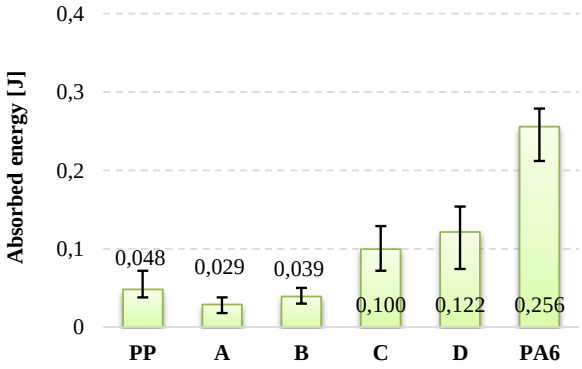

Fig. 5.18. Average values of absorbed energy at break for the first family of blends

The energy at break shows that the elaborated blends (A, B, C and D) can be grouped into two classes. A and B have the lowest average values, lower than those of PP by approximately 39.5...18.75%. The energy at break of material A is 39.5% lower than that of PP, and material B has a energy at break of 18.75% lower than that of PP. Materials C and D have a energy at break of about half the average value of PA6. The higher concentration of PA6 leads to the spread of values over wider intervals.

If the maximum force and energy at break are analyzed, the best material in terms of impact resistance in this family remains PA6, but with too long spreading intervals. The blends formulated by the author, C and D have better values for energy at break, but they will be recommended in applications, only if they have other criteria for which they compete with PA6.

The Second Family of Blends

Comparing the four materials (PPm, H, G and PA6m), the value of the maximum force was obtained for PA6m. The material for which the following maximum force value was obtained is G, with 170.7 N, only 6.46% lower than the PA6m material.

PPm has the maximum force about half of G, and for H the lowest value was obtained, in other words, H is the weakest material in terms of the maximum force required for damage.

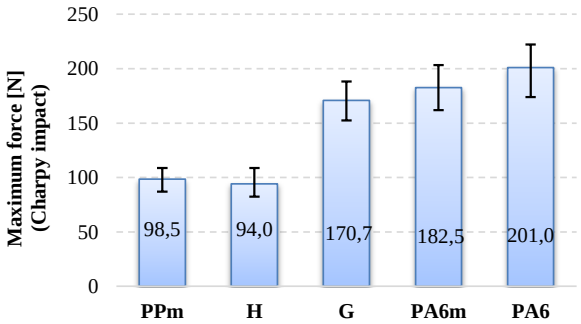

Fig. 5.19. Average values of the maximum impact force Charpy for the second family of blends

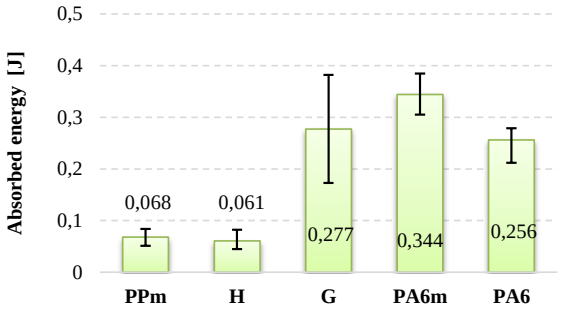

Fig. 5.20. Average values of the absorbed energy for the second family of blends

Regarding the energy at break (Fig. 5.20), it is observed that the best results were obtained for PA6m, both for the average value of the energy at break (0.344 J) and for the spreading interval, which is below 0.084 J.

PPm and H materials have about five times less energy at break than PA6m material. It is clear that in applications with shock resistance materials, PPm and H are not recommended, instead the PA6m (PA6 + EPDM) coat gave better results than for PA6.

Material G should not be removed from the recommendations for shock applications with speeds up to 1 m/s, but the scattering of the results is higher and the average value of the energy at break is very close to that of the simple polymer PA6. The choice between these two materials, G and PA6 is made by analyzing other criteria necessary for the design, such as water absorption, dimensional stability, processability and price.

Aspects of impact-breaking mechanisms at this low speed (0.97 m/s) are shown in the following figures using SEM images, of lower or higher magnification. The magnification of x50...x100 shows the character of the failure, ductile or fragile. From Fig.5.21 it is observed that PPm and H materials have a brittle fracture appearance, while G and PA6m materials have fracture surfaces typical of ductile fracture.

All tested PA6m samples showed the same form of failure while maintaining a link between the test tube fragments (without complete failure) (Fig. 5.22).

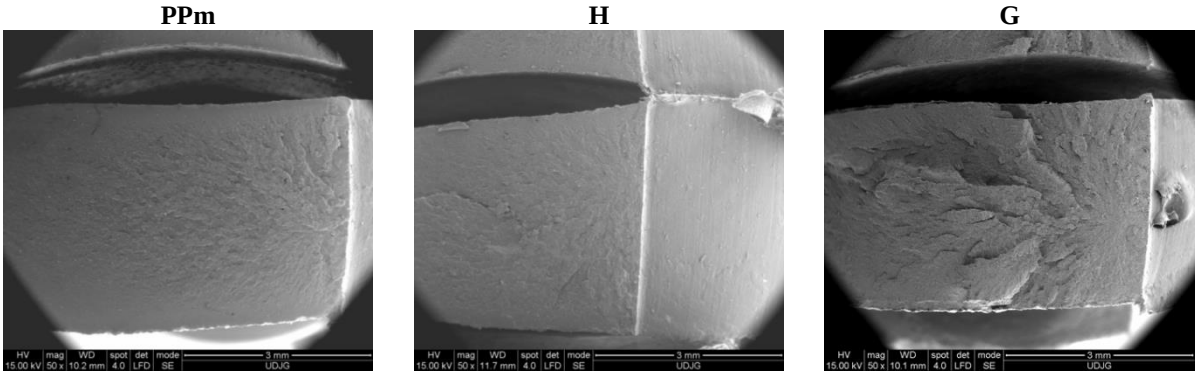

Fig. 5.21. The aspect of failure for the studied materials from the second family of blends

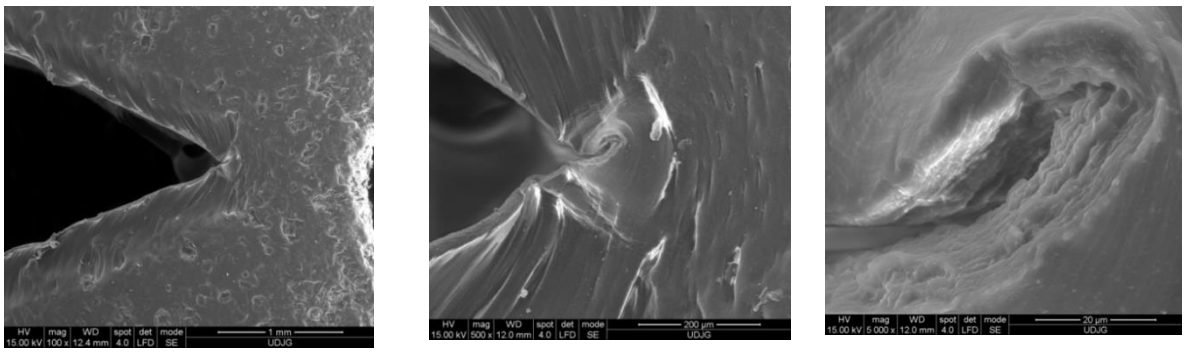

a) 1 mm b) 200 μm c) 20 μm

Fig. 5.22. Appearance of failure for the specimen of PA6m material (side view)

Studying these images, it is not possible to specify whether the failure advanced only from the notch or occurred in the impact area of the impactor. The aspects of breaking material H are similar to PPm. Material G has a different appearance from the materials discussed above (Fig. 5.21): the breaking surface is much rougher and it is likely that the tear was initiated first near the notch but then under the impactor. The very uneven area is very likely to have yielded more abruptly than the material under the notch and under the impactor, some dispersed droplets are partially detached from the matrix, but others, usually smaller, are trapped in the matrix.

The most interesting SEM images were obtained for PA6m (Fig. 5.22). An area parallel to the breaking surface of the crack is observed in which the material has a pronounced plastic yield at an angle of approximately 45° to the breaking surface. The thickness of this layer is about 200 microns and was not observed in the other materials that contained EPDM (H and G). Stopping the crack progress is observed in Figs. 5.22a and b.

The addition of EPDM to PA6 led to the propagation of a failure without fibrillation but with strong local flows on a band near the failure surface.

5.5. Conclusions from the Analysis of Experimental Data from Charpy Tests

In order to formulate some conclusions on the impact behavior of the elaborated materials, typical force and energy curves were superimposed for each material because in this way qualitative differences and similarities can be observed.

From Fig. 5.23 the following can be observed (PA6 material is represented on the graph of each family, for easier comparison):

- similarities: the oscillating aspect of the force in time characteristic of polymeric materials, the tendency of the average force almost linear

- difference: duration to failure: can be considered more fragile materials (PP, A, B and PPm and H) for which the time to failure considered at F=0 is relatively shorter; PA6, C, D, G and PA6m materials have a more ductile character, reflected by a longer time until breaking by Charpy test.

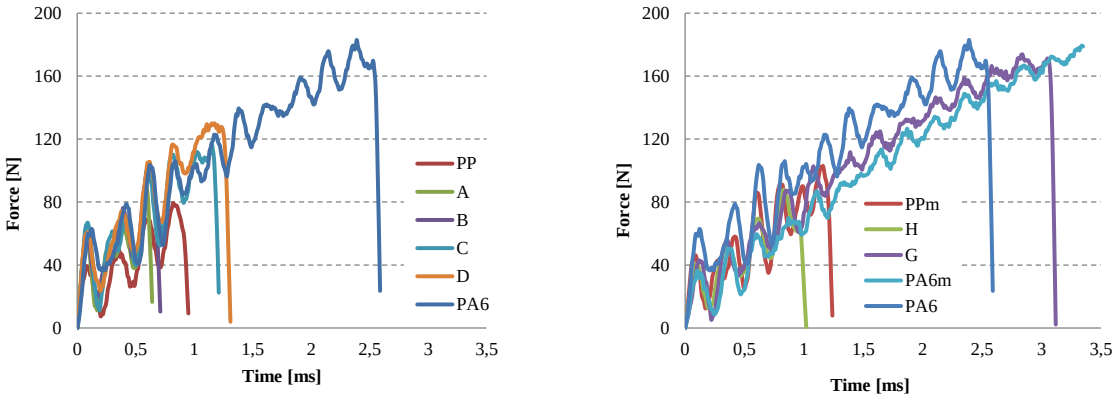

a) first family of blends b) second family of blends

Fig. 5.23. Typical force-time curves for each material tested

From Fig. 5.25, which shows the energy absorbed by the specimen (considered equal to the energy lost by the impactor) the following can be observed:

- similarities: appearance of curves: an almost linear area followed by a curved area resembling a parabola branch

- differences:

- energy at break value (considered at F=0): high values were recorded for PA6, G and PA6m and low values for PP and A; intermediate values were obtained for material D;

- materials from the first family, with the exception of PP, have very close curves even if they stop at different energy values, while for the second family, materials G, PA6m and PA6 have more distant curves.

Analyzing the graph of the evolution of the absorbed energy, it can be concluded that the materials with the best behavior in Charpy testing were PA6, PA6m and G, the last two having the highest values. Figures 5.24 and 5.25 show graphically the dependence of the two characteristics resulting from the Charpy test, depending on the PA6 concentration.

From the point of view of the absorbed energy (Fig. 5.25), a very different evolution is observed depending on the concentration of PA6 and the additions in the PP+PA6 blend.

The first family has a slightly increasing energy at break with the concentration of PA6, materials C and D having close values, but below the value obtained for PA6 (0.256 J).

For the second family, the addition of EPDM causes this characteristic to increase suddenly, from a concentration of 12% to a concentration of 40% PA6.

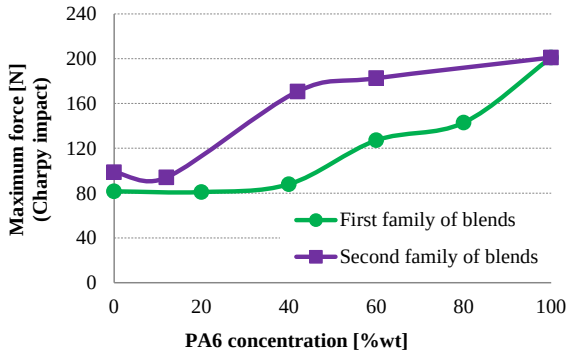

Fig. 5.24. Average values of the maximum impact force Charpy for the two families studied

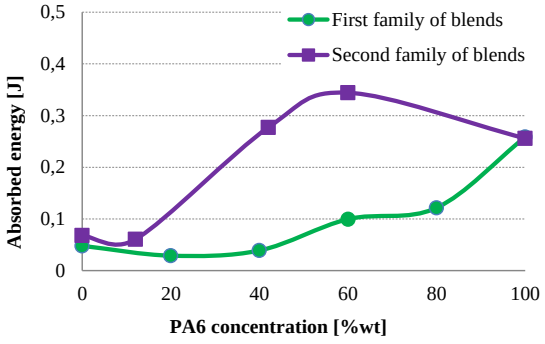

Fig. 5.25. Average values of the absorbed energy for the two studied families

The maximum energy at break value for this family was obtained for PA6m (0.344 J), which has only 60% PA6 and 40% EPDM. A good value was also obtained for material G (0.277 J).

Analyzing the results obtained for the two families of materials, the conclusions are as follows: the first family had satisfactory results for energy at break for material C and D, but at half the value of PA6, so the additions in the author's recipes did not substantially improve the impact characteristics, at least up to a speed of 1 m/s.

In addition, blends C and D tend to form cavities due to the immiscibility of the constituent polymers, PA6 and PP, and the modifying agents ($CaCO_3$ and Polybond 3200) do not eliminate processing problems (especially processing cavity) nor dramatically increase energy at break on Charpy testing.

For the second family, for materials G and PA6m, the results are very good, in the sense that PA6m exceeds PA6, and G also exceeds the energy at break on impact of polyamide.

For the first family, the maximum force increases slightly with the concentration of PA6, from the lowest value (PP and A), to PA6, which reaches 200.96 N.

Combining the two graphs, that of energy at break and that of maximum force during impact, the best materials in terms of impact resistance up to a speed of ~1 m/s are G, PA6 and PA6m (in ascending order of average energy at break). Numerical values for this ordering of the quality of the elaborated materials are given in Tables 5.1 and 5.2.

Table 5.1. Characteristics obtained from Charpy tests, for the first family of blends

Characteristic	PP	A	B	C	D	PA6
Absorbed energy at break [J]	0.048	0.029	0.039	0.09	0.12	0.256
Maximum force [N]	81.61	80.94	87.96	127.14	142.91	200.96
Impact resistance [kJ/m^2]	1.603	0.96	1.29	3.32	4.05	8.52

Table 5.2. Characteristics obtained from Charpy tests, for the second family of blends

Characteristic	PP	PPm	H	G	PA6m	PA6
Absorbed energy at break [J]	0.048	0.068	0.061	0.277	**0.334**	0.256
Maximum force [N]	81.61	98.54	94.05	170.70	**182.52**	200.96
Impact resistance [kJ/m^2]	1.603	2.26	2.017	9.23	**11.47**	8.52

Chapter 6
Modeling and Simulation of the Behavior of Polymeric Specimens in Charpy Test

6.1. Material Modeling and Failure Criterion in Simulation

The tests provided complex data on the behavior of polymeric materials, with increasingly complex constitutive models, which take into account several factors (temperature, deformation rate, structure, stress).

The importance of modeling the behavior of the material, regardless of its nature, is emphasized by valuable works [Johnson, 1983], [Johnson, 1985], [Cowper, 1957], [Schwer, 2007]. Recent studies, experimental and obtained by simulation, have emphasized the importance of modeling the material at high deformation rate [Liu, 2018], [Pîrvu, 2019], [Yaich, 2020]. But most studies refer to metal alloys, used in high-end fields (aerospace, military). Equipment for testing materials at high deformation rates does not reproduce the conditions encountered in practice and the results obtained, although realistic, cannot be extrapolated to real applications without accepting a higher degree of risk than in the case of low deformation rates. Hence the usefulness of numerical simulations, along with experiments, because it presents an alternative to the study of destruction processes.

Gavrus and his collaborators from INSA Rennes, France, have published several studies emphasizing the importance of modeling the behavior of the material in a thermo-visco-plastic variant, proposing a mesoscopic model [Gavrus, 2009], [Gavrus, 2012], [Lee, 2019],[Okereke, 2020], [Jiang, 2020].

As the temperature increases, yielding may occur and its limits decreases with increasing temperature. On the other hand, the deformation at break, increases with increasing temperature, the polymer becoming a brittle material at low temperature, a ductile material at high temperature. The effect of the loading rate on the stress-strain curve is opposite to that caused by temperature. At low loading rates or long loading times, the polymer can behave ductile and have a more pronounced hardening. At high loading rates or short loading times, the same polymer behaves brittle.

The modeling will be done only on the basis of the experimental data obtained at traction for the highest speed (v=1000 mm/min) because it was estimated that for these materials the influence of the test rate, except for the lowest test strain rate (v=10 mm/min), is very low for the shape of the stress-strain curve and the characteristic values obtained from the tensile tests.

6.2. Simulation of Charpy Test under Conditions Similar to the Actual Test

6.2.1. Analysis of Studies with Simulations of Charpy Test

Based on the documentation [Frunză, 2010], [Năstăsescu, 2001], [Ciucă, 2008], the author decided to model the four materials from the second family, considered more efficient.

In the work [Musteață, 2018], it was pointed out that some plastics may have stress-strain curves less sensitive to the rate deformation (Fig. 6.1) for a certain interval, here between v=10 mm/min and v=1000 mm/min, corresponding to a strain rate of 10^{-4} s^{-1} and 0.14 s^{-1}, respectively.

The material models introduced in the Charpy test simulations were made multilinear isotropic, based on experimental data from tensile tests with v=1000 mm/min.

The results reported in the literature show that polymers also have a stress-strain curve dependent on the deformation rate (if other test parameters are kept constant) [Shan, 2007], [Okereke, 2020].

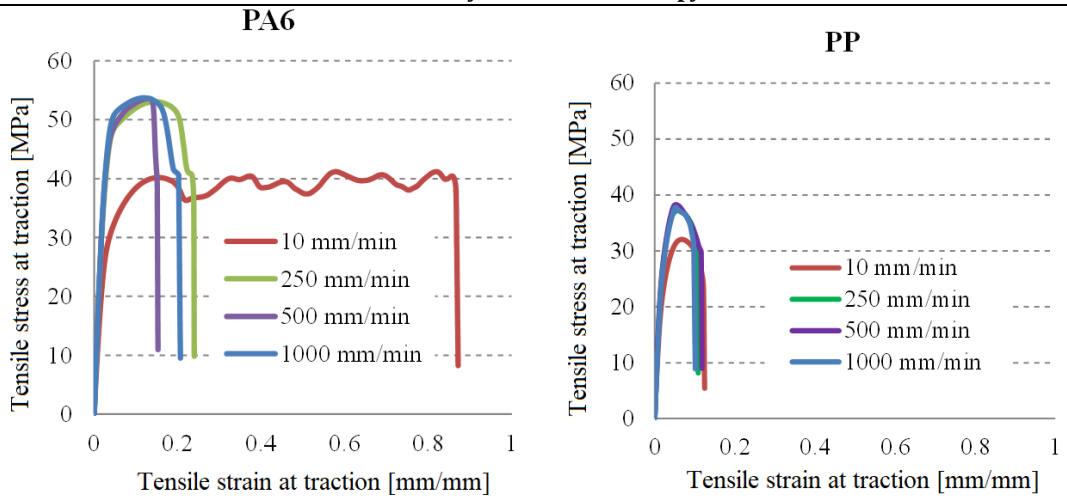

a) Stress – strain curves for PA6 b) Stress – strain curve for PP

Fig. 6.1. Typical stress-strain curves for PP and PA6 [Musteață, 2018]

6.2.2. Constitutive Material Models

From the set of tensile tests, stress-strain curves typical for each of the four materials tested (PPm, H, G and PA6m) were selected, the real curves were calculated and, on each curve, ten points were selected, so that the obtained segments approximate as well as possible the real curve (see Figures 6.2...6.5)

The mesh network of the model was initially coarser and then was finished only in the narrow area containing the notch and the impact area. Minimum final size chosen for the side of the elements is 0.25 mm, the highest values being at the ends of the specimen and at the inactive end of the impactor, 0.75 mm.

The friction between the impactor and the specimen (COF=0.3) and the one between the specimen and the supports (COF=0.3) were taken into account, with the coefficients of friction considered constant during contact.

The impactor was modeled with the real geometry, but with the same mass as in the experiments, thus resulting in a higher density assigned to the impactor material (which is considered non-deformable anyway), so as to reduce the running time.

The simulation time was adapted to the material model, in the sense that the models of material with higher EPS were assigned a longer investigation time of impact ($2.5x10^{-2}$ s) as compared to the models with lower EPS ($1.5x10^{-2}$ s or $5x10^{-3}$ s).

The material models (multilinear with hardening) from the model for each material analyzed,were chosen by introducing the values of the points on the curve that coincide with the values of the real stress-strain curves obtained experimentally from tensile tests for a test speed of v=1000 mm/min (0.016 m/s) for the tested materials (PPm, H, G, PA6m).

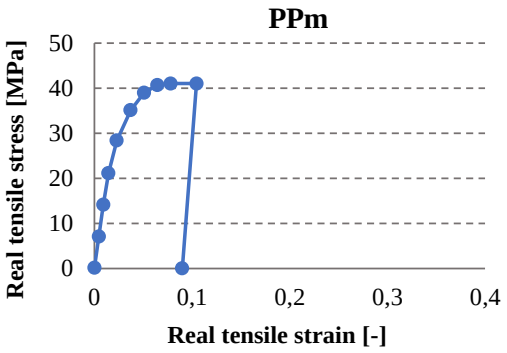

Fig. 6.2. Constitutive model for material PPm

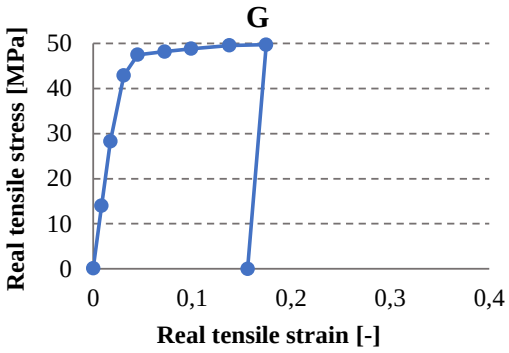

Fig. 6.3. Constitutive model for material G

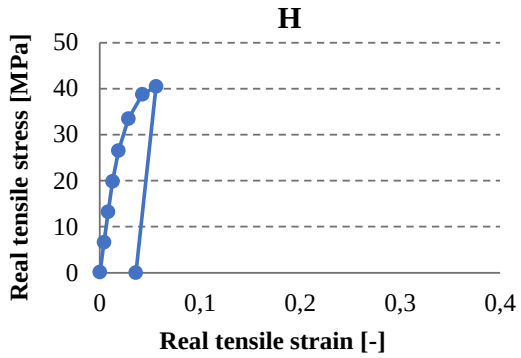

Fig. 6.4. Constitutive model for material H

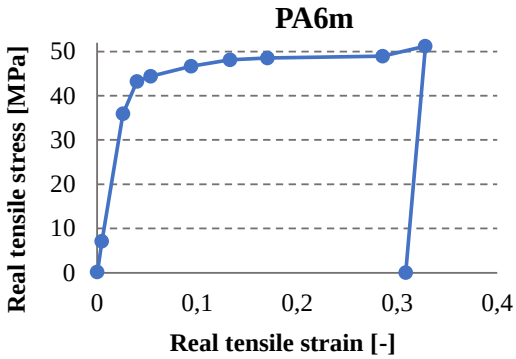

Fig. 6.5. Constitutive model for material PA6m

In Table 6.1. the characteristics of PPm, H, G, PA6m materials are given.

Table 6.1. Characteristics of modeled materials

Characteristic	PPm	H	G	PA6m
Density, kg/m^3	915	915	915	915
Longitudinal modulus of elasticity, E, MPa	1466	1582	1625	1595
Poisson's ratio, ν	0,4	0,4	0,4	0,4
The volume module, MPa	2443,3	2636,7	2708,3	2658,3
Shear modulus, MPa	523,57	565	580,36	569,6
EPS	0,09	0,046	0,156	0,308

6.2.3. Mesh Network for Model with Linear Trajectory Impactor

The issue of the mesh network for the Charpy model is the big difference between the dimensions of the specimen and the dimensions of the notch. Chosing a uniform mesh network would increase the time required for the simulation, without bringing significant improvements in the results of interest (stress distributions, deformations, etc.). In [Rossoll, 1996], [Kumar, 2012], [Saint Catherine, 2002], [Poussard, 2004], [Shokrieh, 2015] are given some solutions of mesh networks, found in the literature for modeling and simulation of Charpy test.

The mesh network was selected to simulate the Charpy test in this paper as in Fig. 6. 6. The size of the sides of the elements is between 0.25 mm and 0.75 mm. Growth ratio between elements 1.2, relatively lower than in the discretizations of other works [Haušild, 2005]. In addition, the model was formed entirely, because in the first simulations with a coarser mesh, it was observed that, although the application of the load and the geometry of the model are symmetrical to a vertical plane, stress distributions and the tendency to zigzag under the notch appeared, a fact also observed on the surfaces of broken specimens.

The assumptions considered in these models are as follows.

- The supports and the impactor are considered rigid, given the difference in properties; impactor and rigid supports were also considered in the works [Poussard, 2004], [Rossoll, 1996], [Serizawa, 2001], [Mohan Kumar, 2012], but in the work of Sainte Catherine [Saint Catherine, 2002] the impactor and supports they were considered perfectly elastic, given the testing of steel specimens.

- The initial velocity (just before impact) is v_0=0.96 m/s (impact velocity, with which the actual tests were performed).

- Boundary conditions: friction between specimen and supports, friction between specimen and impactor (COF=0.3) for all analyzed cases; Poussard [Poussard, 2004], [Haušild, 2012] and Sainte Catherine [Saint Catherine, 2002] did not consider friction, but the friction between impactor and sample and sample and supports was taken into account in the models from [Musteata, 2018].

- Failure criterion: the criterion of equivalent plastic deformation ($EPS_{critical}$) was chosen: when the critical value of EPS was reached in the model, the crack is initiated.

From the experimental results it was found that the four materials for which the impact behavior was simulated with impactor with linear trajectory, have very different EPS, as calculated from the diagram real stress - real deformation (Table 6.3).

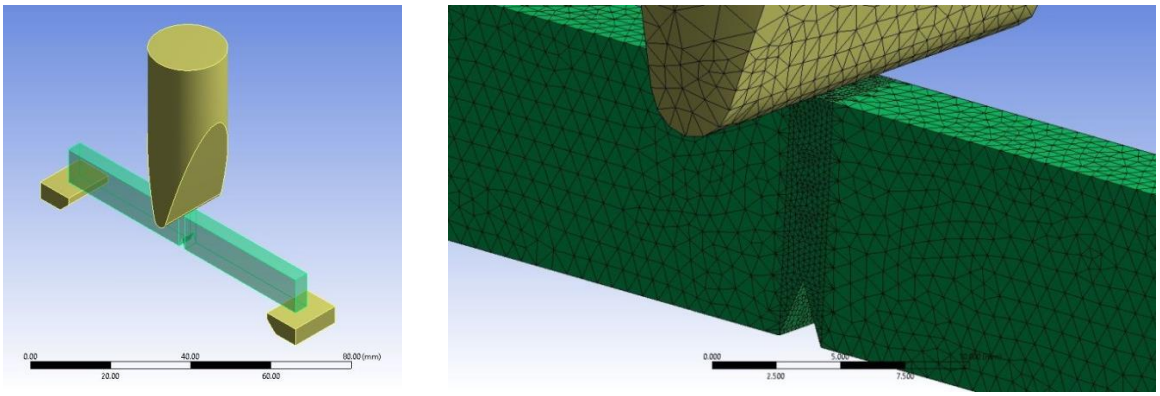

a) b)

Fig. 6.6. Mesh network for Charpy test simulation

Table 6.2. Mesh network statistics

Body	Number of nodes	Number of elements
Impactor	4259	20738
Support 1	3996	3146
Support 2	4212	3354
Specimen	20811	106591
Total for the model	33278	133829

Table 6.3. EPS values for modeled materials

Material (Code)	EPS entered in the model
PPm	0.09
G	0.156
H	0.036
PA6m	0.308

6.2.4. Analysis of Simulations for Each Material from the Second Family

Some images were obtained by considering a half of the transparent specimen (at time t=0 s) (the specimen is not divided into two entities, and the section is right in the plane of symmetry of the notch). This virtual sectioning facilitates the observation of the development of the failure and the change of the distribution of equivalent stresses. A qualitative and quantitative analysis of stress concentrators and how they evolve at any given time as the failure propagates, can be performed.

Material PPm

At the moment closest to the impact ($t=5.0x10^{-4}$ s), two stress concentrators are observed on the tested specimen, one just below the impactor, the other at the tip of the notch, presenting a "butterfly" distribution; the higher values of the equivalent stress are recorded under the impactor σ_{ech}=13.59 MPa. In the following moments, the two stress zones increase in area and value, thus, at time $t=1.0x10^{-3}$ s, σ_{ech}=18.2 MPa. At $t=1.5x10^{-3}$ s, the crack has not yet been created, but the equivalent stress has increased to σ_{ech}=23.9 MPa, recorded under the impactor.

At $t=2.0x10^{-3}$ s, the equivalent stress increased to 29.6 MPa below the impactor and 23.03 MPa at the top of the notch. The specimen is increasingly stressed at time $t=2.5x10^{-3}$ s,

but the initiation of the crack may be seen at t=3.0x10^{-3} s, on a portion of about 2 mm, the equivalent stress reaching 34.15 MPa, this provoquing the local breaking of the material.

From impact of the specimen until the moment t=3.0x10^{-3} s, on the model the critical value of EPS was not reached, $EPS_{(PPm)critical}$=0.09, and therefore, the crack was not initiated.

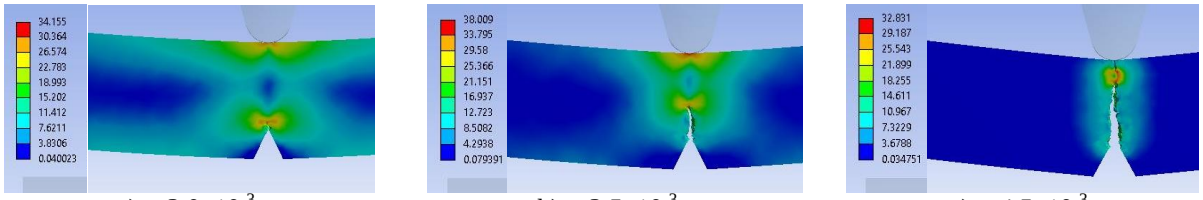

a) t=3.0x10^{-3} s b) t=3.5x10^{-3} s c) t=4.5x10^{-3} s

Fig. 6.7. Selection of important moments in simulation for material PPm

At t=3.5x10^{-3} s, the crack is already propagated over almost half the distance between the top of the notch and the impacted surface. Next, the highest equivalent stress is observed under the impactor σ_{ech}=38 MPa. At time t=4.0x10^{-3} s, the initiation and propagation of the second crack is observed from the impacted part of the specimen to its center. The maximum equivalent stress is visible only at the tip of one of the cracks, at the one initiated from the tip of the notch. At the height of the sample, the still uninterrupted area appears to be 2 mm.

At time t=4.5x10^{-3} s, a maximum of the equivalent stress of 32 MPa is observed which joins like a ribbon the tip of the two cracks.

Although at the beginning the impact had all the symmetrical characteristics compared to the initial plane passing through the tip of the notch, it is observed that later, the stress of the uninterrupted area becomes asymmetric. This phenomenon can occur due to the automatic discretization of the model, although a fine mesh was used, but also to the elasto-plastic behavior of the material. The failure has a zig-zag character, which is also visible on the images obtained at SEM.

At time t=5.0x10^{-3} s, the still unbroken material is on a length of ~ 1.5 mm, length decreasing at time t=5.5x10^{-3} s, leading to the growth of the two cracks, the crack starting from the tip of the notch being kept longer in length than the one started on the side under the action of the impactor.

At t=6.0x10^{-3} s, the maximum equivalent stress moved to the top of the crack from the impactor and has a value of 33 MPa. The moment t=6.5x10^{-3} s is characterized by $\sigma_{ech\ max}$ lower than the previous one, which means that the breaking process (stresses and deformations) alternates with a process of relaxation of the material (σ_{ech} decreases), which is specific to plastics. At t=7.0x10^{-3} s, σ_{ech}= 33.29 MPa, that may be seen in the section of the specimen, which means that there are still small areas unbroken, with local bridges between the two detached fragments of the specimen. The same happens at time t=7.5x10^{-3} s, only that the crack under the impactor, due to the opening of the specimen, may be required for compression. Starting from t=7.5x10^{-3} s, the equivalent stress drops to 20 MPa to t=1.0x10^{-2} s. These stresses, without reaching the stress at break, are due to the collision of the two pieces of the specimen. Complete separation can be observed at t=7.5x10^{-3} s.

At time t=5.0x10^{-4} s, $\sigma_{ech\ max}$ is below half the stress at break. The distribution of equivalent stresses in this sectioning plane is not uniform under the impactor, it seems more uniform at the tip of the notch. Stress concentrators are created at the edge of the theoretical impact line due to automatic meshing and manually introduced material properties, but to a lesser extent the fact that large deformations appear as a margin effect at the ends of the impact line, but also asymmetrical. A maximum stress with values of 13.6 MPa appears in the middle area of the notch.

At time t=1.5x10^{-3} s, the equivalent stresses on the impact line of the specimen are slightly higher but stress concentrators also appear at the base of the notch, more precisely in the middle of it as a 1mm wide band followed by areas with stresses below 20 MPa.

At time t=2.5x10^{-3} s, $\sigma_{ech\ max}$=31.8 MPa, is formed over the entire thickness of the notch tip as an uninterrupted band. At time t=3.0x10^{-3} s, the crack is already initiated and it is observed that it propagates on the height of the specimen, causing an uneven band of maximum stresses of 33 MPa.

The opening of the crack and the continuation of the impact caused on the opposite surface a band of equivalent stress almost as big which still does not yet cause the cracking because the impactor requires compression. The middle area of the specimen is observed, which is almost untensioned in blue and dark blue, with values of 3-7 MPa.

The conclusion that can be drawn from the above is that the impact does not generate stress states in all the volume of the impacted part, but determines areas of stress concentrators where the crack will start.

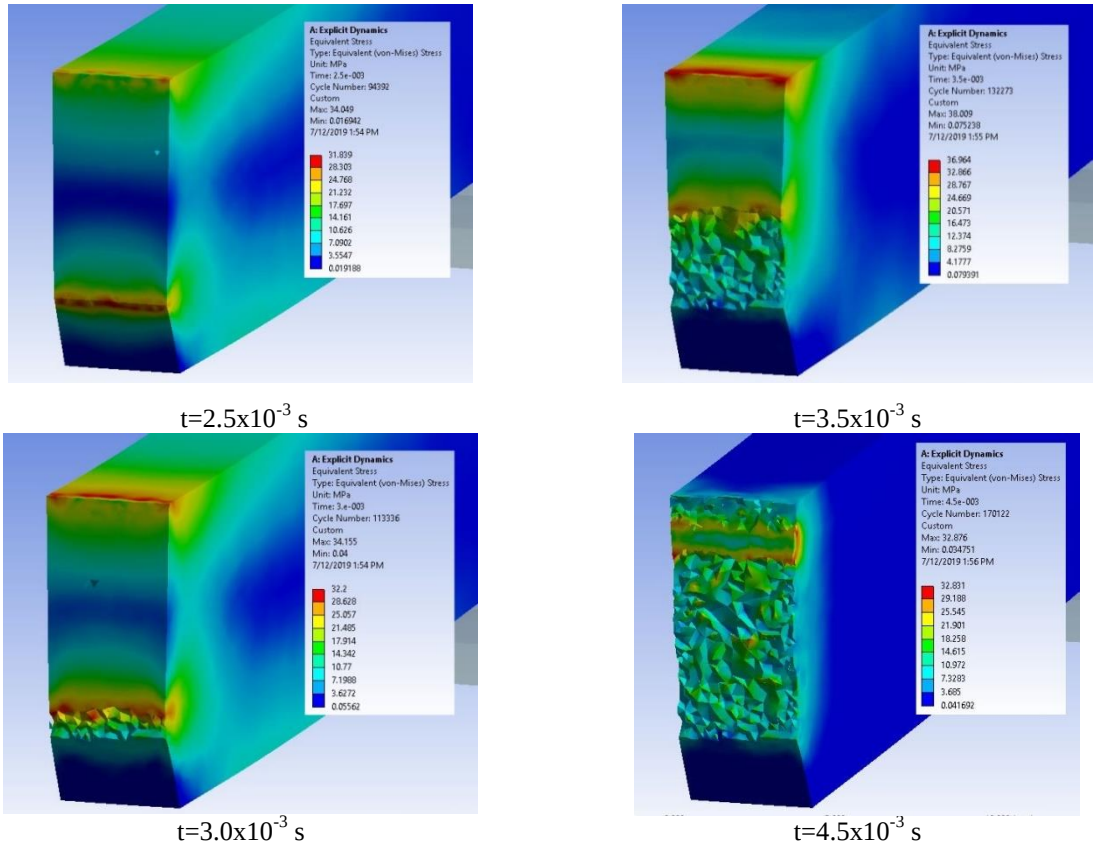

t=2.5x10^{-3} s t=3.5x10^{-3} s

t=3.0x10^{-3} s t=4.5x10^{-3} s

Fig. 6.8. Successive moments from the impact of the test specimen made of PPm material

At time t=3.5x10^{-3} s, the crack initiated at the top of the notch advanced in the middle of the sample section. It is observed that at this moment there are no very high equivalent stresses at the top of the crack or there is only local but that the area under the impactor has a wider range of maximum stresses. Also here an end effect is observed because the maximum equivalent stresses are in a larger volume towards the ends of the impact line.

At time t=4.0x10^{-3} s, the failure advanced, however not uniformly, the crack under the impactor also started. After a microzone was tensioned to the stress at break (EPS_{PPm}), the failure was performed only in the respective microzone, thus appearing another microzone with maximum stresses. At this time, the material left between the two cracks has only a small area with low stresses of 7 MPa.

At time t=5.0x10^{-3} s, the unbroken area stretches for 1-2 mm; even at time t=5.5x10^{-3} s, the linkages between the two fragments of the specimen distributed unevenly across the width of the specimen can be observed.

The smooth surfaces that appear from the moment t=7,5x10^{-3} s, indicate the areas where the upper crack is closed due to the rapid movement of the fragmented gates of the specimen.

Until the moment t=2,5x10^{-3} s, the specimen is not cracked. The crack appears between t=2.5x10^{-3} s and t=3.0x10^{-3} s. At time t=4.5x10^{-3} s the sample has two breaking areas, the one propagated from the notch, but also a narrower one under impactor.

At time t=5.5x10^{-3} s, a very narrow and uneven section can be observed which still unites the two fragments which, at time t=6.0x10^{-3} s are already separated. If high equivalent stresses occur at later times, they are due to the pushing of the fragments into each other until the impactor separates them.

Figure 6.8 shows the breaking surface for the material PPm, its appearance being similar to that obtained in the simulation, but the crack under the impactor is less developed and a superficial crushing destruction is observed which could not be highlighted by modeling. The cracking occurred on a short length and from the impactor.

Material H

Figure 6.9 has a selection of moments during the impact in which the von Mises stress distribution is observed in the lateral view, the appearance and development of the crack at the tip of the notch and then of the crack under the impactor. Due to the color scale, the areas with maximum von Mises stress values (red on each image) are well highlighted.

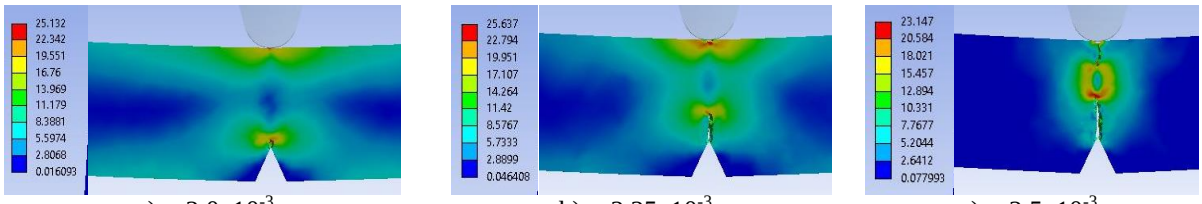

a) t=2.0x10^{-3} s b) t=2.25x10^{-3} s c) t=2.5x10^{-3} s

Fig. 6.9. Selection of important moments in simulation for material H (equivalent stresses, MPa)

The end of the simulation for material H is at the moment t=5.0x10^{-3} s.

In the detail in Fig. 6.10, particularities of the breaking process can be observed at time t=2.5x10^{-3} s, for the material H. The failure propagates from the notch (first) and then from under the impactor. There is an area destroyed by crushing (compression), just below the impactor, as seen in SEM images. The distribution of equivalent stresses at the tip of the cracks is typical of visco-plastic materials.

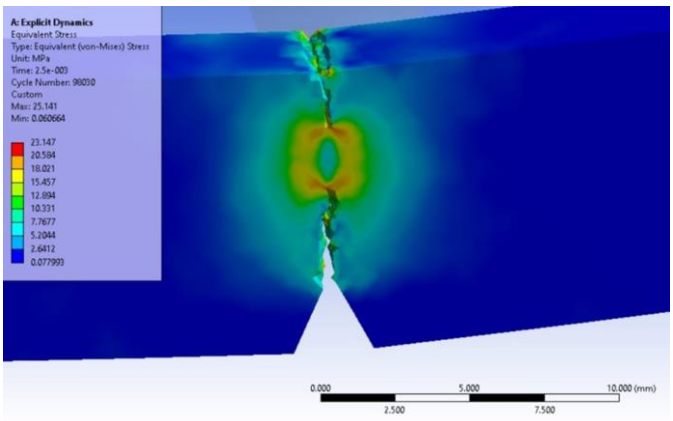

Fig. 6.10. Detail of breaking for material H, at t=2.5x10^{-3} s

The perfectly smooth surfaces visible in Fig. 6.11 are virtually resulted by sectioning with the imaginary plane. It is observed how the crack advances from one moment to another and the area where the last strip of material is lasting (t=3.25x10^{-3} s) before the total fragmentation of the specimen.

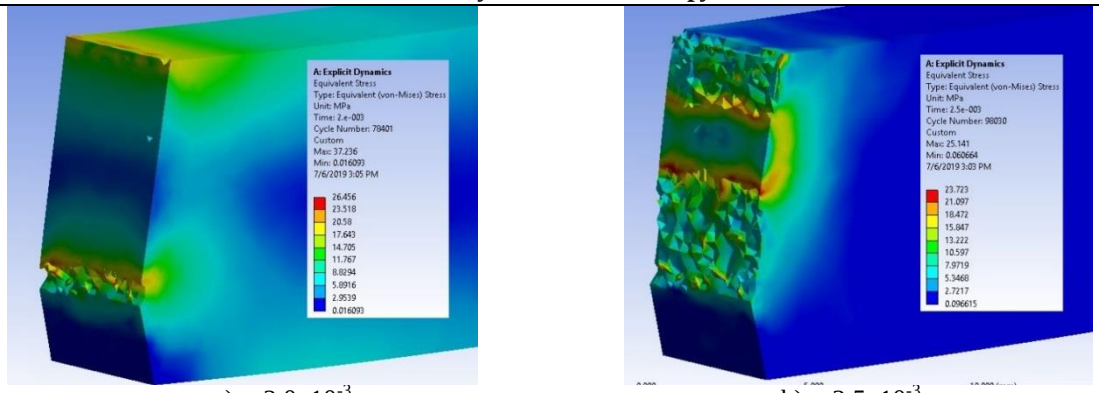

a) $t=2.0x10^{-3}$ s b) $t=2.5x10^{-3}$ s

Fig. 6.11. Appearance of failure in the plane containing the notch tip and the impactor axis, for material H

If a qualitative comparison is made with SEM images of the H material, they are close enough in appearance. In Figs. 6.12 it is observed that the material H has a fragile failure and the initiation of the crack is made first from the tip of the notch, but there is a second crack, initiated from under the impactor, which joins the first at almost 1/4 of the height of the specimen.

The actual appearance of the breaking surface (Fig. 6.12) resembles the appearance of the tear at the end of the simulation. In Fig. 6.11 is observed a destruction by crushing of the material (compression) and an initiation of the crack from the impactor.

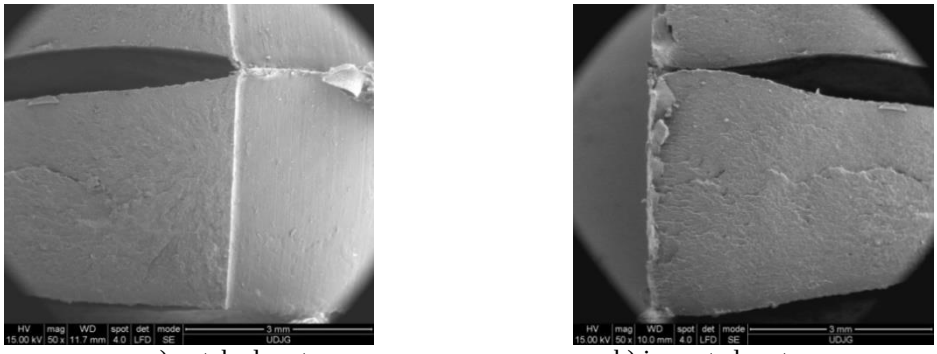

a) notched part b) impacted part

Fig. 6.12. The failure surface of a Charpy specimen, made of material H

Material G

From the experimental data obtained from the Charpy impact test, material G is the second material, in a classification based on energy at break. For this reason, the simulation of impact failure is important compared to the material with better results, PA6m.

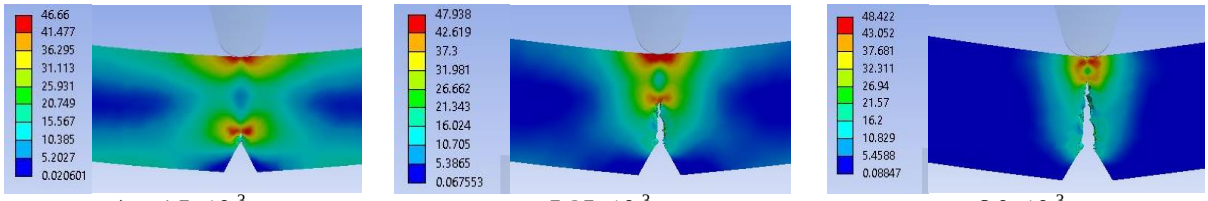

a) $t=4.5x10^{-3}$ s $t=5.25x10^{-3}$ s $t=6.0x10^{-3}$ s

Fig. 6.13. The evolution of the crack generated from the top of the notch, before the initiation of the crack under the impactor, for material G

Figure 6.13 shows the evolution of the crack generated from the top of the notch, before the initiation of the crack under the impactor starts. Fig. 6.14 presents the initiation of the crack under the impactor and the development of the crack at the notch, until the complete separation of the fragments of the specimen. Comparing the images in the simulation from

one moment to the next allows you to establish the starting points of the cracks and how they develop.

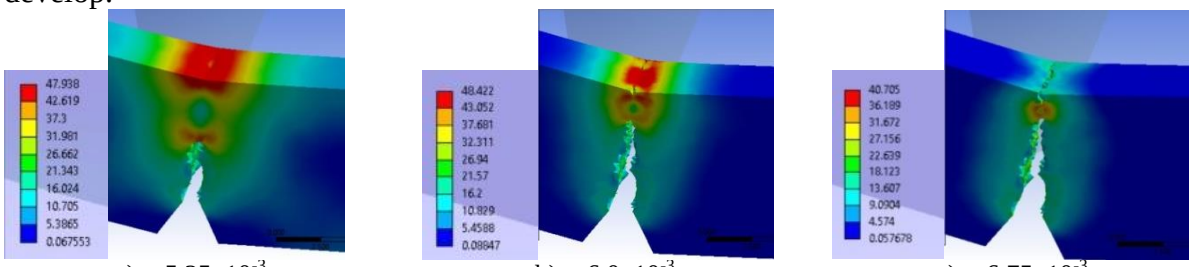

a) t=5.25x10^{-3} s b) t=6.0x10^{-3} s c) t=6.75x10^{-3} s

Fig. 6.14. Successive images in the initiation and propagation of the crack under the impactor, for material G

For example, for material G, in Fig. 6.14a, it is observed that the impactor has created on the impact surface a field of equivalent stresses of high values, close to the stress at break and deforming the specimen so as to force the development of the crack from the notch (b) , but also the initiation of two cracks on the width of the specimen from the ends, in the middle of the specimen maintaining a high stress field. In the image in Fig. 6.14c, it is observed that the union of the two cracks greatly diminished the stress field in the area, strong stress concentrators being in the material left unbroken.

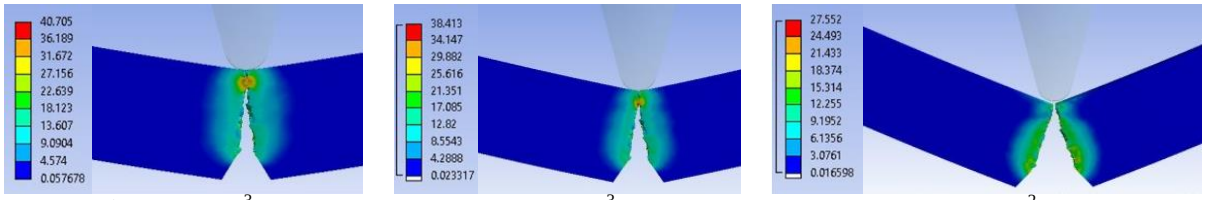

a) t=6.75x10^{-3} s t=9.0x10^{-3} s t=1.5x10^{-2} s

Fig. 6.15. Initiation and evolution of the crack under the impactor, until the separation of the broken fragments for material G

Simultaneous development of stress concentrators is noticed, one around the notch and the other under the impactor, but the failure criterion (EPS=0.156) is reached for the first time at the tip of the notch, at time t=3.75x10^{-3} s, the zone of high von Mises stress (with red color) remaining at the tip of the crack, advancing as it grows, but there is also an area of the same values under the impactor, which as the impactor pushes the specimen, it also increases in surface area (on the side view of the specimen) but also as values.

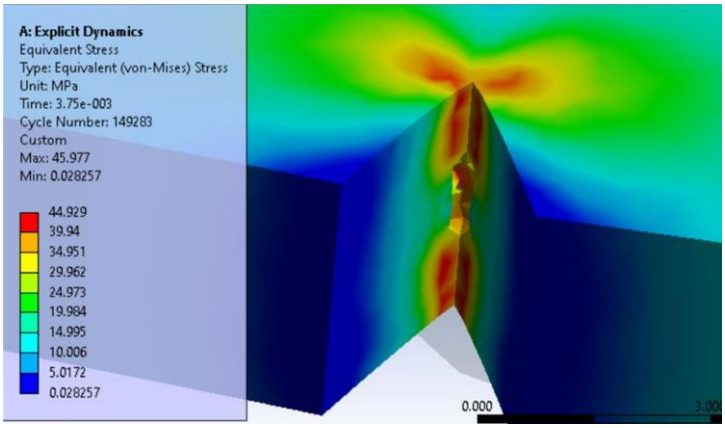

Fig. 6.16. The moment when the crack is first visible on the specimen of material G

The widening of the crack and the change of the angle between the still undissached fragments of the specimen again concentrate the more requested area. Figure 6.14c shows the first moment with the crack under the impactor visible (t=6.75x10^{-3} s). In Figs. 6.15 it is observed that the crack initiated at the top of the notch advances, but at the same time a zone of high stresses is created under the impactor, the crack initiated at the top having a slower propagation speed.

Figure 6.16 shows from another angle, the moment when the crack from the notch was found on the simulation. This is one of the advantages of simulation that destruction mechanisms can be studied and viewed from angles favorable to their explanation.

At the beginning of the impact ($t=7.5x10^{-4}$ s), it is observed the formation of two zones of concentration of stresss on the width of the specimen, along the top of the notch and under the impactor.

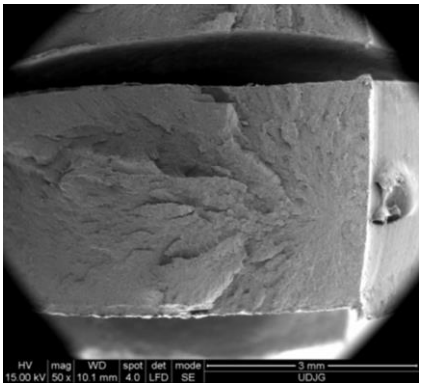

Fig. 6.17. Appearance of impact fracture for a specimen of material G

For G, the failure occurs between moments $t=3x10^{-3}$ s and $t=3.75x10^{-3}$ s, and the crack begins in the middle of the notch width. At time $t=4.5x10^{-3}$ s, the crack is propagated over the entire width of the specimen and has already advanced by almost 1.5 mm.The crack advances towards the other surface of the specimen and the von Mises stress distribution has high values on the impacted surface as well.

At $t=6x10^{-3}$ s, the specimen is not yet completely broken, leaving ~2 mm still uncracked. The continuation of crack development is shown in Fig. 6.14 Figure 6.15 shows moments of crack convergence for material G.

Comparing the images (Fig. 6.18d) with SEM image (Fig. 6.17) may be observed that:

- the aspect of failure is rough both in the model and on the real specimen, the more uneven aspect of the specimen surface being able to be caused by the inhomogeneity of the material;

- a very thin compressed strip is observed in the impact area of the impactor.

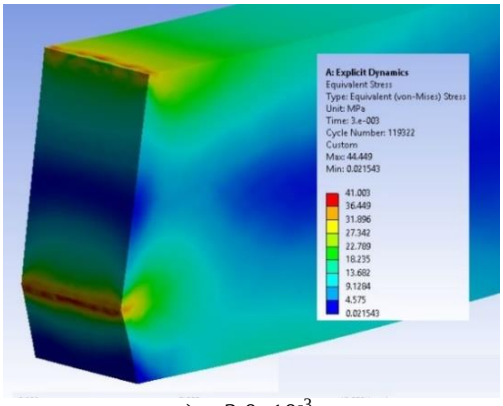

a) $t=3.0x10^{-3}$ s

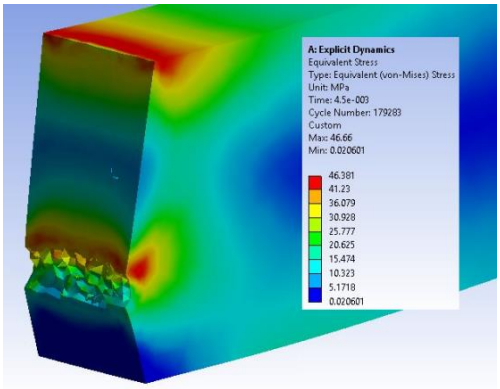

c) $t=4.5x10^{-3}$ s

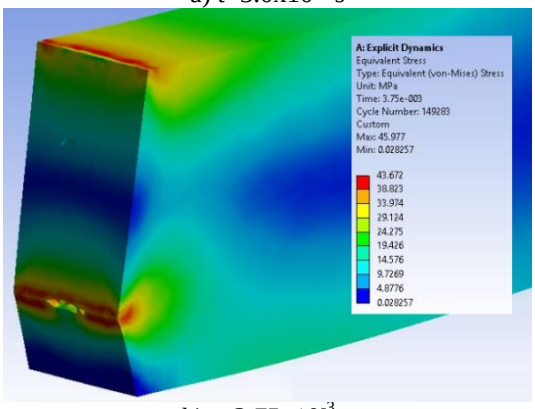

b) $t=3.75x10^{-3}$ s

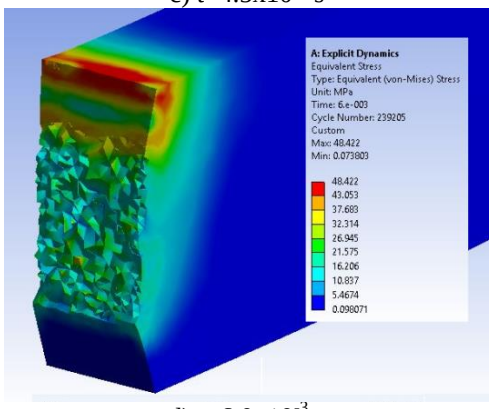

d) $t=6.0x10^{-3}$ s

Fig. 6.18. The evolution of the crack generated from the tip of the notch, before the initiation of the crack under the impactor, for material G

Material PA6m

In Figs. 6.19-6.20, several successive images were chosen to show how the crack advances in the most ductile material (PA6m). The initiation of the crack was made from the top of the notch and at time t=1.25x10^{-2} s, there is a crack of much smaller depth than the one started from the top of the notch. The images from the following moments show that the material left in common, between the two fragments decreases at time t=2.125x10^{-2} s, leaving only a thin band that connects the two fragments. High stress values are also at the top of the crack in the notch. At the last moment of the simulation, another remaining common band and a decrease of the equivalent stress values are observed.

Figures 6.19 and 6.20 show the sequence of moments of destruction, in side view. It can be seen that:

- the specimen did not detach completely (both experimentally and in simulation),
- the running time is the longest, compared to the other modeled materials
- for PA6m material, the EPS at break is the highest.

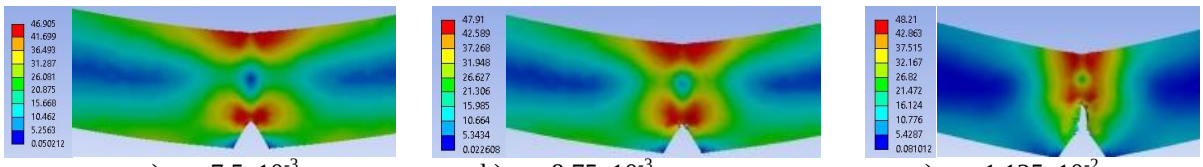

a) t=7.5x10^{-3} s b) t=8.75x10^{-3} s c) t=1.125x10^{-2} s

Fig. 6.19. Lateral view of the specimen made of PA6m, during impact, with von Mises stress distributions (scale is for equivalent stress, in MPa)

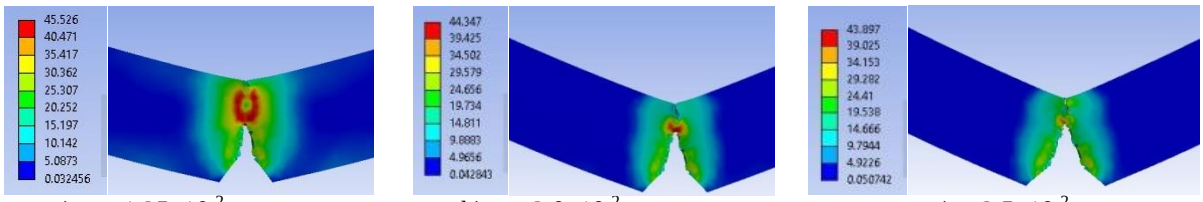

a) t=1.25x10^{-2} s b) t=2.0x10^{-2} s c) t=2.5x10^{-2} s

Fig. 6.20. Lateral view of the PA6m specimen

In Fig. 6.20c, it is observed that for all the tested samples made of PA6m, there is a very narrow area of material that did not break as observed in the simulation.

The breaking process is continued in Figs. 6.22 it is observed that the maximum values of von Mises stresses remain between 47.8 MPa and 43.74 MPa, which means that at any time between t=1.375x10^{-2} s and t=2.5x10^{-2} s, the material breaks.

The PA6m material is more prone to local deformation, the area under the impactor was strongly deformed, observing the trapezoidal shape with the large side under the impactor.

In Fig. 6.22 the imaginary section is observed through the top of the notch which "reveals" that the crack initiates between t=6.25...7.5x10^{-3} s, being located in the middle of the notch. This advances to the other edge of the specimen quite quickly with a fairly rapid concentration of stress near the crack front but you can also see a strongly stressed area under the impactor. At time t=1,125x10^{-2} s, a crack initiated in the area where the impactor strikes is visible.

Fig. 6.21. Breaking of specimens following Charpy tests. for material PA6m

The cracks advance intermittently (sometimes one, sometimes the other) Until the moment t=1x10^{-2} s the crack has propagated from the notch, and at this moment, there are two areas with stress concentration, the one under the impactor and the one in front of the crack, on the surface side shaped like a butterfly.

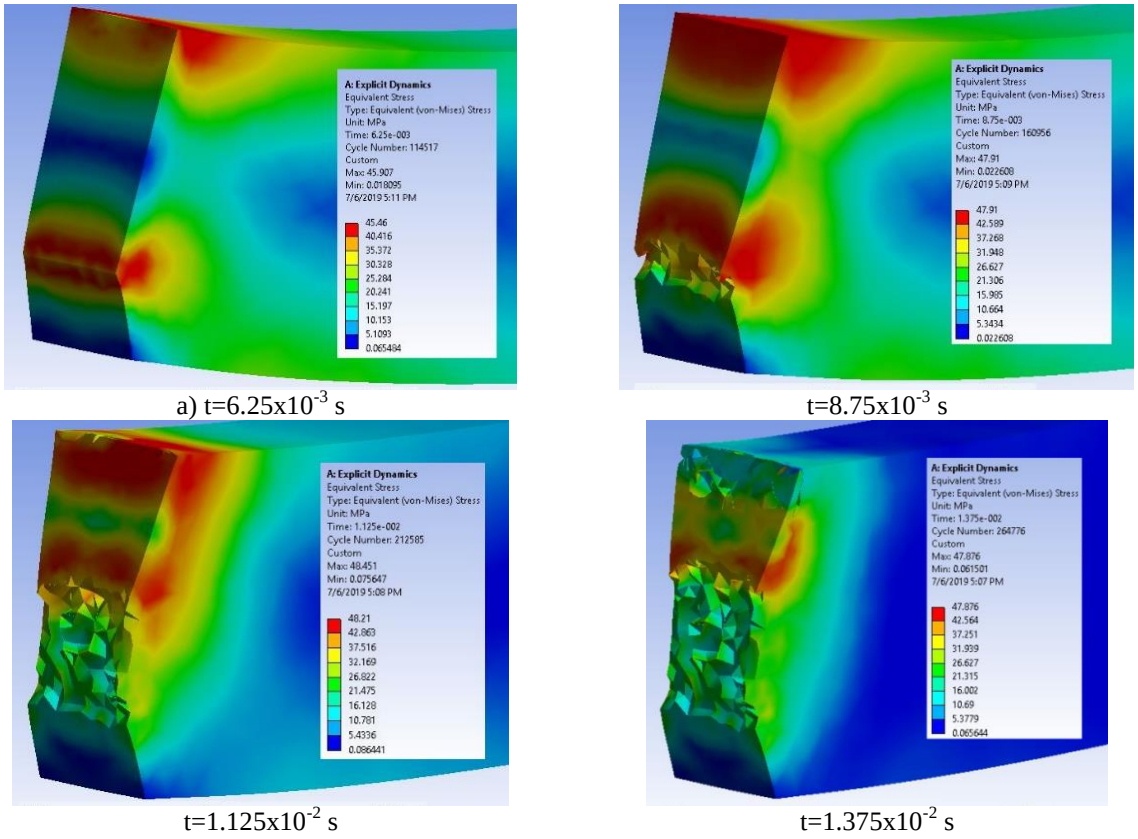

a) t=6.25x10^{-3} s t=8.75x10^{-3} s

t=1.125x10^{-2} s t=1.375x10^{-2} s

Fig. 6.22. Moments during impact for material PA6m

Already at moment t=1.125x10^{-2} s, the crack under the impactor was generated, noting that compared to other materials that initiated crack under the impactor, it is asymmetric, the explanation being the more viscous-plastic character (larger plastic deformations and slope in the smaller plastic field). The propagation of the crack under the impactor, along the entire width of the specimen, relaxes this area, the stress concentrator arching between the two cracks.

Qualitative validation of the crack propagation mode in the PA6m material may be argued by comparing the actual shape of the cracks (Fig. 6.21) with the simulated shape (Fig. 6.23). The nonlinear propagation of the crack and the existence of some micro-volumes elongated outside the separation surface.

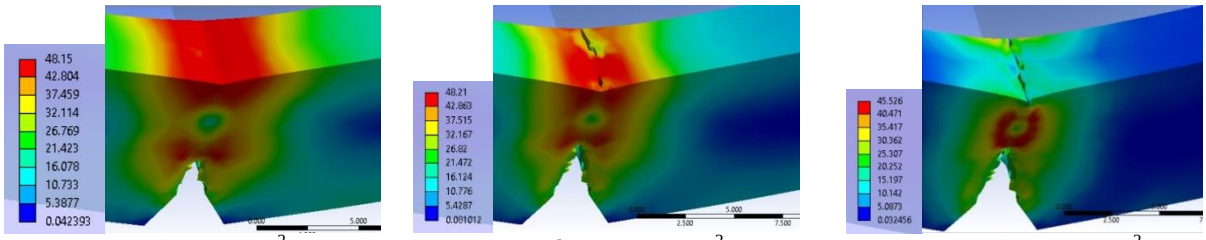

a) t=1.0x10^{-2} s b) t=1.125x10^{-2} s c) t=1.25x10^{-2} s

Fig. 6.23. Details of the impact simulation for the PA6m material

6.3. Conclusions from the Simulations with the Constitutive Models Of Material for the Second Family

The review of available and recent impact modeling documentation in the Charpy test highlighted

- mesh pattern too coarse or too fine,
- disregard for friction in the vast majority of works,
- simplified modeling of the specimen material,
- simplifying hypotheses that can alter the virtual sharing of the sample.

Different failure mechanisms were highlighted due to the different impact velocity. The originality of the proposed model consists in the following:

- finer discretization of the impact area to highlight the mechanisms of failure and their development over time,
- this made it possible to differentiate the destruction mechanisms according to the material introduced in the simulation,
- in the simulations were introduced simplified curves (in 10 points) of the most representative curves real stress - real deformation for the materials of the mixture family,
- depending on the base polymer (PA6 or PP), the initiation and development of failure for the 4 materials were highlighted,
- the author used a less widely used destruction criterion, EPS,
- the validation of the model and the simulation results was done,
- qualitative: the shape of the broken surfaces by comparing to SEM images,
- quantitatively by comparing the impact duration: the duration of the destruction of the specimen is longer than the real one, explainable by the fact that the material model does not take into account the influence of the material deformation speed in the Charpy test, the model being introduced with a 0.016 m/s (1000 mm/min) (maximum strain rate for tensile tests). It is very likely that the appearance of the stress-strain curve will change for 1m/s in the sense of increasing the yield limit and decreasing the EPS.

Comparison between the stress distribution at the same time of the simulation, for different materials, is useful because the degree of damage of the specimen is observed and that could be different. At the time chosen for comparison, only PPm has no cracked initiation. The shape of the crack is also different for each material. H and G have a crack in the depth of the specimen, but for PA6m, the crack is enlarged.

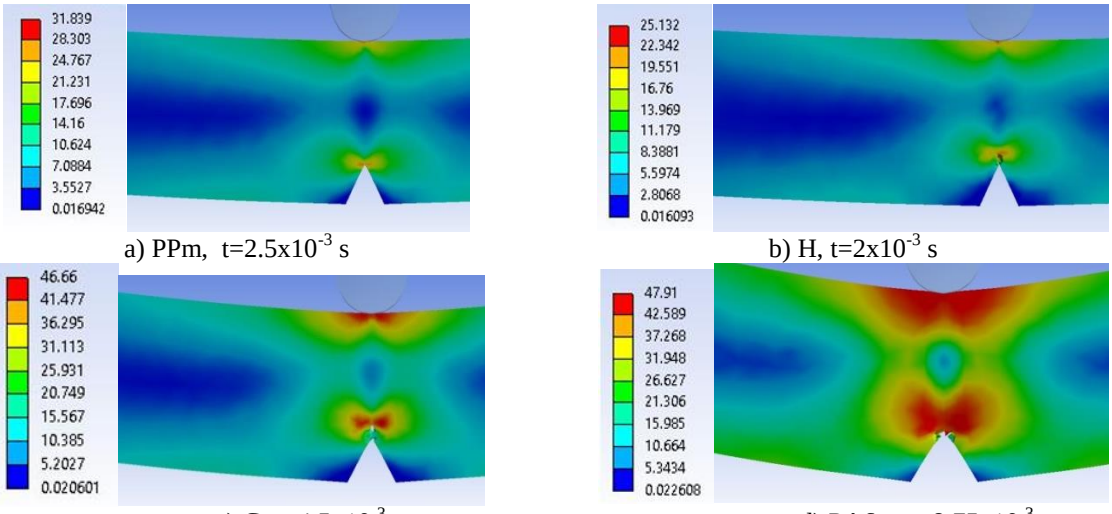

a) PPm, t=2.5x10^{-3} s b) H, t=2x10^{-3} s

c) G, t=4.5x10^{-3} s d) PA6m, t=8.75x10^{-3} s

Fig. 6.24. Crack initiation times for each material and von Mises stress distribution (scale is for equivalent stress, in MPa)

In Fig. 6.24 are given the moments when the crack initiation is visible. It is observed that for material H, the crack appears at time $t=2x10^{-3}$ s, for PPm, the crack appeared at time $t=2.5x10^{-3}$ s. Material G has the crack initiated at time $t=4.5x10^{-3}$ s. The longest time recorded on the simulation for PA6m, $t=2.5x10^{-2}$ s. From these images it is observed that the PPm and H materials are less deformable, the deformation of the notch shape being almost imperceptible. For more ductile materials, the V of the notch opens visibly and the crack shape differs for G and PA6m. For material G, the crack propagates of brittle type in the sense that it develops towards the impactor, while for material PA6m a strong deformation of the material without the crack advancing so rapidly, this is also visible on SEM images from the same angle.

Table 6.8. Analysis of important moments during impact

Material	Moment of impact	Moment of initiation of the first crack [s]	Moment of initiation of the second crack [s]	Moment of total detachment of fragments [s]	Total running time [s]
PPm	0	$2.5x10^{-3}$	$3.5...4.0x10^{-3}$	$7.0x10^{-3}$	$1.0x10^{-2}$
H	0	$1.75x10^{-3}$	$2.0x10^{-3}$	$4.0x10^{-3}$	$5.0x10^{-3}$
G	0	$3.75x10^{-3}$	$6.0x10^{-3}$	$9...9.75x10^{-3}$	$1.5x10^{-2}$
PA6m	0	$7.5x10^{-3}$	$1.125x10^{-2}$	does not fully detach	$2.5x10^{-2}$

The higher the EPS and the higher the yield level, the wider the distribution of high stresses (red) (in a larger volume).

In Fig. 6.25, the evolution of the maximum values of the von Mises stress for the four material models is given. PPm and H materials have better contoured graphs, while the shape of the curve for material G and PA6m indicates a more ductile behavior for these two materials. In general, the maximum values of von Mises stresses indicate the initiation of a crack and/or its continuation after a very short moment of relaxation of the stresses. The last maximum value can also indicate a strong, very punctual compression of the specimen fragments if they collide. Analyzing the images it is likely that the last maximum of material G is due to this compression contact.

PPm and H materials have graphs of the maximum values of von Mises stresses with distinct peaks (three for PPm and two for H), indicating cracks (one from the notch and the other initiated from under the impactor) and/or hits of the fragments with strong local compression. For G and PA6m materials, these curves reflect a much more ductile behavior.

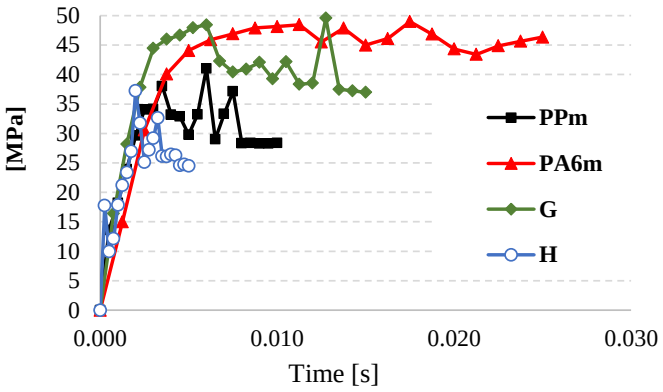

Fig. 6.25. Evolution of the maximum values of the von Mises stress during the simulation, for each material

If it is analyzed the time until the breaking of the Charpy specimen, it may consider the breaking time up to the last maximum of the von Mises stresses), it is observed that the breaking time increases from material H, then PPm, G and for the PA6m mixture breaking is not with the detachment of large fragments of the specimen, nor until the end of the simulation ($t=2.5x10^{-2}$ s). In reality, the time of destruction of Charpy samples is ordered in

the same way as in simulations. For PA6m it is observed that the maximum value of the von Mises stress did not decrease as much at the end of the simulation as for the other materials, suggesting that the specimen has not yet broken completely, remaining a very narrow strip joining the two main fragments of the specimen, which could also be observed in the real specimens.

Table 6.9. Impact characteristics

The parameter	PPm	H	G	PA6m
EPS	0.09	0.036	0.156	0.308
Maximum von Mises stress during impact [MPa]	41.1	37.2	48.4	48.9

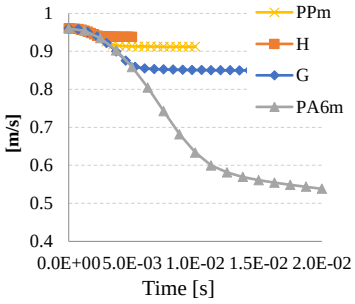

Fig. 6.26. Evolution of the impactor speed during impact.

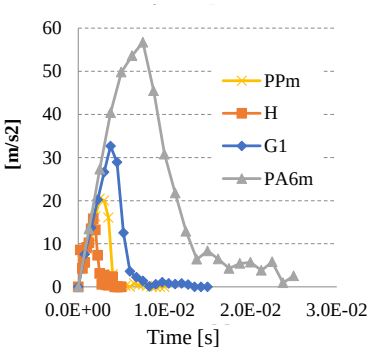

Fig. 6.27. Evolution of impactor acceleration during impact.

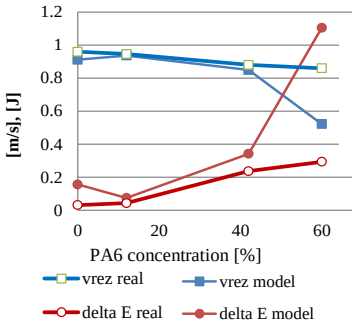

Fig. 6.28. Residual impactor speed and breaking energy at the final moment

*delta E - energy absorbed by the specimen on impact

Figure 6.26 shows the evolution of the impactor speed during the impact. It is observed that the values of the residual velocities are in the same order as the EPS values. For the materials introduced in the simulation, the lowest value of EPS produced the smallest reduction of the impactor speed, as the residual speed enters the formula of the energy absorbed by the test specimen, it results that the material with the highest EPS (PA6m) absorbed the most great energy. The conclusion would be that the residual speed is proportional to the EPS value.

Small differences in energy at break and residual velocity were obtained between the model and real material parameters for PPm, H and G materials (Fig. 6.27...6.28). The best concordance for these two parameters was obtained for material H, followed by G and PPm.

The biggest difference between the model and the actual test, taking into account these parameters, was obtained for PA6m, the material with better Charpy impact characteristics. From this analysis it results that the constitutive model of multilinear material introduced in the simulation of the Charpy test gave results closer to reality for the more fragile materials.

For the most ductil material, with a high yield value, the model had a much higher impact energy absorption than the real one, which would mean that the introduction of the multilinear model obtained at a test rate of 1000 mm/min (0.016 m/s) from tensile tests, does not satisfactorily simulate the behavior of the specimen at impact with speed v=0.96 m/s. Works in the field [Cowper, 1957], [Okereke, 2019], [Shan, 2007], [Shokrieh, 2015], highlighted that even in the field of low impact velocities (1...10 m/s), polymers are sensitive to the rate of stress and implicitly of deformation rate, usually in the sense of increasing the stress at break and decreasing the deformation at break.

6.4. A Discussion of the Influence of the Modeled Material Curve and EPS for Material G

For material G, the difference between the value in the simulation and the actual one was 22.2% compared to the real value, for the energy absorbed on impact until the breaking of the specimen, a difference that could be reduced by adjusting the material model. The author proposed another model of material, G2 which changed the stress at break and EPS.

The cases studied are:

- material G1 (EPS=0.156) and the stress-strain curve in Fig. 6.29a,

- material G2 (EPS=0.05) and the stress-strain curve in Fig. 6.29b.

The curve of the G1 material is based on the multilinear modeling of the tensile results for v=1000 mm/min, and the G2 material is an imaginary material, with lower EPS (EPS = 0.05) and higher yield strength, with slope of the curve in the steeper plastic field, realistic trend for tests with higher speeds, between 0.016 m/s and 1 m/s (the test rates with which the Charpy tests were performed in this paper).

The common properties of the two material models, G1 and G2, are Young modulus ($E_{G1}=E_{G2}=1625$ MPa), Poisson ratio ($\nu_{G1}=\nu_{G2}=0.4$), hydrostatic modulus ($E_{hydrostaticG1}=E_{hydrostaticG2}=2708.3$ MPa), shear modulus ($G_{G1}=G_{G2}=580.36$ MPa), density ($\rho_{G1}=\rho_{G2}=915$ kg/m^3). Different values were taken for the yield strength σ_{G1}==47.4 MPa, $\sigma_{G2}=52.8$ MPa and for the breaking criterion, $EPS_{G1}=0.156$, $EPS_{G2}=0.05$. The trend of increasing the yield limit and decreasing the EPS characterizes a higher deformation rate of a material [Johnson, 1985], [Găvruș, 2009]. It should be emphasized that this model of material (G2) is virtual (Fig. 6.29b), imagined by the author to obtain a more realistic response of the simulation of the behavior of material G on impact, as no experimental data were obtained for higher deformation rates, to make a model based on experimental data.

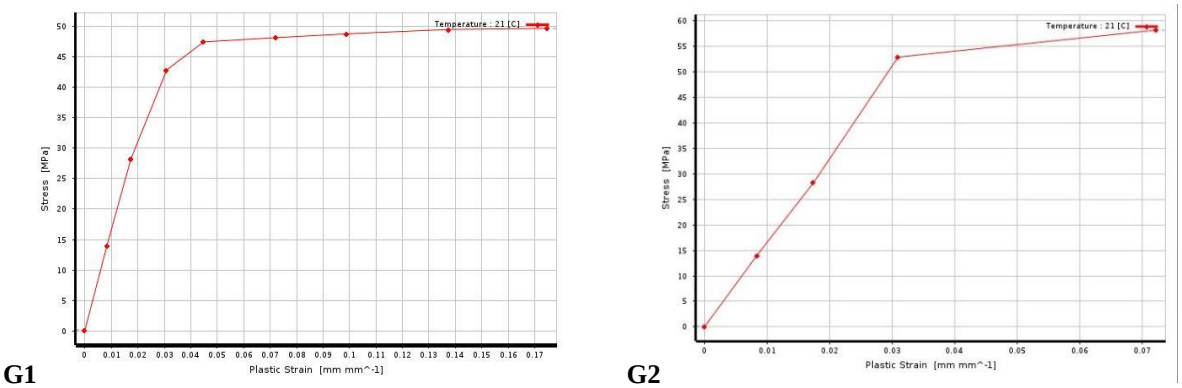

G1 **G2**

Fig. 6.29. Comparison between G1 and G2

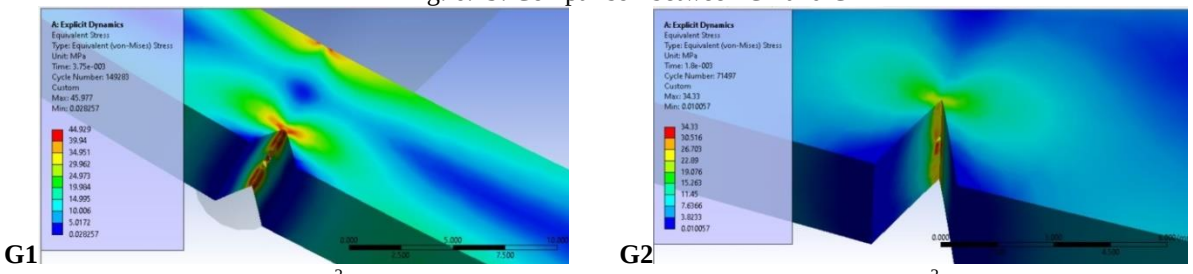

G1 **G2**

a) $3.75x10^{-3}$ s $1.8x10^{-3}$ s

Fig. 6.30. Initiation of the first crack (up - the moment without crack, down - the moment with the crack already started)

At higher deformation rates, EPS is lower and the stress-strain curve is higher which also leads to shortening the time until the specimen breaks.

Figure 6.30 shows two important moments during the destruction of the specimen how the stresses are concentrated at the top of the notch. The images above show the last time von Mises stress distribution without crack initiation, and the images below show the first moment the crack is observed. It appears in the middle of the width of the top of the notch.

Figure 6.31 shows the moment of initiation of the second crack on the specimen, a crack that is initiated under the impactor. The images above show the moment before the crack initiates and in the ones below the crack is already initiated. It is observed that the initiation of the crack takes place for the material G1, symmetrical at the ends of the width of the specimen. The duration between the two events is about $t=1x10^{-3}$ s, for both materials but for the more ductile G1 material, the crack is only about the length of about a third of the

width of the specimen while the G2 material has a crack along the entire width of the specimen this being generated faster and because EPS is lower.

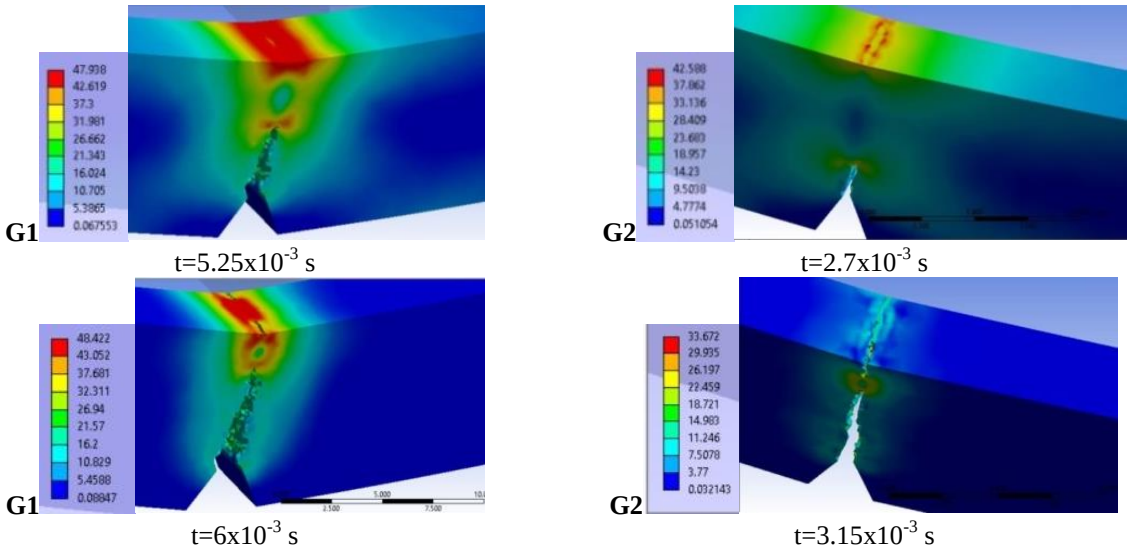

Fig. 6.31. Time moment of the second crack initiation (under the impactor)

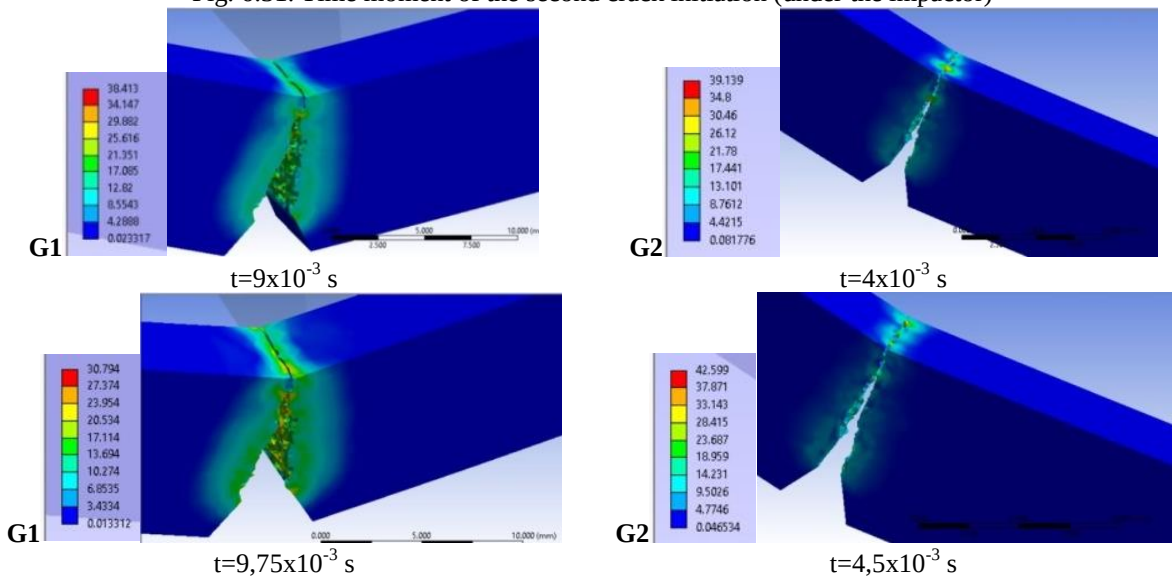

Fig. 6.32. Comparison between the moments of total detachment of the specimen fragments

Changing the material characteristics led to the modification of many aspects of the simulation. In Fig. 6.33 the curve of the maximum values of the von Mises stress is observed. The model with lower value of EPS and higher yield limit (G2) produced the break in a shorter time, highlighting the two cracks by the peaks of maximum values for von Mises stress during simulation. The G1 model produced a failure initiated very close to that of the G2 material, but it has a more ductile character, and the crack under the impactor starts later.

The breaking mechanism seems similar, but the events follow one another faster for the material model with lower EPS and better mechanical characteristics, specific to a higher deformation speed. Modifying the material model with data obtained at higher deformation ratess can also help to calibrate the model on a time scale, which is more difficult to achieve due to the lack of experimental data.

Figure 6.34 shows that the impactor acceleration in the case of simulating material G2, returns to 0 in a time interval approximately twice smaller than for material G1. For material G1, the impactor speed is reduced to 0.922 m/s while the material with higher EPS, G2, reduced the impactor speed to 0.85 m/s.

Another criterion for validating a simulation may be the time to events that can be measured experimentally and can be observed on the simulation. One such parameter is the time until the sample breaks. In the experimental data can be considered the time when the impact force suddenly decreases to 0, this being considered here as the breaking time of the specimen. In Fig. 6.36 the time to the breaking of the specimen for the experimental results and for the simulation results is represented. It is observed that the largest differences were obtained for PPm and PA6m. The results for PA6m are considered as follows: the real time on the graph is the time when F=0, because the specimen did not break for the vast majority of tests (1 of 11). It is observed that the tendency to increase the time to failure is maintained for H and G materials and their models. Regarding PA6m, the values of this time are considered the values for F=0 (both experimental and from simulation).

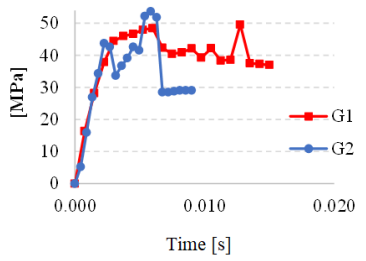

Fig. 6.33. Maximum value of von Mises stress, for materials G1 and G2

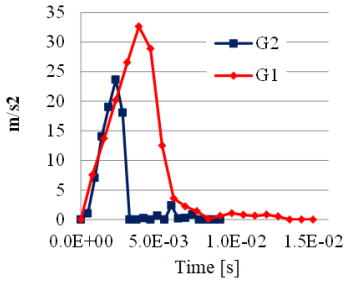

Fig. 6.34. Impactor acceleration

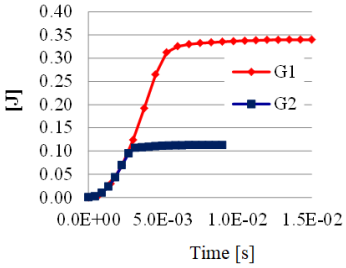

Fig. 6.35. Energy absorbed during the impact

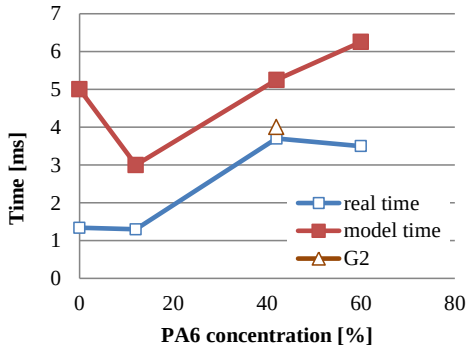

Fig. 6.36. Comparison between the time until breaking of the specimen, real one and that from the simulation

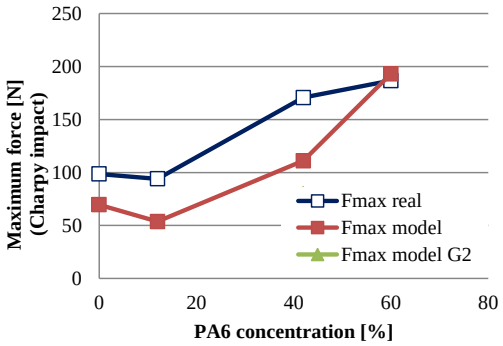

Fig. 6.37. Maximum Charpy impact force, experimental and simulation results, for the materials in this study

The longer simulation time, obtained for all materials, can be argued by the multilinear constitutive model, which does not take into account the modification of the parameters involved in stresses with different deformation speeds, as in the models of Johson Cook, Huh-Kang, Allen- Rule, Cowper-Symonds (commented in [Schwer, 2007], the models proposed by Yaich and Găvruș [Yaich, 2020].

Another validation criterion of the model proposed by the author can be the value of the maximum force: a comparison can be made between the value of the maximum force measured experimentally and the value of the maximum force obtained from the simulation (Fig. 6.37). For PA6m, the values are very close, but for the other materials, the real value exceeds the value recorded in the simulation.

As concerning the results obtained from simulation, the following conclusions can be drawn:

- the proposed material models are qualitatively validated in terms of the shape of the broken surface and the failure of the specimen (specimens break in simulation for PPm, H and G, and do not break for PA6m, as in reality),

- with regard to other validation criteria, the multilinear constitutive models deviated from the actual values, more or less, but these deviations can be justified by the fact that the influence of the deformation rate on the behavior of the materials was not taken into account. Models should be formulated to take into account the specifics of low-velocity impact stress, although experimental data are scarce in the literature.

Chapter 7
Conclusions and Contributions

7.1. Final Conclusions

The results of this work, both experimental and given by simulation, highlight the potential of immiscible blends of polymers, based on PA6 + PP, to obtain a better set of mechanical properties for impact-based applications and to customize characteristics dependent on blend concentration and phase morphology.

The author consulted a documentation (over 320 works) customized for each field (processing, testing, modeling). Based on this documentation, the author proposed a theoretical and experimental study for two families of PA6+PP blends. Initially, in collaboration with eng. Doina Constantinescu, PhD, the first family was formulated (the blends A, B, C and D, based on PP and PA6, having as compatibility agents LDPE, Polybond 3200 and $CaCO_3$), tests were performed on traction and the morphology of the blends was studied, after which, based on a critical analysis of these results, the second family of blends was formulated (H, G as blends with PP + PA6 + EPDM and PA6m - a blend PA6 + EPDM). For both families, Charpy tests were performed, for a single geometry of test specimen (with a C-type notch) and a single impact velocity (0.96 m/s).

The idea of this investigation is original in that it studies the influence of the composition on some mechanical properties, including on the characteristics at moderate shock (~1 m/s) for two families of materials:

- the first family consists of four mixtures with complementary concentrations of PA6 and PP, with the values 20%, 40%, 60%, 80% PA6, to which was added the same investigation for the basic polymers PA6 and PP. In these mixtures were introduced as CaCO3 compatibilizing agents at the micro to nano level (microns and tens of microns) and a Polybond 3200 coupling agent (based on maleic anhydride); the concentration of the compensating agents was the same for all four mixtures,

- the second family of polymeric mixtures consisted of three polymeric mixtures, two having PP + PA6 + EPDM and one blend based only on PA6+EPDM.

The author designed a campaign of tensile tests and tests at Charpy to highlight the differences in behavior of the materials developed. The author used the test equipment, existing at “Politehnica” University of Bucharest and at “Elie Carafoli” Aerospace Research Institute (INCAS). The experimental campaign elaborated and applied by the author, allowed for the mechanical characterization of the elaborated materials.

Tensile tests determined the characteristics such as tensile strength, Young's modulus of elasticity, relative tensile strength and breaking energy for four test speeds and the influence of PA6 concentration and test speed was analyzed.

The author selected four test speeds, available on the Instron 2736-004 test machine, to highlight the influence of the deformation speed on the mechanical characteristics.

Based on the results, it was observed that the four mechanical characteristics are grouped as follows:

- the tensile energy at break and the deformation at break evolve similarly as a function of test speed and PA6 concentration. For neat PP and two PP-matrix blends (A and B), a concentration of values and a very low dependence on the test speed were noticed. Therefore, for the studied test speed ranges, materials A and B do not significantly change the average values of these characteristics. The other two characteristics evolved differently. The modulus of elasticity does not have a clear dependence on concentration and speed, but with the exception of PA6, at v=10 mm / min, it evolves in a band of 230 MPa (1500-1800 MPa).

The breaking stress decreases for material A compared to PP, after which the mixtures have a tendency to increase the breaking stress with increasing PA6 content, not always the breaking stress changing visibly and with the test speed.

3. Charpy tests showed the breaking energy of the C-notch specimens and the maximum force during the destruction process. Figure 7.1 shows the impact strength of the two families as a function of polyamide concentration and shows higher values for material G and PA6m, compared to PA6, which is recognized as a polymer with applications for components required at impact. The first family had a slightly increasing trend starting with material A, which had weaker results than PP, and growing slightly to material D.

The graph highlights the big difference between the two families. It can be concluded that the intake of EPDM for mixtures with a concentration of 40-60% PA6 are optimal recipes for improving impact resistance.

4. The author identified specific failure processes, both in traction and for Charpy impact, by studying the images obtained with an scanning electron microscope at "Dunarea de Jos" University, FEI Quanta 200 brand (4 nm resolution, magnification 1 million times, analysis with the built-in EDX spectrometer).With the help of the EDX spectrometer, it was possible to establish the phase reversal in the first family, which takes place between the concentrations of 40-60% PA6.

5. The author designed a finite element model for Charpy test, to analyze the dynamics of failure processes, dynamics that cannot be studied experimentally with the available equipment. The simulation campaign was based on two groups of simulations:

- simulations showing the influence of the impact velocity on the results of a constituent model for a polymeric material [Musteață, 2018],

- simulations as realistical as possible of the specimen breaking, with multilinear constitutive models, differentiated for each material, based on experimental data obtained from tensile tests, with the highest test speed (1000 mm/min). It was observed, based on the analysis of the equivalent stress distribution, that the introduction of different material models, appropriate to the actual behavior, highlights different durations and modes of destruction for this Charpy test.

This simulation allowed the author to identify stages of destruction processes and their duration, the cracking mode (with a single crack initiated from the top of the notch, or with two cracks, one initiated from the top of the notch and the other initiated later, under the impactor). The von Mises stress distribution and how the stresses are concentrated during crack propagation were analyzed. The speed and acceleration of the impactor during the impact were studied because the initial speed and the residual speed can be a measure of the energy consumed by the impactor to break the specimen, and the acceleration reflects the force with which the impactor acts, considering the impactor mass constant (3,4 kg).

The model developed by the author is original because it takes into account the elements that make up the system and their particularities:

- the large differences in mechanical properties between the impactor and the specimen led to the consideration of the impactor as a perfectly rigid body, thus simplifying the model and managing to capitalize on the computer resources available;

- the model includes the friction between the supports and the test piece, but also the friction between the impactor and the test piece, introducing in the model a realistic but constant value of the coefficient of friction.

The multilinear model for materials gave better results for more fragile materials and results farther from the experimental values for more ductile materials (G and PA6m). The conclusion would be that ductile materials have a behavior more strongly influenced by the deformation speed.

6. The study of the morphology of the mixtures made by the author showed:

- first family: biphasic morphologies are created in which the two polymers PP and PA6 change their role with changing concentrations. Thus, for materials A and B, the matrix consists of PP, and PA6 is in the form of droplets. For materials C and D, the phases are

reversed, the matrix becoming PA6, and PP being in the form of droplets partially attached to the PA6 matrix, which would explain the better results than PP matrix mixtures (materials A and B) , but less efficient than PA6 and mixtures with PA6 + EPDM and PP + PA6 + EPDM (material G).

- the second family: very different morphologies are created, in the sense that, for G and PA6m, EPDM and PA6 become a compatible matrix and the PP droplets attach more strongly than to the first matrix family. In the rupture sections there are no more cavities generated by the injection molding in the mat and / or on request, neither in the tensile test, nor in the Charpy test, but there is a fibrillation process, ie generation of fibrils between drops and matrix, which it makes the energy needed to break them greater.

For the first family, it was found that the technological process and the concentration of mixtures proposed by the author led to the formation of injection cavities, these cavities are generated due to preferential cooling of the polymer mixture near the walls of the mold in materials B, C and D. cooling of the two materials, the specimen begins to solidify at the edge and inside, due to the surface tension, where the cooling / solidification of the material takes place more difficult, gaps are created that tend to pull towards the already cooled material (the one from outside). These cavities can alter the mechanical properties and therefore the scattering of the values of the mechanical characteristics for these materials was quite large. The same problems regarding the formation of cavities during processing have been reported for these mixtures by other authors [Gonzales Montiel, 1995], [Bai, 2004], [Bai, 2005].

Based on the specialized work and the experimental results, the author concluded that better mechanical properties for a PP + PA6 mixture could be obtained by introducing an elastomer-type compatibilizing agent, which has the role of preventing the separation of dispersed droplets from matrix.

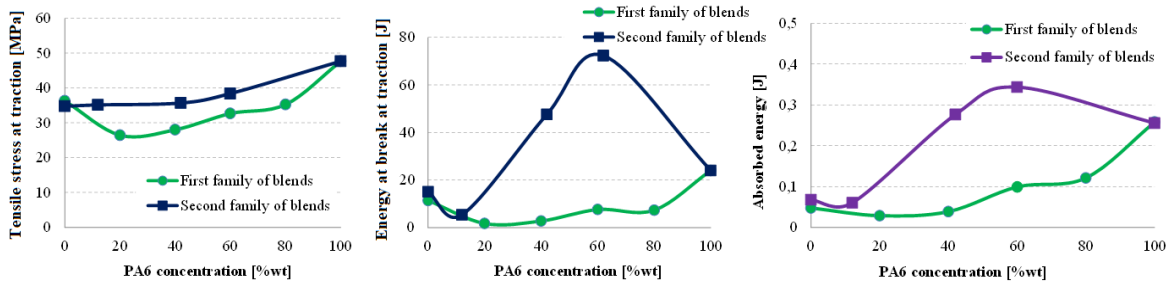

a) Average values of the tensile stress at traction

b) Average values of the energy at break at traction

c) Average values of the absorbed energy

Fig. 7.1. Mechanical characteristics of the two polymeric families

The author formulated a new family, to which EPDM was added. Three original recipes were made, material H (PP+12% PA6+8% EPDM), material G (PP+42% PA6 + 28% EPDM) and material PA6m (60% PA6+40% EPDM). The same tests, performed for this second family of polymer blends, showed good tensile properties for PA6m and G and much improved properties of Charpy test parameters (Fig. 7.1b and c), two of the materials (G and PA6m) may be recommended for applications of moderate impact, instead of PA6, which is a polymer with dimensional instability, water absorption and quite difficult to process by injection[Dupont™ Zytel® and Minlon® Guide].

7.2. Personal Contributions

Through this work, the author had the following contributions:

- preparation of documentation on polymer mixtures, focusing on mixtures containing PP and PA6, including the morphology of PP + PA6 mixtures in order to be able to compare

with the morphology of mixtures developed by it, a documentation on tensile and impact testing Charpy type, a documentation on finite element modeling of the Charpy test.

- development of original PP + PA6 blend recipes, of which two out of seven reported good results; these two materials (G and PA6m) may be recommended for applications where they have to deal with low or moderate speed shock,
- the design of a test campaign to characterize the tensile materials developed at different test speeds and the Charpy test,
- synthesis of experimental results and highlighting of better materials; for the tensile results, the author established the influence of the test speed on the range 10...1000 mm/min,
- establishing dependencies between the mechanical properties and the composition of the polymer mixtures,
- designing a model for finite element analysis, which realistically simulates the stages and mechanisms of destruction of modeled materials based on experimental results, so that from the results of the simulations to draw conclusions for future better material recipes and encourage the use of simulations in describing and understanding the processes of destruction of polymeric materials,
- the simulation was performed in a dynamic process, a less common aspect in the existing models in the literature, the results being good and very good for understanding the stages and mechanisms of material transfer,
- dissemination of results through papers published in ISI (two) and BDI (five) journals presented at international and national conferences and a poster at the UgalInvent UGAL Innovation and Research Salon 2019,
- the processing of the experimental results involved the acquisition of skills to work with software dedicated to test machines and simulations, the winTest Analysis software for the universal test machine, Testometric M350-5AT for the Charpy test machine - CEAST 9340, Ansys Solid Mechanics (explicit dynamic), other software (EXCEL and MathLab) used in the processing of experimental data,
- non-destructive investigations using the scanning electron microscope and the EDX spectrometer serving it,
- qualitative and quantitative validation of the model on the basis of several criteria (time to rupture of the specimen, maximum force in the Charpy test, energy absorbed on impact and residual speed),
- development of multilinear constitutive models of materials (PPm, H, G and PA6m), based on experimental data from tensile tests writh the highest rate (1000 mm/min),
- calibration of the model by modifying the constitutive (virtual) model, taking into account the influence of the behavior of a material at higher deformation speeds (material G2 with higher breaking stress and lower plastic breaking deformation (EPS)).

7.3. Perspectives for Further Research

Research in the field of polymer blends is promising because recyclable thermoplastic materials can be used, in certain concentrations, to meet strength requirements, but also involve a reduction in the cost of separating waste materials.

A future reseach that could continue this study and its results may include:

- optimization of PP and PA6-based blend recipes, with application-specific compatibility agents (eg assessment of low- and medium-speed impact behavior by Charpy and free-fall impact tests),
- development of finite element models for the evaluation of stress and strain state of test specimens for polymer blends and validation based on experimental results, a step forward being an adiabatic modeling and introducing models based on experimental data, obtained at deformation rates closer to that for Charpy impact,
- testing under other impact conditions (drop test etc.).

References

[1] Ahn Y-C., Paul D. R. (2006) Rubber toughening of nylon 6 nanocomposites. *Polymer*, **47**, 2830–2838, doi: 10.1016/j.polymer.2006.02.074.

[2] Albrecht W., Fuchs H., Kittelmann W., Lünenschloss J. (2006) *Manufacture, applications, characteristics, testing processes*. Weinheim, Wiley-VCH.

[3] Alexandrescu L., Sönmeza M., Georgescu M., Nițuică A., Ficai R., Trusca R., Gurău D., Tudoroi L. (2017) Polyamide/Polypropylene/graphene oxide nanocomposites with functional compatibilizers. Morpho-structural and physico-mechanical characterization. *Procedia Structural Integrity*, **5**, 675-682.

[4] Antunes C. F., Machado A.V., Duin M. (2011) Morphology Development and Phase Inversion during Dynamic Vulcanisation of EPDM/PP Blends. *European Polymer Journal*, **47**, 1447–1459.

[5] Arnold M. (2015) Instrumented Pendulum Impact Testing for Plastic, testXpo, https://fdocuments.in/document/instrumented-pendulum-impact-testing-for-plastics-impact-testing-102015-mareike.html

[6] Bai S. L., Wang G. T., Hiver J. M., G'Sell C. (2004) Microstructures and mechanical properties of polypropylene/polyamide 6/polyethelene-octene elastomer blends. *Polymer*, **45**, 3063-3071.

[7] Bai S., G'Sell C., Hiverc J.-M., Mathieu C. (2005) Polypropylene/polyamide 6/polyethylene-octene elastomer blends. Part 3. Mechanisms of volume dilatation during plastic deformation under uniaxial tension. *Polymer*, **46**, 6437–6446.

[8] Banerjee S., Joshi M., Ghosh A. K. (2013) Investigations on clay dispersion in polypropylene/clay nanocomposites using rheological and microscopic analysis, *Journal of Applied Polymer Science*, **130**, 4464–4473, https://doi.org/10.1002/app.39590

[9] Berstad T., Langseth M., Hopperstad O. S. (1994) Elasto-viscoplastic constitutive models in the explicit finite element Code LS-DYNA3D. *Second International LS-DYNA3D User Conference*, San Francisco.

[10] Beuguel Q., Ville J., Crepin-Leblond J., Mederic P., Aubry T. (2017) Influence of formulation on morphology and rheology of polypropylene/polyamide blends filled with nanoclay mineral particles, *Applied Clay Science*, **147**, 168–175.

[11] Bicerano J. (2002), *Prediction of Polymer Properties*, 3rd edition, Marcel Dekker Inc, New York.

[12] Biron M., (2010) Polypropylene: A chameleon that competes with engineering plastics & many other materials, *SpecialChem*, https://omnexus.specialchem.com/tech-library/article/polypropylene-a-chameleon-that-competes-with-engineering-plastics-many-other-materials

[13] Botan M. (2014) Caracterizarea mecanică și tribologică a unei clase de compozite polimerice, teza de doctorat, Universitatea "Dunărea de Jos" din Galați

[14] Botan M., Georgescu C., Pirvu C., Deleanu L. (2014) Influence of aramid fibers on mechanical properties of two polymeric blends, *22nd International Conference on materials and technology*. Portoroz Slovenia, **53**.

[15] Boțan M., **Musteață A. E.**, Ionescu T. F., Georgescu C., Deleanu L. (2017) Adding aramid fibres to improve tribological characteristics of two polymers, 15th International Conference on Tribology, Kragujevac, Serbia, *Tribology in Industry*, **39(3)**, 283-293. http://paper.researchbib.com/view/paper/135458

[16] Bradley R. (1984) *Radiation Technology Handbook*, Marcel Dekker, New York.

[17] Brown R. (2002) Handbook of Polymer Testing. Short-Term Mechanical Tests. Rapra Technology Limited, ISBN: 1-85957-324-X.

[18] Chanda M., Roy S.K. (2009) *Plastics fundamentals, properties and testing*. CRC Press Taylor & Francis Group.

[19] Chow W. S., Mohd Ishak Z. A. (2015) Polyamide blend-based nanocomposites: A review. *eXPRESS Polymer Letters*, **9(3)**, 211–232. doi: 10.3144/expresspolymlett.2015.22

[20] Chow W. S., Mohd Ishak Z. A., Karger-Kocsis J. (2003) Compatibilizing effect of maleated polypropylene on the mechanical properties and morphology of injection molded polyamide 6/ polypropylene/organoclay nanocomposites. *Polymer*, **44**, 7427–7440.

[21] Ciucă I., Bolcu D., Stănescu M.M. (2008) Elemente de mecanica solidelor deformabile și teoria ruperii. *Editura Didactică și Pedagogică*, București, ISBN 978-973-30-2398-2.

[22] Cowper G. R., Symonds P. S. (1957) Strain-hardening and strain-rate effectsin the impact loading of cantilever beams. Office of Naval Research, Contract Ncmr-562(10), NR-064-406 Technical Report No. 28 Brown University Providence.

[23] Datta S., Lohse D. J. (1996) *Polymeric Compatibilizers*. Hanser/Gardner Publications, Cincinnati.

[24] Folkes M. J., Hope P. S. (1993) Polymer blends and alloys. *Blackie Academic and Professional*, London

[25] Frunză G., Spînu S. (2010) *Fundamentele teoriei plasticității*. Editura Universității " Ștefan cel Mare"din Suceava, ISBN 978-973-666-336-9.

[26] Fu S.-Y., Lauke B., Lid R. K.Y., Mai Y.-W. (2006) Effects of PA6,6/PP ratio on the mechanical properties of short glass fiber reinforced and rubber-toughened polyamide 6,6/polypropylene blends, *Composites: Part B*, **37**, 182–190.

[27] G'Sell C., Bai S.L., Hiver J.M. (2004) Polypropylene/polyamide 6/polyethylene-octene elastomer blends. Part 2: volume dilation during plastic deformation under uniaxial tension. *Polymer*, **45**, 5785–5792.

[28] G'Sell C., Hiver J. M., Dahoun A. (2002) Experimental characterization of deformation damage in solid polymers under tension, and its interrelation with necking. *International Journal of Solids Structures*, 39, 3857–3872.

[29] Găvruș A. (2009) Formulation of a new constitutive equation available simultaneously for static and dynamic loadings. *EDP Sci. Web of Conf. Proc. DYMAT*, 1239–1244.

[30] Găvruș A. (2012) Constitutive Equation for Description of Metallic Materials Behavior during Static and Dynamic Loadings Taking into Account Important Gradients of Plastic Deformation. *Key Engineering Materials*, 504–506: 697–702.

[31] Găvruș A., Caestecker P., Ragneau E. (2012) Finite element analysis of the influence of the material constitutive law formulation on the chip formation process. *ASME Proc. of 11th Int. Conf. ESDA*.

[32] Gonzales-Montiel A., Keskkula H., Paul D. R. (1995) Impact-modified nylon 6/polypropylene blends: 3. Deformation mechanisms. *Polymer*, **36**, 4621–37.

[33] Grob M. C. (2012) *Plastic additives: an answer for the new trends in the plastic industry*, BASF Schweiz AG, Tagung Kunststofftechnologie 2012 (HTA-FR), Fribourg, Switzerland.

[34] Hancock M., Rothon R. N. (1995) *Principle types of particulate fillers. în: Rothon RN* (ed) Particulate-filled polymer composites. Longman, Harlow, p. 50, Rapra Technology Limited

[35] Harrats C., Sabu Thomas Gabriel Groeninckx (2006) *Micro- and Nanostructured Multiphase Polymer Blend Systems. Phase Morphology and Interfaces*, CRC Press Taylor & Francis Group.

[36] Hasanpour M., Mazidi M. M., Aghjeh M. K. R. (2019) The effect of rubber functionality on the phase morphology, mechanical performance and toughening mechanisms of highly toughened PP/PA6/EPDM ternary blends, *Polymer Testing*, **79**, https://doi.org/10.1016/j.polymertesting.2019.106018.

[37] Haušild P., Berdin C., Rossoll A. (2005) Modelling of the Charpy impact test in the DBTT range. *Materials Science Forum*, **482**, 331-334.

[38] Hosseini F. S., Ahmadloo E. (2015) An investigation of thermal and mechanical properties of synthesised polyamide-6/γ-alumina composites. *Plastics, Rubber and Composites*, **44**, 182-188, doi:10.1179/1743289815Y.0000000009

[39] Huang J. J., Keskkula H., Paul D.R. (2006) Elastomer particle morphology in ternary blends of maleated and non-maleated ethylene-based elastomers with polyamides: Role of elastomer phase miscibility. *Polymer*, **47**, 624–638.

[40] Jiang C., Zhua Z., Zhang J., Yanga Z., Jiang H. (2020) Constitutive modeling of the rate- and temperature-dependent macro-yield behavior of amorphous glassy polymers, *International Journal of Mechanical Sciences*, 179.

[41] Johnson G. R., Cook W. H. (1985) Fracture characteristics of three metals subjected to various strains, strain rates, temperatures and pressures. *Engineering Fracture Mechanics*, **21**, 31-48.

[42] Johnson G. R., Cook W.H. (1983) A constitutive model and data for metals subjected to large strains, high strain rates and high temperatures, *7th International Symposium on Ballistics*, The Hague, The Netherlands.

[43] Jose S., Francis B., Thomas S., Karger-Kocsis J. (2006) Morphology and mechanical properties of polyamide 12/polypropylene blends in presence and absence of reactive compatibiliser, *Polymer*, **47**, 3874–3888.

[44] Kusmono, Mohd Ishak Z. A., Chow W. S., Takeichi T., Rochmadi (2008) Influence of SEBS-g-MA on morphology, mechanical, and thermal properties of PA6/PP/organoclay nanocomposites. *European Polymer Journal*, **44**, 1023–1039, doi: 10.1016/j.eurpolymj.2008.01.019.

[45] Laoutid F., Estrada E., Michell R. M., Bonnaud L., Müller A. J., Dubois P. (2013) The influence of nanosilica on the nucleation, crystallization and tensile properties of PP/PC and PP/PA blends, *Polymer* **54**, 3982-3993.

[46] Lee H.-H. (2019) *Finite Element Simulations with ANSYS Workbench 2019*, SDC Publications

[47] Li H., Xie X.-M. (2017) Morphology development and superior mechanical properties of PP/PA6/SEBS ternary blends compatibilized by using a highly efficient multi-phase compatibilizer, *Polymer*, **108**, 1-10.

[48] Li H., Xu Y., Zhang T., Niu K.,Wang Y., Zhao Y., B. Zhang, (2020) Interfacial adhesion and shear behaviors of aramid fiber/polyamide 6 composites under different thermal treatments. *Polymer Testing*, **81**, 106-209.

[49] Liu S., Kouadri-Hennia A., Găvruș A. (2018) DP600 dual phase steel thermo-elasto-plastic constitutive model considering strain rate and temperature influence on FEM residual stress analysis of laser welding. *Journal of Manufacturing Processes*, 407-419. doi:10.1016/j.jmapro.2018.07.006

[50] Ma L., Yang W., Guo H. (2019) Effect of cross-linking degree of EPDM phase on the morphology evolution and crystallization behavior of thermoplastic vulcanizates based on polyamide 6 (PA6)/ethylene-propylene-diene rubber (EPDM) blends. *Polymers*, **11**, 1375. doi:10.3390/polym11091375

[51] McKeen L.W. (2008) *The effect of temperature and other factors on plastics and elastomers*, William Andrew Inc.

[52] Mohan Kumar K., Devaraj M. R., Lakshmi Narayana H. V. (2012) Finite element modelling for numerical simulation of Charpy impact test on materials Proceedings of the International Conference on Challenges and Opportunities in Mechanical Engineering, *Industrial Engineering and Management Studies ICCOMIM*, 32-36.

[53] **Musteață A. E.**, Pelin G., Botan M., Deleanu L. (2018) Tensile Tests for Polyamide 6 and Polypropilene, *Mechanical Testing and Diagnosis*, **4**, 16-22.

[54] **Musteață A. E.**, Boțan M., Pelin G., Deleanu L., Constantinescu D. (2018) Tensile characteristics for a class of polymeric blends (PP + PA6), IOP Conference Series: Materials Science and Engineering, Volume 485, 8th Conference on Material Science and Engineering (UgalMat 2018), Galati, Romania, https://iopscience.iop.org/article/10.1088/1757-899X/485/1/012015

[55] **Musteață A. E.**, Boțan M., Petrescu H., Pirvu C., Constantinescu D., Deleanu L. (2019) Amestecuri polimerice cu rezistență la șoc, UGAL INVENT Salonul Cercetării și Inovării organizat de Universitatea „Dunărea de Jos" din Galați, Lucrările Salonului Inovării și Cercetării UgalInvent 2019, 115, http://www.invent.ugal.ro/ROcatalogue2019.html

[56] **Musteață A. E.,** Pelin G., Boțan M., Popescu A., Deleanu L. (2020) The behavior in traction test of polymeric blends PP+PA6, Materiale Plastice, **57 (1),** 153-166. https://revmaterialeplastice.ro/pdf/18%20MUSTEATA..1%2020.pdf, https://doi.org/10.37358/Mat.Plast.1964

[57] **Musteață A. E.**, Pîrvu C., Deleanu L., Georgescu C. (2018) Simulation of Charpy test for different impact velocities, *IOP Conference Series: Materials Science and Engineering*, Volume 514, Product Design, Robotics, Advanced Mechanical and Mechatronic Systems and Innovation Conference (PRASIC) 8–9, Romania. doi: 10.1088/1757-899X/514/1/012011

[58] **Musteață A. E.**, Stanilă V., Deleanu L., Bria V., Georgescu C. (2016) Influence of PTFE concentration in PBT on mechanical properties, *Mechanical Testing and Diagnosis*, **3**, 5-9, https://www.gup.ugal.ro/ugaljournals/index.php/mtd/article/view/2304/1964

[59] Năstăsescu V., Ştefan A., Lupoiu C. (2001) Analiza neliniară prin metoda elementelor finite, *Fundamente teoretice şi aplicaţii* (Bucureşti: Academia Tehnică Militară)

[60] Okereke M. I., Akpoyomare A. I. (2019) Two-process constitutive model for semicrystalline polymers across a wide range of strain rates, *Polymer*, **183**.

[61] Ou B., Li D., Liu Y. (2009) Compatibilizing effect of maleated polypropylene on the mechanical properties of injection molded polypropylene/polyamide 6/functionalized-TiO_2 nanocomposites, *Composites Science and Technology*, **69**, 421–426.

[62] Palacios J. K., Sangroniz A., Eguiazabal J. I., Etxeberria A., Müller A. J. (2016) Tailoring the properties of PP/PA6 nanostructured blends by the addition of nanosilica and compatibilizer agents, *European Polymer Journal*, **85**, 532–552.

[63] Pîrvu C., **Musteață A. E**., Ojoc G. G., Sandu S., Deleanu L. (2019) A meso level fe model for the impact bullet - yarn, Revista de Materiale Plastice, 56(1) 22-31, https://revmaterialeplastice.ro/pdf/5%20PARVU%201%2019.pdf

[64] Poussard C., Sainte Catherine C., Forget P., Marini B. (2004) On the identification of critical damage mechanisms parameters to predict the behavior of Charpy specimens on the upper shelf. in *Predictive material modeling: combining fundamental physics understanding*, Computational Methods and Empirically Observed Behavior, eds. M. Kirk, M. Natishan (West Conshohocken, PA: ASTM International), 103-120.

[65] Rosato D. V., Rosato Donald V., Rosato V. M. (2004) *Plastic Product Material and Process Selection Handbook*, Elsevier Science & Technology Books.

[66] Rosato D., Rosato D. (2003) *Plastics Engineered Product Design*, Elsevier Ltd.

[67] Rossoll A., Tahar M., Berdin C., Piques R., Forget P., Prioul C., Marini B. (1996) Local Approach of the Charpy Test at Low Temperature. *Journal de Physique IV Colloque*, **06**, 279-286.

[68] Rothon R. N. (1999) Mineral Fillers in Thermoplastics: Filler Manufacture and Characterisation. *Advances in Polymer Science*, **139**.

[69] Sainte Catherine C., Hourdequin N., Galon P., Forget P. (2002) Finite element simulations of Charpy-v and sub-size Charpy tests for a low alloy rpv ferritic steel, *Small Specimen Test Techniques*: 4th volume, Sokolov M. A., Landes J.D. și Lucas G. E. (editori), ASTM International, West Conshohocken, PA.

[70] Schwer L. (2007) Optional Strain-Rate Forms for the Johnson Cook constitutive model and the role of the parameter Epsilon_0^1, Dynamore GmbH, LS-Dyna, Andwerderforum, Frankenthal, Impact, https://www.dynamore.de/en/downloads/papers/07-forum/impact/optional-strain-rate-forms-for-the-johnson-cook/view

[71] Serizawa H., Zhengqi W. U., Murakawa H. (2001) Computational analysis of Charpy impact test using interface elements. *Transactions of JWRI*, **30**, 97-102.

[72] Shan G.-F., Yang W., Yang M., Xie B., Feng J., Fu Q. (2007) Effect of temperature and strain rate on the tensile deformation of polyamide 6. *Polymer*, **48**.

[73] Sharma K. R. (2012) Polymer Thermodynamics Blends, Copolymers and Reversible Polymerization, *CRC Press Taylor & Francis Group*, ISBN 13: 978-1-4398-2640-9.

[74] Shokrieh M. M., Joneidi V. A. (2015) Characterization and simulation of impact behavior of graphene/ polypropylene nanocomposites using a novel strain rate–dependent micromechanics model. *Journal of Composite Materials*, **49**, 2317–2328.

[75] Utracki L. A. (1995) History of commercial polymer alloys and blends (From a perspective of the patent literature). *Polymer Engineering Science*, **35**, 1–17.

[76] Utracki L. A. (2002) *Polymer Blends Handbook*, Kluwer Academic Publishers, Dordrecht, London, ISBN 1-4020-1114-8 Set.

[77] Vranjes Penava N., Rek V., Fiamengo Houra I. (2012) Effect of EPDM as acompatibilizer on mechanical properties and morphology ofPP/LDPE blends. *Journal of Elastomers & Plastics*, **45**, 391–403, doi: 10.1177/0095244312457162

[78] Wang K., Wang C., Li J., Su J., Zhang Q., Du R., Fu Q. (2007) Effects of clay on phase morphology and mechanical properties in polyamide&6/EPDM-g-MA/organoclay ternary nanocomposites. *Polymer*, **48**, 2144–2154, doi: 10.1016/j.polymer.2007.01.070

[79] Yaich M., Găvruș A. (2020) New phenomenological material constitutive models for the description of the Ti6al4v titanium alloy behavior under static and dynamic loadings. *Procedia Manufacturing*, **47,** 1496–1503.

[80] Yu S., Yek W. M., Ho S. Y., Rannou S. A.D., Lim S. H. (2015) Microstructure and impact strength of polyamide 6 composites. *Materials Today Communications*, **4**, 199–203.

[81] *** Dupont™ Zytel® And Minlon® Nylon Resins Molding Guide, https://www.dupont.com/content/dam/dupont/amer/us/en/transportation-industrial/public/documents/en/Zytel%20and%20Minlon_Nylon_Resin_Molding_Guide_GNE-A11218-00-A1216_050117_OM.PDF

[82] *** Kritilen Masterbatches, https://www.plastikakritis.com/assets/uploads/files/Plastika%20Kritis_masterbatches-001.pdf

[83] *** Polyamide (Nylon) - Troubleshooting Common Nylon Processing Problems, https://plastics.ulprospector.com/generics/22/c/tr/polyamide-nylon-troubleshooting

[84] *** SR EN ISO 179-1:2010 Materiale plastice. Determinarea caracteristicilor la şoc Charpy. Partea 1: Încercarea neinstrumentală la şoc

[85] *** SR EN ISO 179-2:2002 Materiale plastice. Determinarea proprietăţilor de şoc Charpy. Partea 2: Încercarea instrumentală la şoc

[86] *** SR EN ISO 527-1:2020 Materiale plastice. Determinarea proprietăților de tracțiune. Partea 1: Principii generale

[87] *** SR EN ISO 527-2:2012 Materiale plastice. Determinarea proprietăţilor de tracţiune. Partea 2: Condiţii de încercare a materialelor plastice pentru injecție și extrudare

[88] ***Polypropylene (PP) Typical Properties Generic PP Impact Copolymer, https://plastics.ulprospector.com/generics/39/c/t/polypropylene-pp-properties-processing/sp/26

[89] ***Polypropylene(PP),http://www.irpcmarket.com/upload/document/datasheet-1516693272.pdf

Scientific Papers

Elaborated by eng. Andreea Elena Musteață

1. **Musteață A. E.,** Pelin G., Boțan M., Popescu A., Deleanu L., The behavior in traction test of polymeric blends PP+PA6, Review de Materiale Plastice, 2020, https://revmaterialeplastice.ro/pdf/18%20MUSTEATA..1%2020.pdf

2. Pîrvu C., **Musteață A. E.,** Ojoc G. G., Sandu S., Deleanu L., A meso level fe model for the impact bullet - yarn, Revista de Materiale Plastice, 56(1) 22-31, 2019, https://revmaterialeplastice.ro/pdf/5%20PARVU%201%2019.pdf

3. **Musteață A. E.**, Pîrvu C., Deleanu L., Georgescu C., Simulation of Charpy test for different impact velocities, IOP Conference Series: Materials Science and Engineering, Volume 514, Product Design, Robotics, Advanced Mechanical and Mechatronic Systems and Innovation Conference (PRASIC) 8–9 November 2018, Brasov, Romania, DOI: 10.1088/1757-899X/514/1/012011

4. **Musteață A. E.**, Boțan M., Pelin G., Deleanu L., Constantinescu D., Tensile characteristics for a class of polymeric blends (PP + PA6), IOP Conference Series: Materials Science and Engineering, Volume 485, 8th Conference on Material Science and Engineering (UgalMat 2018) 11–13 October 2018, Galati, Romania, https://iopscience.iop.org/article/10.1088/1757-899X/485/1/012015

5. Boțan M., **Musteață A. E.,** Ionescu T. F., Georgescu C., Deleanu L., Adding aramid fibres to improve tribological characteristics of two polymers, 15th International Conference on Tribology, Kragujevac, Serbia, 17 – 19 May 2017, publicat în Tribology in Industry, **39(3),** 283-293, http://paper.researchbib.com/view/paper/135458

6. **Musteață A. E.,** Pelin G., Boțan M., Deleanu L., Tensile Tests for Polyamide 6 and Polypropilene, Mechanical Testing & Diagnosis. 2018, 8(4), 16-22.

7. **Musteață A. E.**, Stanilă V., Deleanu L., Bria V., Georgescu C., Influence of ptfe concentration in pbt on mechanical properties, Mechanical Testing and Diagnosis, 2016(VI), **3**, pp. 5-9, https://www.gup.ugal.ro/ugaljournals/index.php/mtd/article/view/2304/1964

8. **Musteață A. E.,** Boțan M., Petrescu H., Pîrvu C., Constantinescu D., Deleanu L., Amestecuri polimerice cu rezistență la șoc, UGAL INVENT Salonul Cercetării și Inovării organizat deUniversitatea „Dunărea de Jos" din Galați, 16-18 Octombrie 2019, Lucrările Salonului Inovării și Cercetării UgalInvent 2019, p. 115, http://www.invent.ugal.ro/ROcatalogue2019.html